Florida International University

FIU Digital Commons

FIU Electronic Theses and Dissertations | University Graduate School

3-25-2021

Design and Realization of Fully-digital Microwave and Mm-wave Multi-beam Arrays with FPGA/RF-SOC Signal Processing

Sravan kumar Pulipati
spuli009@fiu.edu

Follow this and additional works at: https://digitalcommons.fiu.edu/etd

Part of the Electrical and Electronics Commons, Signal Processing Commons, and the Systems and Communications Commons

Recommended Citation

Pulipati, Sravan kumar, "Design and Realization of Fully-digital Microwave and Mm-wave Multi-beam Arrays with FPGA/RF-SOC Signal Processing" (2021). *FIU Electronic Theses and Dissertations*. 4652.
https://digitalcommons.fiu.edu/etd/4652

This work is brought to you for free and open access by the University Graduate School at FIU Digital Commons. It has been accepted for inclusion in FIU Electronic Theses and Dissertations by an authorized administrator of FIU Digital Commons. For more information, please contact dcc@fiu.edu.

FLORIDA INTERNATIONAL UNIVERSITY

Miami, Florida

DESIGN AND REALIZATION OF FULLY-DIGITAL MICROWAVE AND MM-WAVE MULTI-BEAM ARRAYS WITH FPGA/RF-SOC SIGNAL PROCESSING

A dissertation submitted in partial fulfillment of the

requirements for the degree of

DOCTOR OF PHILOSOPHY

in

ELECTRICAL AND COMPUTER ENGINEERING

by

Sravan Kumar Pulipati

2021

To: Dean John Volakis
College of Engineering and Computing

This dissertation, written by Sravan Kumar Pulipati, and entitled Design and Realization of Fully-Digital Microwave and mm-Wave Multi-Beam Arrays with FPGA/RF-SoC Signal Processing, having been approved in respect to style and intellectual content, is referred to you for judgment.

We have read this dissertation and recommend that it be approved.

Elias Alwan

Shubhendu Bhardwaj

Satheesh Venkatakrishnan

Todd Crowl

Arjuna Madanayake, Major Professor

Date of Defense: March 25, 2021

The dissertation of Sravan Kumar Pulipati is approved.

Dean John Volakis
College of Engineering and Computing

Andrés G. Gil
Vice President for Research and Economic Development
and Dean of the University Graduate School

Florida International University, 2021

© Copyright 2021 by Sravan Kumar Pulipati
All rights reserved.

DEDICATION

To my parents, friends and well-wishers!

ACKNOWLEDGMENTS

First and foremost, I would like to sincerely thank my advisor, Dr. Arjuna Madanayake, for always being there to guide, motivate, share ideas and provide encouragement to me throughout my Ph. D. program.

I would like to express my gratitude to the committee members Dr. Elias Alwan, Dr. Shubhendu Bhardwaj, Dr. Satheesh Venkatakrishnan and Dr. Todd Crowl for their unreserved help and support. Also, I would like to thank Dr. Chamira Edussooriya, Dr. Chamitha Wijenayake, Dr. Leonid Belostotski and Dr. Sirani Perara for their contribution towards my research that led to several publications.

I am very grateful to my past and present research fellow-mates in the RAND group especially Viduneth Ariyarathna, Najath Akram and Nilan Udayanga. They always kept me motivated and it has been a pleasure to work with them. Finally, I take this opportunity to dedicate this dissertation to my father Vijay Kumar Pulipati, my mother Vijaya Laxmi Pulipati, my brothers Rahul and Susheel. Although we have been thousand of miles apart, they always had me in their prayers and wishes! This journey wouldn't have been possible without their immense support.

Special Acknowledgements:

I am extremely grateful for the financial support provided by funding provided by National Science Foundation (NSF) Spectrum Efficiency, Energy Efficiency, and Security (SpecEES) throughout my graduate studies. I would also like to acknowledge funding support provided by the ECE department at FIU. of support, which provided an opportunity for an international student like me to pursue graduate studies, was invaluable. Many thanks!

The generous support from the ROGERS Corporation for donating PCB boards used in the fabrication of the microwave components is gratefully acknowledged. I would also like to thank the CASPER and Xilinx communities for guiding me in difficult situations when working with Reconfigurable Open Architecture Computing Hardware (ROACH) and RF-System on chip (SoC) platforms.

ABSTRACT OF THE DISSERTATION

DESIGN AND REALIZATION OF FULLY-DIGITAL MICROWAVE AND MM-WAVE MULTI-BEAM ARRAYS WITH FPGA/RF-SOC SIGNAL PROCESSING

by

Sravan Kumar Pulipati

Florida International University, 2021

Miami, Florida

Professor Arjuna Madanayake, Major Professor

There has been a constant increase in data-traffic and device-connections in mobile wireless communications which led the fifth generation (5G) implementations to exploit mmWave bands at 24/28 GHz. The next generation wireless access point (6G and beyond) will need to adopt large scale transceiver arrays with a combination of multi-input-multi-output (MIMO) theory and fully digital multi-beam beamforming. The resulting high gain array factors will overcome the high path losses at mmW bands, and the simultaneous multi-beams will exploit the multi-directional channels due to multi-path effects and improve the signal to noise ratio. Such access points will be based on electronic systems which heavily depend on the integration of radio frequency (RF) electronics with digital signal processing performed in field programmable gate array (FPGA)/ RF system-on-chip (SoC).

This dissertation is directed towards investigation and realization of fully-digital phased arrays that can produce wideband simultaneous multi-beams with FPGA or RF-SoC digital back-ends. The first proposed approach, a spatial bandpass (SBP) infinite impulse response (IIR) filter-based beamformer, is based on the concepts of space-time network resonance. A 2.4-GHz 16-element array receiver has been built for real-time experimental verification of this approach. The two other approaches

are based on discrete Fourier transform (DFT) theory and and a lens-based approach, lens plus focal planar array theory, which is essentially an analog model of DFT. These two approaches are verified for a 28 GHz, 800 MHz mmWave implementation with RF-SoC as the digital back-end. It has been shown that for all proposed multi-beam beamformer implementations, the measured beams are well aligned with the simulated beams. The proposed approaches differ in terms of their architectures, hardware complexity and costs. This dissertation also presents an application of multi-beam approaches for RF directional sensing applications to explore white spaces within the spatio-temporal spectral regions. A real-time directional sensing system is proposed to capture the white spaces within the 2.4-GHz Wi-Fi band.

Further, this dissertation investigates the effect of electro-magnetic (EM) mutual coupling in antenna arrays on the real-time performance of fully-digital transceivers. Different algorithms are proposed to uncouple the mutual coupling (MC) in digital domain. The first one is based on finding the MC transfer function from the measured S-parameters of the antenna array and employing it in a Frost finite impulse response (FIR) filter in the beamforming backend. The second proposed method uses fast algorithms to realize the inverse of mutual coupling matrix via tridiagonal Toeplitz matrices having sparse factors. A 5.8 GHz, 32-element array and 1-7 GHz, seven-element tightly coupled dipole array (TCDA) have been employed to demonstrate the proof-of-concept of these algorithms.

TABLE OF CONTENTS

CHAPTER PAGE

1. INTRODUCTION 1
1.1 Motivation 2
1.2 Contributions of this Dissertation 8
1.3 Publications 11
1.4 Dissertation outline 11
1.5 Scientific collaborators 16

2. REVIEW OF RF BEAMFORMING THEORY AND TECHNIQUES . . . 19
2.1 Spatio-temporal plane waves 19
2.2 2D ST plane-wave spectrum and its properties 23
2.3 Uniform linear arrays to spatially sample 2D STPWs 24
2.4 Spatial filter requirements 25
2.5 Beamforming or spatial filtering techniques 28
2.5.1 Beamforming implementation with fixed weight set 30
2.5.2 Multi-beam beamformers implementation 31
2.6 Conclusion 33

3. MULTIBEAM ARRAY RECEIVER USING 2D SPATIALLY BANDPASS DIGITAL IIR FILTERS 34
3.1 Background 34
3.2 Evolution of first-order 2D IIR SBP beam filters 38
3.2.1 Architecture and implementation of the 2D IIR SBP filter 40
3.2.2 First-order 2D IIR SBP multiband trapezoidal filter 41
3.3 Proposed filter validation with a 16-element 2.4-GHz I-Q array receiver . 45
3.3.1 Antenna array, RF front-end, and digital systems setup 46
3.3.2 Measurement setup and limitations 48
3.3.3 Measured beams 48
3.3.4 Contribution and comparison to previous work 50
3.4 Conclusion 52

4. MULTI-BEAM BEAMFORMING USING FAST FOURIER TRANSFORM 53
4.1 Background 54
4.2 Development of a 28-GHz 32-element digital receiver array 56
4.2.1 Design specifications and constraints 57
4.2.2 Front-end design 57
4.3 Design of a four-point FFT multi-beam beamforming receiver at 28 GHz 61
4.3.1 Patch antenna design 62
4.3.2 Patch antenna array 64
4.3.3 Receiver chain 65
4.3.4 Digital back-end 66

4.3.5 Four-point FFT digital design . . . 69
4.3.6 Real-time beamforming and measurement setup . . . 70
4.3.7 Calibration . . . 71
4.3.8 Real-time beam measurements . . . 72
4.4 Contribution and comparison to previous work . . . 73
4.5 Conclusion . . . 74

5. MULTI-BEAM BEAMFORMING USING LENSES AND FOCAL PLANE ARRAYS . . . 76
5.1 Background . . . 77
5.2 Architecture of multi-beam beamforming using lens and FPA assembly . 78
5.3 Design of a four-element, 28-GHz multi-beam beamformer . . . 79
5.3.1 Lens design . . . 79
5.3.2 28-GHz digital array receiver specifications . . . 80
5.3.3 Measurement setup for 28-GHz lens . . . 82
5.3.4 Measured 28-GHz lens + FPA digital beams . . . 84
5.3.5 Simulated 28 GHz beams using lenslets . . . 86
5.4 Contribution and comparison to previous work . . . 87
5.5 Conclusion . . . 88

6. REAL-TIME FPGA BASED MULTI-BEAM DIRECTIONAL SENSING 90
6.1 Background . . . 90
6.2 ROSs of the spectra of plane waves and white spaces . . . 91
6.3 Sensing over multi-beams . . . 93
6.4 Design of a 16-element FFT multi-beam based directional sensor for 2.4 GHz Wi-Fi sources . . . 94
6.4.1 RF receiver array setup with 16-point FFT beamformer . . . 94
6.4.2 Multi-beam directional energy detectors . . . 95
6.4.3 Average 2D FFT-based power spectral density function . . . 96
6.4.4 Experimental setup . . . 97
6.4.5 Control experiments with known sources and directions . . . 99
6.4.6 Real-world measurements . . . 100
6.5 Conclusion . . . 102

7. DIGITAL MUTUAL COUPLING COMPENSATION USING FROST FIR FILTERS . . . 103
7.1 Background . . . 104
7.2 Signal processing model . . . 106
7.2.1 Three dimensional mutual coupling transfer function for uniform planar arrays . . . 107
7.2.2 Frost 3D FIR beamformer . . . 110
7.2.3 Frequency-dependent array factor . . . 111

7.2.4 Proposed design with compensation of MC . . . 112
7.3 Design of complex-coefficient FIR filters . . . 113
7.4 Experimental validation of 2D FIR MC compensated beamformer . . . 114
7.4.1 Receiver array setup . . . 115
7.4.2 Experimental setup and beam measurements . . . 116
7.4.3 Limitations . . . 116
7.4.4 Discussion . . . 117
7.5 Experimental validation of 3D FIR MC compensated beamformer . . . 118
7.5.1 Antenna array design . . . 118
7.5.2 Receiver chain and digital back-end . . . 120
7.5.3 Measurement setup and beam measurements . . . 121
7.5.4 Limitations . . . 123
7.6 Contribution and comparison to previous work . . . 124
7.7 Conclusion . . . 125

8. DIGITAL MUTUAL COUPLING COMPENSATION USING FAST ALGORITHMS . . . 126
8.1 Background . . . 126
8.2 Structured coupling matrix . . . 128
8.2.1 Structural properties of the coupling matrix . . . 128
8.3 Uncoupling the mutual coupling . . . 130
8.3.1 Brute-force computation . . . 131
8.3.2 Fast algorithms . . . 132
8.4 Experimental verification . . . 134
8.4.1 Antenna array and S-Parameter measurement . . . 134
8.4.2 Microwave receivers and digital back-end . . . 134
8.4.3 Measurements . . . 137
8.5 Contribution and comparison to previous work . . . 138
8.6 Conclusion . . . 139

9. CONCLUSIONS AND FUTURE WORK . . . 140

BIBLIOGRAPHY . . . 144

VITA . . . 161

LIST OF TABLES

TABLE PAGE

3.1 Comparison between Simulated and Measured RF Beams 50

4.1 Components and specifications for the mmW receiver design 60

4.2 Specifications for the patch antenna 62

4.3 Dimensions for the Patch Antenna Design 63

7.1 SL Level Reductions Achieved with the Proposed Approach 117

8.1 Beam performance improvement using the proposed method 137

LIST OF FIGURES

FIGURE PAGE

1.1 The evolution of mobile communications [1] 1

1.2 Possible applications of MIMO + multi-beam beamforming (a) in a blocked LOS path; (b) to improve SNR when LOS is available by using multi-path techniques, and to connect across corners in an urban environment. 4

1.3 (a) Satellite communication with multi-beam beamforming covering wider geographical areas [2]. (b) Starlink constellation of cubesats and utilization of adaptive multi-beam beamforming to track neighbor cubesats in motion and perform data transfers and handovers [3]. . 5

2.1 Propagating EM waves emitted from a source can be approximated as plane waves in its far-field region. Such plane waves in 3D space are described as a function of space and time by w_{PW}. 20

2.2 (a) 2D signal processing by a linear array of antennas; (b) 3D signal processing by a rectangular array of antennas. 21

2.3 (a) STPW propogating in 2D (space-space) domain; (b) STPW propogating in 2D (space-time) domain; (c) Light cone demonstration; (d) ROS of the STPW aligned along spatio-temporal DOA. 22

2.4 Relevance of spatial frequency to direction of arrivals of STPW. In all plots, the x-axis refers to spatial element index and y-axis to the normalized by 'c' time samples. Spatial frequency is the frequency of the wavefront observed from x-axis. 24

2.5 2D mixed-domain (ω_x, Ω_{ct}) frequency spectrum of three broadband Gaussian-modulated cosine pulses. 26

2.6 (a) RoS of the ST broadband bandpass PWs received by a ULA (b) RoS of the ST broadband bandpass PWs following I-Q downconversion. (c) RoS of the ST broadband bandpass PW following I-Q downconversion and downsampling. 27

2.7 Beamforming architectures: 1) Analog beamforming, 2) Digital beamforming, 3) Hybrid beamforming. 28

2.8 Receive mode model of an N-element phased array. 29

2.9 Mutibeam beamforming architectures: (a) analog beamforming (b) digital beamforming (c) hybrid beamforming. 32

3.1 (a) RoS of the ST broadband bandpass PWs received by a ULA; (b) RoS of the ST broadband bandpass PWs following I-Q downconversion; (c) RoS of the ST broadband bandpass PW following I-Q downconversion and downsampling. 35

3.2 (a) A 2D resistively terminated passive prototype network with spatial inductor L_x and temporal inductor L_{ct}; (b) A 2D magnitude response of filter $H(s_x, s_{ct})$, and (c) A 3D view of the frequency response in (b). 36

3.3 Magnitude response of (a) first-order and (b) second-order 2D IIR SBP filter for $\theta = -30°$. 39

3.4 (a) Direct-form I implementation of the first-order single-band 2D IIR SBP beam filter. (b) Systolic array architecture of the proposed IIR filter accepting digitized I-Q inputs from the array receiver. 42

3.5 Structure for the filter-bank of a 2D SBP multiband trapezoidal filter. . 43

3.6 (a) Magnitude response of the 2D IIR multiband trapezoidal filter $H_{IIR}(z_x, z_{ct})$; (b) cross section of (a) at $\omega_{ct} = 0$. 44

3.7 Architecture of the test setup for verifying the 2D IIR SBP beam filter. 45

3.8 (a) The overall experimental setup; (b) RF receiver chain implemented using commercial-off-the-shelf components; (c) ROACH-2 FPGA–based digital back-end. 47

3.9 Measuring the filter beam patterns from the RF receiver setup placed inside a parking garage. 48

3.10 Measured beam patterns vs. the fixed-point simulated beam patterns of (a) 2D IIR SBP filter having passbands at $-10°$ and $-35°$; (b) 2D IIR SBP filter having passbands at $-15°$ and $-40°$. The fixed point simulated beams are generated from the digital design from Matlab Simulink and do not incorporate any microwave effects. 49

4.1 (a) 2D frequency response of the I-Q downconverted, downsampled STPW. The red path indicates the ideal passband required by the beamformer, (b) Frequency response of an eight-point DFT filter-bank. 55

4.2 System overview: a 16×16 beamforming+MIMO access point for 28-GHz OFDM. 58

4.3 Architecture of the single receiver chain of the proposed mmW heterodyne receiver array. 60

4.4 (a) Geometry of the designed antenna sub array (b) CST-simulated return loss (c) CST-simulated polar pattern of the sub-array at 28 GHz. Note that the polar pattern is along the axis of the array i.e., in the elevation plane. 63

4.5 (a) Close-up image of the fabricated antenna sub-array. (b) Measured return loss of the fabricated antenna. 64

4.6 A four-element ULA developed from the single patch subarray with an inter-element spacing of 8 mm. 65

4.7 (a) Four-element receiver array front-end with HMC1065LP4E I-Q down-converter. (b) Functional block diagram of HMC1065LP4E [4]. (c) Receiver array mounted on a rotating platform 66

4.8 (a) RF-SoCs Quad RF-ADC tile overview (b) PLL clocking system in RF-SoC data converter chip. Taken from [5]. 68

4.9 RF SoC digital back-end used for the implementation of four-point FFT beamformer at 28-GHz. 69

4.10 Architecture of the digital back-end with a four-point FFT digital core. Each core is realized in a polyphase manner to support wide bandwidths. 70

4.11 A 28-GHz transmitter and receiver array setup for taking measurements. 71

4.12 (a) The sampled I and Q channels of each baseband signal at an IF of 100 MHz. (b) The digitally-calibrated channels fed to the digital beamforming cores. 72

4.13 Four-point FFT real-time digital multi-beam beamforming at 28 GHz. Simulated and measured beam patterns corresponding to each output of the FFT multi-beam beamformer at $f_{IF} = 100$ MHz. 73

5.1 Architecture of a lens + focal planar array (FPA)–based multi-beam beamforming. 78

5.2 Validation of the lens + 1D array using full-wave electromagnetic simulations using CST studio suite. (a) Designed lens structure along with dimensions. Parameter x_o was varied as $x_o = -12, -4, 4, 12$ mm to emulate the beams radiated by the four 1D arrays. (b) 3D printed lens used for measurements. 3D beams with peak at $\theta = 4^o$, 12^o resulting due to $x_o = 4$ and 12 mm are shown in (c) and (d) respectively. For $x_o = -12, -4$ mm cases, beams in opposite directions were obtained (not shown). 81

5.3 (a) Experimental setup with digital back-end RF SoC system and local oscillator (b) Receiver chains for the four-element FPA (and aperture array) with array taped to the base of the ABS plastic lens. The LO is split four-ways using a microwave divider network. 83

5.4 (a) Simulated normalized gain patterns of the beams using fullwave electromagnetic simulation using CST studio suite. Elemental subarray gain pattern (normalized by the maximum of beam pattern) is shown for comparison. (b) Measured normalized gain patterns of the beams extracted from RF SoC and corresponding normalized elemental subarray pattern. 84

5.5 System overview of cascaded Lens + FPA multibeam beamformer to generate sharper beams. 85

5.6 (a) Simulated beam patterns from lens+FPA setup for a lenslet array. (b) Simulated beam patterns obtained from cascaded lens+FPA setup using measured lens beam data. 86

6.1 (a) An RF signal received by a ULA; (b) The ROS of the spectrum of a plane wave signal in the 2D frequency domain. 92

6.2 (a) The ROS of the 2D spectrum of a quadrature-sampled plane wave; (b) ROSs of the spectra of plane waves and white spaces. 93

6.3 (a) Theoretical RF beams corresponding to the spatial FFT outputs; (b) the experimentally measured beams using a fixed-point implementation of the 16-point FFT. 95

6.4 Digital architectures for directional sensing of RF sources; (a) multibeam directional energy detector; (b) average 2D FFT-based PSD function. 98

6.5 (a) Different situations in which measurements are performed; (b) measurements for the case of known RF sources; (c) real-time measurements using Wi-Fi access points. The detected energy is subjected to thresholding to make a binary decision for spectral occupancy. . . 99

7.1 Structure of a Frost beamformer [6] implemented for a $N_x \times N_y$ UPA. The coefficients $\beta_{i,j,k}$ can be derived to realize either a true-time-delay beamformer or a more generic 3D FIR frustum filter, while taking into account the effect of MC such that the effect of MC is de-embedded in the resulting array pattern. 106

7.2 Measured S-parameters of a tightly coupled 5×5 uniform rectangular array showing (a) coupling between elements within a row ULA (b) coupling between two row ULAs. (c) Frequency response of the 3D MC transfer function in (7.1) for this TCA considering $\eta = 13$ as the reference element in the 25×25 coupling matrix $\mathbf{K}_c$. 107

7.3 The 5.8-GHz 32-element antenna array setup used for experimentally verifying the 2D case of the proposed MC compensated Frost beamformer. 114

7.4 Measured beam patterns in comparison with the ideal beam patterns for cases (a) 10-MHz IF signal; (b) 20-MHz IF signal; (c) 30-MHz IF signal for the 5.8-GHz 32-array 2D FIR filter implementation. . . . 116

7.5 Setup for TCDA array measurements. A seven-element ULA (part of the 7×7 TCDA) was connected to broadband receivers (1-6 GHz). 118

7.6 Fabricated dual polarized microstrip TCDA (left) with infinite array active VSWR (right), showing VSWR <3 scanning down to 60° in the principle (E/H) and diagonal (D) planes. 120

7.7 Experimental setup for measuring the filter beam-patterns using the TCDA array. 122

7.8 Measured beam patterns in comparison with the ideal beam patterns for (a) IF = 100-MHZ, Scanning angle=−10 degrees; (b) IF=100-MHZ, Scanning angle= −20 degrees. 122

8.1 Overview of the proposed real time mutual uncoupling architecture. . . 127

8.2 The signal flow graph corresponding to $N = 8$. 130

8.3 (a) A 32-element 5.8-GHz receiver front-end used for the experimental verification; (b) Close up of one PCB fabricated receiver chain (c) ROACH-2 FPGA platform used as digital back-end; (d) Measurement setup. 133

8.4 Measured S-parameters (return loss and mutual coupling) for seven-central elements of the designed antenna array. 133

8.5 Comparison of measured beam patterns corresponding to all the eight bins of the spatial FFT based beams with and without mutual coupling compensation. 136

CHAPTER 1

INTRODUCTION

It is an exciting time for wireless communications! At this point of time, we can all agree on the fact that wireless networks are omnipresent. Development of new mobile technologies introduced different wireless services, which has caused smart devices to become widely known and has attracted new users. Owing to advances in the wireless field, there is a constant increase in the amount of data-traffic and device connections. It was predicted that the number of mobile connections would surpass 100 billion by the year 2020 [7]. This increase in demand for wireless connectivity led to massive modifications to the cellular infrastructure, and in just over four decades, mankind has witnessed the evolution of five generations of mobile communications from first generation (1G) to fifth generation (5G) as shown in Fig. 1.1. All these advancements aim at providing smooth and flawless mobile connectivity between users that significantly improve their daily lives.

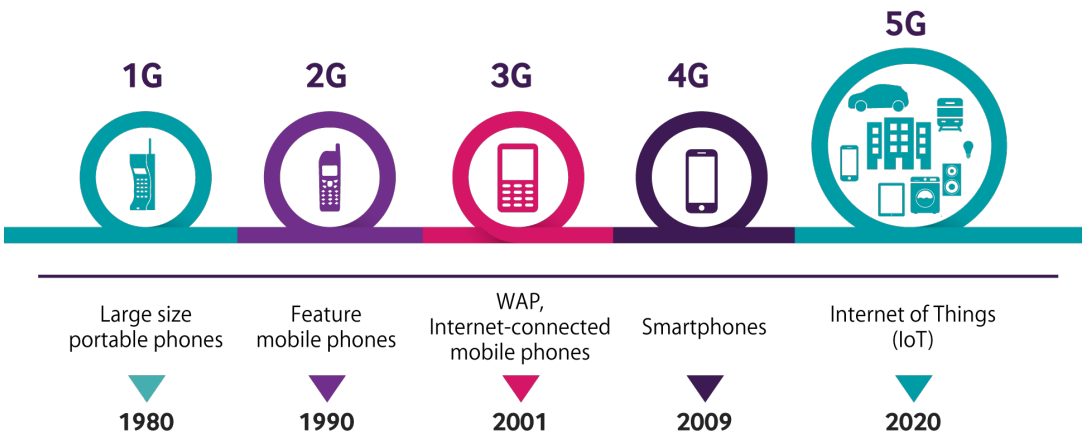

Figure 1.1: The evolution of mobile communications [1]

1.1 Motivation

Mobile technologies up to fourth generation (4G) utilized only the lower frequency bands such as microwave sub-6 GHz bands, where the channel bandwidths are typically 20 MHz for a connection [8]. Subsequently, this led to global scarcity in the available spectrum and demands to leverage the unused spectrum at higher frequencies. This motivated the exploration of the mm-wave (mmW) frequency spectrum, and mmW-enabled mobile communications are now at the verge of becoming reality. The benefits of adopting mmW systems for wireless communications has been well known for a long time as reported in [9, 10], and they have finally garnered enough interest to become a part of 5G infrastructure. The frequency spectrum specified by the International Telecommunication Union (ITU) for 5G communication includes the bands 3.4–3.6 GHz, 5–6 GHz, 24.25–27.5 GHz, 37–40.5 GHz, and 66–76 GHz [11], while the Federal Communications Commission (FCC) has specified the 27.5–28.35 GHz frequency band for 5G [12]. This spectrum allocation is aimed at densely connecting both people and the Internet of Things (IoT), to achieve higher levels of efficiency and data rates as compared to existing 4G long-term evolution (LTE) and Wi-Fi networks. The communication links envisaged for 5G wireless networks are expected to exhibit ultra-low latency (less than 1 ms) [13], enrich crowded connections and provide enhanced spectral energy. In addition, it will support a multitude of services and devices, with a range of brand new applications that includes but is not limited to augmented reality, virtual reality, security/surveillance, autonomous cars, remote health-care, and much more [14, 15].

Nevertheless, the challenge associated with the transition from 4G to 5G is that the radio transceiver front-end needs to be redesigned, since the mmW 5G links are now subjected to a completely new radio-propagation environment [16]. Also,

the blockage of EM waves at mmW frequencies will tremendously affect their power values owing to Friis' path loss formula, and will considerably reduce the signal-to-interference and noise ratio (SINR) [8]. High-gain directional antennas can be used at both the transmitting and receiving ends to circumvent these path losses, resulting in a significantly enhanced SINR. [17, 18]. However, directional antennas with narrow beams are applicable to long-range mm-wave point-to-point communications with a line-of-sight (LOS) link and become unsuitable for multiuser mobile communications, as they provide only limited spatial coverage [19–21]. Moreover, directional beams need to be steered either electronically or mechanically to obtain a better substitute link for non-LOS communications [20]. This beam steering technique is widely known as *beamforming*. Mechanical beam steering is rarely used now because it is bulky, cumbersome and has a non flexible architecture. Instead, front-ends use antenna arrays that apply signal processing techniques for directional transmission/reception of electromagnetic (EM) waves and thus achieve electronic beam steering. This technique of utilizing an array of sensors in conjunction with signal processing algorithms is called *spatial filtering* [22]. With advent of 4G and 5G wireless communications, beamforming has drawn great deal of attention, as it is one of the critical requirement for 5G applications [23–26].

However, as mentioned before, directional antennas are prone to have less spatial coverage, and such systems have reduced performance levels without an LOS path. Thus, communications at mmW necessitate multi-beam beamforming in order to utilize the complex urban wireless channels that suffer from occlusions, path loss, and multi-path effects [27]. Next-generation wireless access points will likely employ a combination of multi-input-multi-output (MIMO) theory with multi-beam fully-digital beamforming [26, 28–31]. The high-gain array factors provided by very sharp beams will be required for overcome high path losses and mitigate environ-

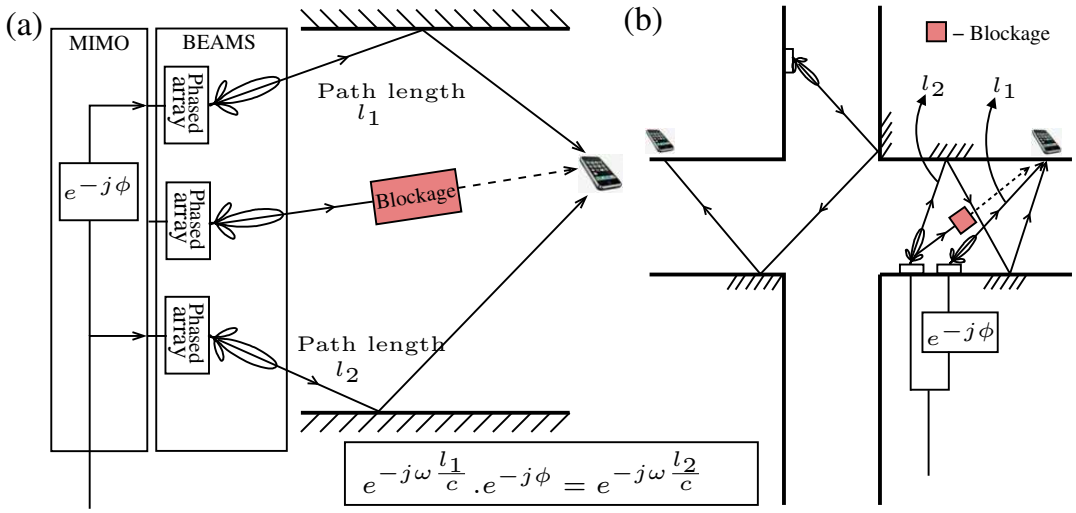

Figure 1.2: Possible applications of MIMO + multi-beam beamforming (a) in a blocked LOS path; (b) to improve SNR when LOS is available by using multi-path techniques, and to connect across corners in an urban environment.

ment attenuation due to absorbing gases (e.g., oxygen at 60 GHz), rain, hail, dust, and other opaque objects (trees, humans) that degrade the signal-to-noise ratio (SNR) at the receiver [19]. These networks will exploit both the massive bandwidth available in the mmW bands and the high SNR available due to the use of high-gain antenna arrays to achieve spectral efficiency via orthogonal frequency division multiplexing (OFDM) [32]. In particular, the high SNR that can be achieved with digital beamforming will allow quadrature amplitude modulation (QAM) with up to 1024 discrete constellation points per OFDM sub-carrier. As discussed in one of our recent works [33], the combination of MIMO techniques with fully-digital multi-beam beamforming allows coherent combination of several ray-like channels (from the sharp beams) to achieve several important capabilities, such as 1) connecting when LOS is not available due to channel blockage, 2) connecting across corners in a densely built environment (e.g., downtown Miami/ New York City), and 3) coherent combination of multiple ray-like channels to improve SNR even when LOS is available. These scenarios are illustrated in Fig. 1.2 [33]. Multibeam beamforming

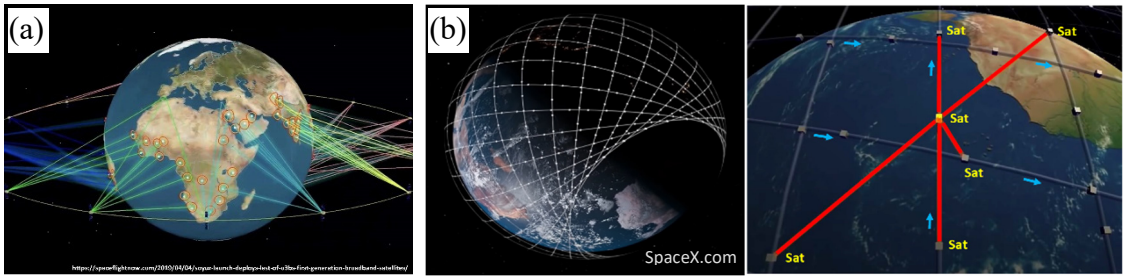

Figure 1.3: (a) Satellite communication with multi-beam beamforming covering wider geographical areas [2]. (b) Starlink constellation of cubesats and utilization of adaptive multi-beam beamforming to track neighbor cubesats in motion and perform data transfers and handovers [3].

on linear/rectangular apertures is thus important for exploiting multi-directional channels in massive-MIMO systems.

Further, mmW applications are emerging relevant to defense systems, such as space-based mesh networks between low earth orbit satellites, cross-platform high-capacity data connectivity (air/space/land/sea) and electronic warfare [14, 19, 21]. Satellite communications with multibeam beamforming enables wider coverage areas, thus increasing the number of simultaneous users as shown in Fig. 1.3(a). In addition, SpaceX's Starlink satellites that guarantee ultra-fast internet connections feature four phased array antennas to increase the data throughput [3]. These cubesat satellites are arranged in a constellation as shown in Fig. 1.3(b), must maintain connection with their five nearest neighbors in order to achieve successful data transfers and handovers [3]. Hence, they would require adaptive multi-beam beamforming to track the moving cubesats. These scenarios are listed in Fig. 1.3. All these applications demand multi-beam beamforming networks that can accommodate massive number of high-bandwidth beams. Because of this, recently Defense Advanced Research Project Agency (DARPA) have recently called a separate program (the MIDAS program) that is dedicated to real-time mm-wave (18–50 GHz

band) digital multi-beam beamforming to enhance secure communications between military platforms [34]. One crucial step in implementing these mmWave systems is to provide critical timing functionality and high-rate element-level processing in the digital back-end. Xilinx radio frequency (RF) system-on-chip (SoC) devices are currently the state-of-the-art digital signal processing back-ends that are capable of sampling a 100 MHz signal with sub-nanosecond timing. They provide the flexibility to meet the needs of multiple wireless applications, for example in the development of holographic radars that demand state-of-the-art processors to enable rapid adaptivity of the digital back-end circuits [35].

By utilizing the Xilinx RF-SoC analog-to-digital converters (ADCs) that are capable of sampling in GHz range, wideband fully-digital beamfilters with more than 2 GHz bandwidth are on the verge of becoming reality. Also, the antenna engineers are coming up with designs that assume a small form factor while providing huge bandwidths, such as a tightly coupled dipole array [36]. However, due to smaller physical area, the mutual coupling between the antenna elements for lower frequency bands tends to be higher and directly reflects the real-time performance. Although a plethora of array factors can be realized with fully digital approaches, the real-time performance on an array of antenna elements is thus typically reduced due to the non-ideal effects present in real-world antenna systems, particularly electromagnetic mutual coupling (MC) between neighboring elements. The impedance mismatches between the antennas and the low-noise amplifiers (LNAs) across the radio band of interest cause significant deviation of the measured performance compared to theoretical best-cases scenarios developed in computer based simulations. For high-performance receiver arrays, the MC can significantly impact the stop-band performance i.e., the side-lobe (SL) level and nulls of the receiver.

Considering how noisy and lossy the wireless communication channel can be, we need to improve the array performance whenever possible. The channel is time-varying but the RF transceiver systems are under our control and, hence, it is critically important that the noise, EM interference and the non-ideal effects introduced by our system are kept to minimum. Generally, it is the amplifiers, and mixers (which introduce harmonics, inter-mods, and DC offsets) cause degradation to real-time performance [37]. However, in case of wide-band arrays such as tightly coupled dipole array (TCDA) [36], it is the mutual coupling between these antennas that plays a crucial role in affecting the beam performance. MC also has a significant impact on the array active reflection co-efficient Γ_{act} in the antenna array that makes the design of LNA challenging [38]. Γ_{act} is beamformer-dependent (i.e., dependent on beam-direction) and differs from an isolated antenna-element reflection coefficient, as MC causes the distortion in the array pattern [38]. In addition, MC makes it impossible for LNA designers to simultaneously achieve input power match and noise match for all beam directions, thereby making array sensitivity beam-dependent [38]. Literature shows that using several approaches for mutual coupling reduction such as using low-scattering antennas [39], electromagnetic bandgap structures [40], split ring resonators [40], which are all implemented at the analog stage. But in this dissertation, we explore two digital approaches for MC compensation. One is based on finding the MC transfer function from the measured S-parameters of the antenna array and then employing it in a Frost finite impulse response (FIR) filter in the beamforming back-end. The second one uses novel fast algorithms to realize the inverse of the mutual coupling matrix via tridiagonal Toeplitz matrices having sparse factors.

1.2 Contributions of this Dissertation

A large portion of this dissertation is directed towards the implemention of phased arrays that can produce simultaneous multi-beams using both analog and digital networks. These front-ends are supported by highly sophisticated digital back-ends to support wider bandwidths. Further, we explore how one of these multibeam approaches is utilized in sensing applications. Finally, we investigate and validate different algorithms used for the mutual coupling compensation. The contributions of each topic are briefed described below:

Multi-beam Approach 1: The first approach is based on multi-beam beamforming using spatial bandpass (SBP) 2D infinte impulse response (IIR) digital filters. These IIR filters are multi-dimensional filters and are based on the concepts of space-time network resonant theory. The proposed filters provide a wideband response across the entire temporal bandwidth of the incoming signal at the antenna array and encompass a trapezoidal-shaped passband to filter out the desired 2D spatio-temporal broadband bandpass plane waves (PWs). The proposed filters are very low in complexity compared to the FIR-based implementations while achieving a wideband frequency response. Chapter 3 discusses the theory and realization of these filters. For proof of concept verification, a 16-element 2.4-GHz digital array receiver is designed and employed. A Reconfigurable Open Architecture Computing Hardware 2 (ROACH-2) field programmable gate array (FPGA) is used as the digital signal processor (DSP) to realize two simultaneous beams using the proposed SBP filter.

Multi-beam Approach 2: The second approach is based on aperture beamforming, which uses an antenna array receiver where a discrete Fourier transform (DFT) is used to create multiple beams. Orthogonal simultaneous multi-beams in theory can be achieved by employing a spatial DFT operation across a uniform linear array (ULA) antenna samples in receive/transmit mode. Chapter 4 discusses the theory behind the DFT-based beamforming and the implementation of a fully digital four-beam beamformer using a four-element array at 28-GHz. The digital multi-beam beamforming is accomplished using a Xilinx radio-frequency system-on-chip (RF SoC) platform that can support 2 GSps sampling of 16 analog input channels. The digital beamforming supports 845 MHz of bandwidth and is performed in a polyphase DSP architecture.

Multi-beam Approach 3: The third approach is based on a focal plane array (FPA) and lens assembly to achieve multi-beam beamforming. Dielectric lens antennas are of great interest because they allow high gain with beam steerability, when fed using a properly designed FPA feed. The FPA is located on the focal region of the lens, and it is connected to dedicated receivers (or transmitters) that are interfaced to digital receivers (or transmitters). This dissertation proposes to build and implement a lens+FPA-based multi-beam beamforming architecture at mmW frequencies to provide sharp and directed RF beams. Chapter 5 discusses the theory behind the lens+FPA-based beamforming and the design steps for its implementation. This approach is validated by employing a 4-element aperture array as a feed array for a high-gain ABS dielectric lens antenna. The lens is mounted onto the 28-GHz digital array receiver with RF SoC back-end to form multi-beams.

Multi-beams for Directional Sensing: We discuss the possibility of using one of the multi-beam beamforming approaches for RF spectrum sensing applications in Chapter 6. It discusses the exploration of the white spaces within the spatio-temporal spectral regions that can be used to fulfill our need to alleviate the spectral scarcity. By studying the network surroundings using directional sensing, the white spaces in the spatio-temporal spectral region can be used to fill in the wireless channels that are not being used efficiently. In this work, a 16-point FFT based multi-beam directional sensor is realized on the ROACH-2 digital platform to capture the white spaces within the 2.4-GHz Wi-Fi band.

Frost FIR filters based Mutual Coupling Compensation: This chapter discusses a wideband FIR-based digital beamformer design that de-embeds the effect of MC from the array factor leading to improved SL and null performance. A 3D spatio-temporal coupling transfer function is derived from the measured S-parameters of a uniform planar array (UPA). The theoretical formulations for designing a 3D complex-coefficient FIR filter, optimal in the minimax sense, are presented. Later, the 3D MC transfer function is employed in the 3D FIR filter design to de-embed the coupling effects. In particular, this chapter shows that this multi-dimensional filter design problem can be converted as a second-order cone programming problem. The proposed minimax design is the *first* optimizations-based design technique for 3D FIR filters having coefficients with complex values. The proposed models are validated for both 3D and 2D case using experiments on a sven-element TCDA operating in the frequency range of 1 to 7 GHz and a 32-element patch antenna array operating in the frequency range of 5.7 to 6 GHz, respectively.

Mutual Coupling Compensation based on a Fast Algorithm: Chapter 8 introduces us to a fast algorithm implemented on a digital hardware back-end suitable for real-time uncoupling of mutually coupled arrays. This algorithm finds the inverse of the mutual coupling matrix and is based on inversion of $N \times N$ tridiagonal Toeplitz matrices having sparse factors. To this end, a low-order coupling function is considered where each antenna is coupled to its two nearest neighbors. The proposed method can nevertheless be extended to higher-order coupling, albeit at increased system complexity. The proposed algorithm has been experimentally verified for an eight-element antenna array at 5.8-GHz.

1.3 Publications

The research outcomes from this dissertation has resulted five journal publications and twelve conference papers, which are listed in the vita at the end of the dissertation.

1.4 Dissertation outline

The rest of the dissertation is organized as follows:

Chapter 2 presents a review of propagating electromagnetic (EM) plane waves, also known as *space time plane waves* (STPW) as seen by antenna arrays. The work in this dissertation is based on spatial filtering of the space time waves, so this review chapter helps us to understand the concepts of beamforming and the methods used for its realization. Section 2.1 discusses STPWs propagating in 3D space and the relevant signal processing as received by uniform linear arrays and rectangular arrays. Sections 2.2 and 2.3 continue the discussion of the frequency

spectrum of 2D STPWs and shows how the spatial frequency is related to their direction of arrival. This section also describes the region of support (ROS) of the 2D STPWs frequency spectrum and the trapezoidal passband of the downconverted, downsampled RF signals. In Section 2.4 we investigate the requirements of spatial filters to enhance the desired STPW signals. Finally, Section 2.5 reviews the basic concepts of multibeam realization and presents an overview of their implementation topologies.

Chapter 3 proposes a multi-beam implementation topology based on IIR filters that are known to be 2D spatial bandpass (SBP) filters. The SBP digital beamfilters are derived from frequency planar (FP) filters, hence this chapter starts with a discussion of the evolution of FP IIR filters in Section 3.1. The frequency planar filters are wideband array processing algorithms that are based on the concepts of multi-dimensional space-time network resonance. Section 3.2 describes the evolution of 2D IIR SBP beam filters from the frequency planar filters. The proposed filter's transfer function is derived such that its magnitude response encompasses the trapezoidal passbands of the 2D broadband downconverted PWs. Sections 3.2.1 and 3.2.2 discuss the systolic array architecture of the proposed filters and hwo a multi-band approach is derived. Section 3.3 describes a 2.4 GHz, 16-element array designed and built for real-time verification of the proposed work. Section 3.3.1 provides details about the setup of the antenna arrays, RF front-end and digital systems. The discussion on the measurements of beam patterns, the filter's performance, and the hardware complexity is included in Sections 3.2.3 and 3.2.4.

Chapter 4 presents multi-beam beamforming using fast Fourier transforms (FFTs) and includes a four-element 28 GHz receiver array implementation with an RF-SoC digital back-end. It starts with a background on the mathematical properties of FFT and how they are utilized as spatial filters to realize simultaneous multi-beams.

Section 4.2 describes a 28-GHz, 32-element receiver array design for 5G wireless communication. The front-end design assumes a 16×16 beamforming MIMO access point with Xilinx RF-SoC performing the DSP. Section 4.2.1 presents the link budget and noise figure analysis for front-end design assuming 64 QAM modulation, 512 point OFDM to establish a wireless communication link with bit error probability better than 10^{-5}. Due to cost limitations, a four-element, 28-GHz receiver array realizing four beams is implemented. The antenna array design, receiver array and the digital back-end details are all presented in Sections 4.3.1 to 4.3.4. Section 4.3.5 describes a four-point FFT digital design implemented on an RF-SoC–based ZCU1275 hardware platform. The measurement setup and the calibration procedure to correct the RF front-end amplitude and phase mismatches are discussed in Sections 4.3.6 and 4.3.7. Finally, performance evaluation of the digitally measured beams in comparison with the simulated beams is presented in Sections 4.3.8.

An analog multi-beam beamforming approach is presented in Chapter 5. The contents of this chapter describe a lens and focal plane array assembly for a 28 GHz, four-element receiver array to achieve four simultaneous sharp beams. It starts by describing the motivation and background for the lens-based approach in Section 5.1. It continues with specifications of the system architecture using lenses and an FPA assembly to realize multi-beams. Section 5.3 provides details about the implementation of the proposed approach at 28 GHz. A lens made from ABS material is designed to achieve a directivity of 29 dBi, and a description of the lens design is provided in Section 5.3.1. The experimental setup of the digital back-end RF SoC system, receiver chains design is explained in Sections 5.3.2 and 5.3.3. This section also presents the full-wave EM simulations of the lens design performed in CST simulation software. The discussion of the simulated beams is also provided in this section. Section 5.3.4 discusses the measured 28-GHz lens + FPA digital

beams. The measured beams are compared with the beams simulated using CST and conclusions are drawn regarding ways to improve the gain enhancements due to lens. Finally Section 5.3.5 describes a hybrid beamforming approach using lenslets.

Chapter 6 explores the applications of beamforming for spectrum sensing. A real-time FPGA based multi-beam directional sensor based on FFT algorithms is proposed in this chapter. Section 6.1 gives a background on white spaces available in the spatio-temporal frequency domain. Section 6.2 continues the discussion by looking into the theory of directional sensing of EM waves emanating from an RF source. The ROSs of the spectra of plane waves and white spaces is revisited in this section. Section 6.3 demonstrate sensing over multi-beams using the spatial FFT approach. The chapter continues with a discussion of a 16-element, 2.4-GHz implementation of the multi-beam directional sensor to verify the proof-of-concept. Details about the 16-point FFT realized on a ROACH-2 digital platform are provided in Section 6.4.1. The theoretical RF beams and the experimentally measured beams are presented as well. Sections 6.4.2 and 6.4.3 describe the digital architectures of RF sources for 1D (direction only) and 2D (direction and frequency) applications. This dissertation is limited to 1D directional sensing only. Section 6.4.4 describes the experimental setup, and the preliminary measurements conducted with known sources and directions is explained in Section 6.4.5. Finally, the real-world measurements with 2.4-GHz Wi-Fi sources are presented in Section 6.4.6.

In Chapter 7, novel wideband Frost FIR filter-based digital beamformer design for mutual coupling compensation is proposed. Section 7.1 introduces us to mutual coupling (MC) and other non-ideal effects present in an array that can effect the real-time performance of large-scale, fully-digital phased arrays. A description of the signal processing model for developing the proposed filters starts in Section 7.2. Derivation of the mutual coupling transfer function for uniform planar arrays using

S-parameter based formulations is included in the Section 7.2.1. Section 7.2.2 describe the design and the transfer function of the Frost 3D FIR beamformer. The MC transfer function derived earlier is incorporated in the Frost FIR filter design to derive the transfer function of the proposed MC compensation beamformer. This is detailed in Sections 7.2.3 and 7.2.4. Section 7.3 describes the design of complex-coefficient FIR filters. In this Section, the 3D FIR filter design is formulated as a convex optimization problem, and the filter co-efficients are derived. Section 7.4 presents the experimental validation of a 2D FIR MC compensated beamformer. The 5.8-GHz, 32-element receiver array setup with ROACH-2 based digital back-end is described in Section 7.4.1. Section 7.4.2 presents the experimental setup and measured beams, while the limitations and performance improvement is discussed in Sections 7.4.3 and 7.4.4, respectively. We then move onto experimental validation of 3D case in Section 7.5. The TCDA antenna array design operating in the range of 1 to 6 GHz is described in Section 7.5.1. The rest of the experimental setup and digital back-end details are included in Sections 7.5.2 and 7.5.3. Beam measurements are carried out at 2 GHz with 100-MHz IF signal for two scanning angles. Section 7.5.3 includes performance evaluation of the proposed filter by comparing the measured beams and the ideal beams with and without the proposed mutual coupling technique.

Chapter 8 also presents a digital technique for mutual coupling compensation, which is based on fast algorithms and has lower digital complexity as compared to the FIR-based approach. Section 8.1 gives a brief background about the effect of MC on array performance. Section 8.2 introduces the structured coupling matrix K_c used to model the effect of mutual coupling, and Section 8.2.2 describes its structural properties and how the fast-algorithms can be used to implement the inverse of coupling matrix with low hardware resources. Section 8.3 presents the sig-

nal flow graph of the proposed fast-algorithm–based MC compensation technique. The details of the sparse factorization of the inverse matrix that uncouples the mutual coupling in the array is discussed in the same section. Section 8.4 discusses the experimental verification of the proposed approach by employing a 5.8 GHz, eight-element receiver array with ROACH-2 digital back-end. Microwave receiver designs, digital back-end details, and S-parameter measurements to model the coupling matrix are all discussed in Sections 8.4.1 and 8.4.2. Section 8.4.3 presents the array pattern measurements corresponding to all eight bins of spatial FFT with and without mutual coupling compensation.

Finally, Chapter 9 summarizes all the research work carried out in this dissertation and provides insights for future work.

1.5 Scientific collaborators

The work performed in the research study of this dissertation was carried out with multiple collaborations. Dr. Chamira Edussooriya at University of Moratuwa (Srilanka), who has expertise in advanced digital signal processing and design of multidimensional filters, collaborated on the work described in Chapters 3, 6 and 7. He contributed towards the mathematical analysis of multi-beam versions of the proposed 2D trapezoidal filters (Ch. 3). He helped in developing the theory required for exploring white-spaces in the 2D spatio-temporal spectrum (Ch. 6). He and his student (Ashira Jayaweera) collaborated in designing Frost FIR filter designs using minimax approach (Ch. 7). His major contribution towards this research study has led to several publications in IEEE International Microwave Symposium (IMS), Transactions on Aerospace and Electronic Systems, the Midwest Symposium

on Circuits and Systems (MWSCAS) and the Moratuwa Engineering Research and Conference (MerCON).

This research work was carried out in collaboration with several members of the RFCOM group at Florida International University. The work described in Chapters 5 and 7 were mainly conducted in collaboration with Dr. Shubhendu Bhardwaj. Dr. Bhardwaj has abundant experience in electromagnetic modeling, antenna designs, and novel mmWave and THz implementations. Particularly, the 28-GHz mmW lens used for analog multi-beam beamforming in Chapter 5 was designed by him. Dr. Elias Alwan and Dr. Satheesh Bojja Venkatakrishnan, two other distinguished members of this group, provided vital contributions by conducting technical reviews and providing insights on the RF and and mmWave system implementations in Chapter 4 and Chapter 7. Dr. Alexander Johnson of this very renowned group has extended his support by contributing a 7×7 dual-polarized tightly coupled dipole array designed by him for wideband STAR applications. This array is used in Chapter 7 for validation of the 3D mutual coupling compensation method. The collective effort of all these members is invaluable and has led to several publications in IEEE IMS, Microwave Transaction on Theory and Techniques (MTTS) and the international Workshop on Antenna and Technology (iWAT).

Dr. Chamith Wijenayake of the University of Queensland, Australia, with has expertise in MD signal processing algorithms and digital hardware architectures for wideband beamformers, extended his collaboration by providing mathematical analysis of beamfilters and several digital algorithms described in this dissertation. Specifically, he derived the mutual coupling transfer function from the S-parameters based approach in Chapter 7 and 8. This collaboration led to several publications in many conferences including but is not limited to IMS, MERCON, and TAES. Similarly Dr. Leonid Belostotski of the of the University of Calgary (Canada),

who has expertise in RF and mmWave circuits and systems, mixed-signal circuits, collaborated on the several publications related to the work done in Chapters 7 and 8. He also provided technical comments and reviews for those publications.

The mutual coupling compensation using fast algorithms was conducted in collaboration with Dr. Sirani Perera at Embry Riddle Aeronautical University. Dr. Perera is a distinguished researcher in the fields of low-complexity algorithms, wideband multi-beam antenna arrays and analog complementary metal-oxide semiconductor (CMOS) implementation. She proposed and derived the mathematical proofs for the fast algorithms discussed in Chapter 8.

Dr. Theodore S. Rappaport at New York University, who has expertise on wireless communications, MIMO, and 5G mmWave, also collaborated in several publications especially in the work related to mmWave multi-beam array receivers. He helped to evaluate the practical relevance of the 28-GHz multi-beam work in 5G and mmWave implementations.

CHAPTER 2

REVIEW OF RF BEAMFORMING THEORY AND TECHNIQUES

The contents of this work are based on spatial filtering techniques of space-time plane waves. The mathematical analysis of space-time plane waves received by an array of antennas is essential to completely understand the concepts of beamforming and its techniques. This chapter presents presents a review of the spectrum for propagating the plane waves, also known as spatio-temporal plane waves (STPWs), as seen by an antenna array in a receive mode beamformer. All the concepts related to to the receiver will apply to the transmitter due to the reciprocity nature of the antennas.

2.1 Spatio-temporal plane waves

Consider the wave propagation scenario between a transmit and receive antenna shown in Fig. 2.1. At any point in the far field[1] of an antenna the radiated wave can be represented by a plane wave whose electric-field strength is the same as that of the wave and whose direction of propagation is in the radial direction from the antenna [42]. As the radial distance approaches infinity, the radius of curvature of the radiated wave's phase front also approaches infinity; thus, in any specified direction, the wave appears locally as a plane wave as illustrated in Fig. 2.1. This is a far-field characteristic of waves radiated by all practical antennas. A spatio-temporal plane wave is a special case of a plane wave that is a function of two independent variables: space and time.

[1]Far-field is generally considered to be at a distance d from the transmitter, where $d > 2D^2/\lambda$, while λ is the wavelength of the wave in the propagating medium, and D is the aperture of the radiating antenna [41].

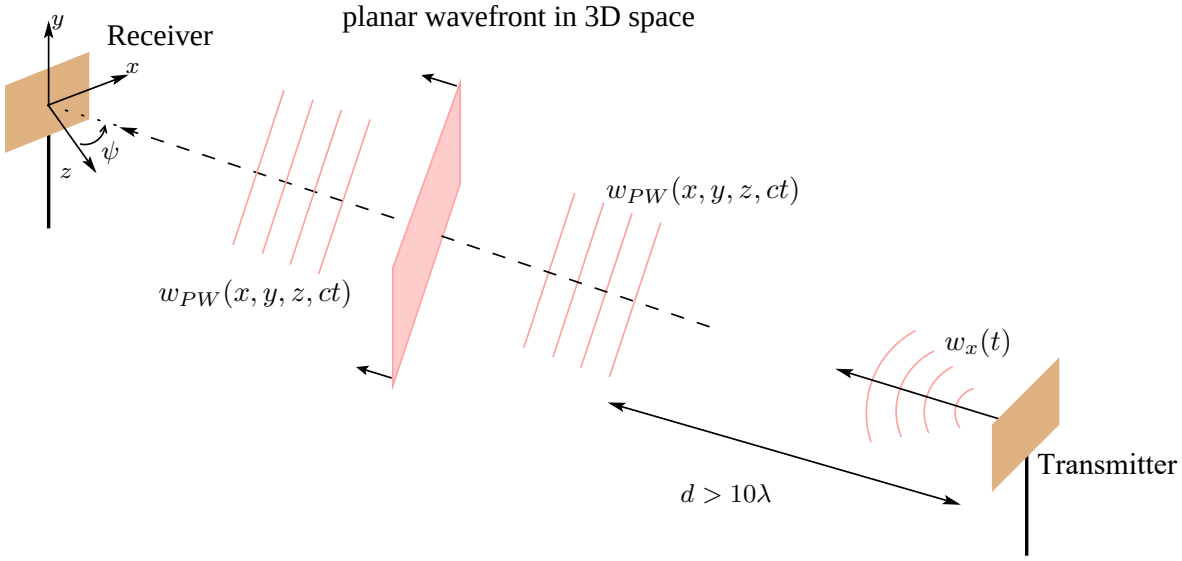

Figure 2.1: Propagating EM waves emitted from a source can be approximated as plane waves in its far-field region. Such plane waves in 3D space are described as a function of space and time by w_{PW}.

A time-varying plane-wave w_{pw} propagating in the 3D far-field space $\{x, y, z\} \in \mathbb{R}^3$ can be represented by a 4D spatio-temporal plane-wave $w_{pw}(x, y, z, t)$ [43] of the form given by the following equation:

$$w_{pw}(x, y, z, t) = s_{pw}(ct + d_x x + d_y y + d_z z), \tag{2.1}$$

where $\hat{d} = [d_x \; d_y \; d_z]$ is the unit vector specifying the direction of arrival (DoA) of the signal in the 3D space $\{x, y, z\} \in \mathbb{R}^3$ such that $d_x^2 + d_y^2 + d_z^2 = 1$, c is the wave propagation speed, and $s_{pw}(\lambda), \forall\, \lambda = ct + d_x x + d_y y + d_z z \in \mathbb{R}$ is the one dimensional 1D temporal intensity function [44, 45]. For each value of λ, $s(\lambda)$ corresponds to a 4D iso-surface in $\{x, y, z, ct\} \in \mathbb{R}^4$. The unit vector $\hat{d}$ can be expressed in terms of elevation angle ψ and azimuth angle ϕ as $\hat{d} = [\sin\psi\cos\phi \quad -\sin\psi\sin\phi \quad \cos\phi]$ [42].

A good demonstration of signal processing of the plane waves with different planar antenna configurations is shown in Fig. 2.2. A uniform linear array (ULA)

can process signals varying in single space vector and is a function of elevation angle ψ, whereas a rectangular array is a function of both elevation angle ψ and azimuth angle ϕ. The STPW signals received in a planar region, which is the uniform rectangular array in our case placed in the (x, y) region, can be expressed as shown in Eq. (2.2) by setting z in Eq. (2.1) to 0:

$$w_{pw}(x, y, t) = s_{pw}(d_x x + d_y y + ct). \tag{2.2}$$

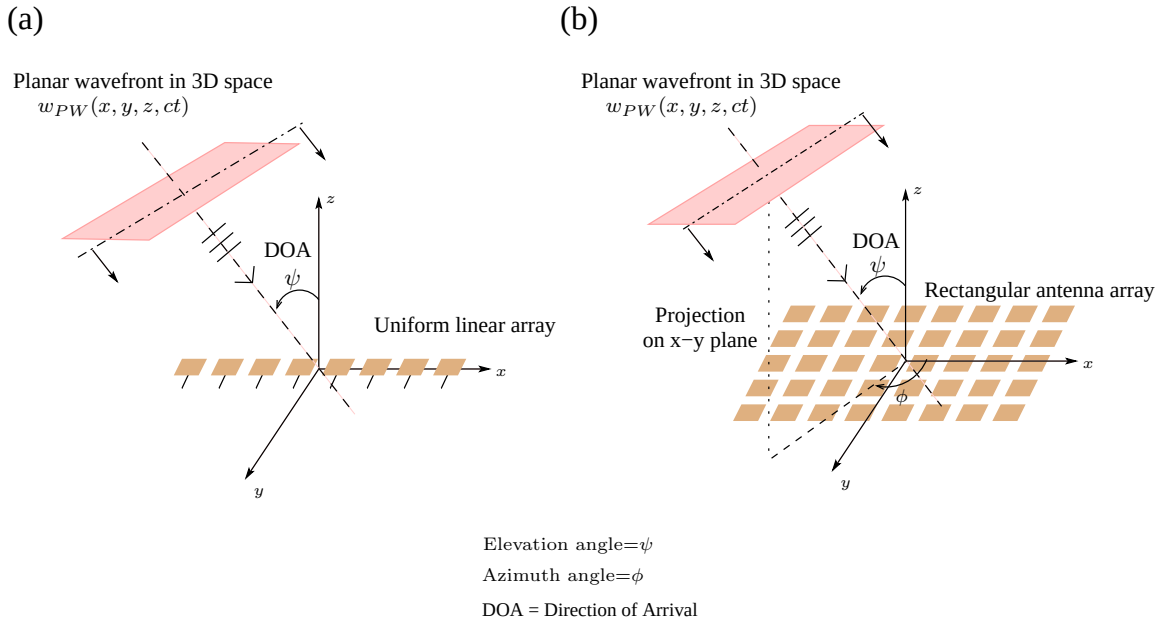

Figure 2.2: (a) 2D signal processing by a linear array of antennas; (b) 3D signal processing by a rectangular array of antennas.

Thus, the 4D hyper planar iso-surfaces of constant λ in Eq. (2.1) are simplified to 3D iso-surfaces in Eq. (2.3). For a ULA placed along the x axis, the 3D iso-surfaces simplify further to 2D iso-lines in the region $\{x, ct\} \in \mathbb{R}^2$ as given:

$$w_{pw}(x, ct) = s_{pw}(-(\sin\psi)x + ct). \tag{2.3}$$

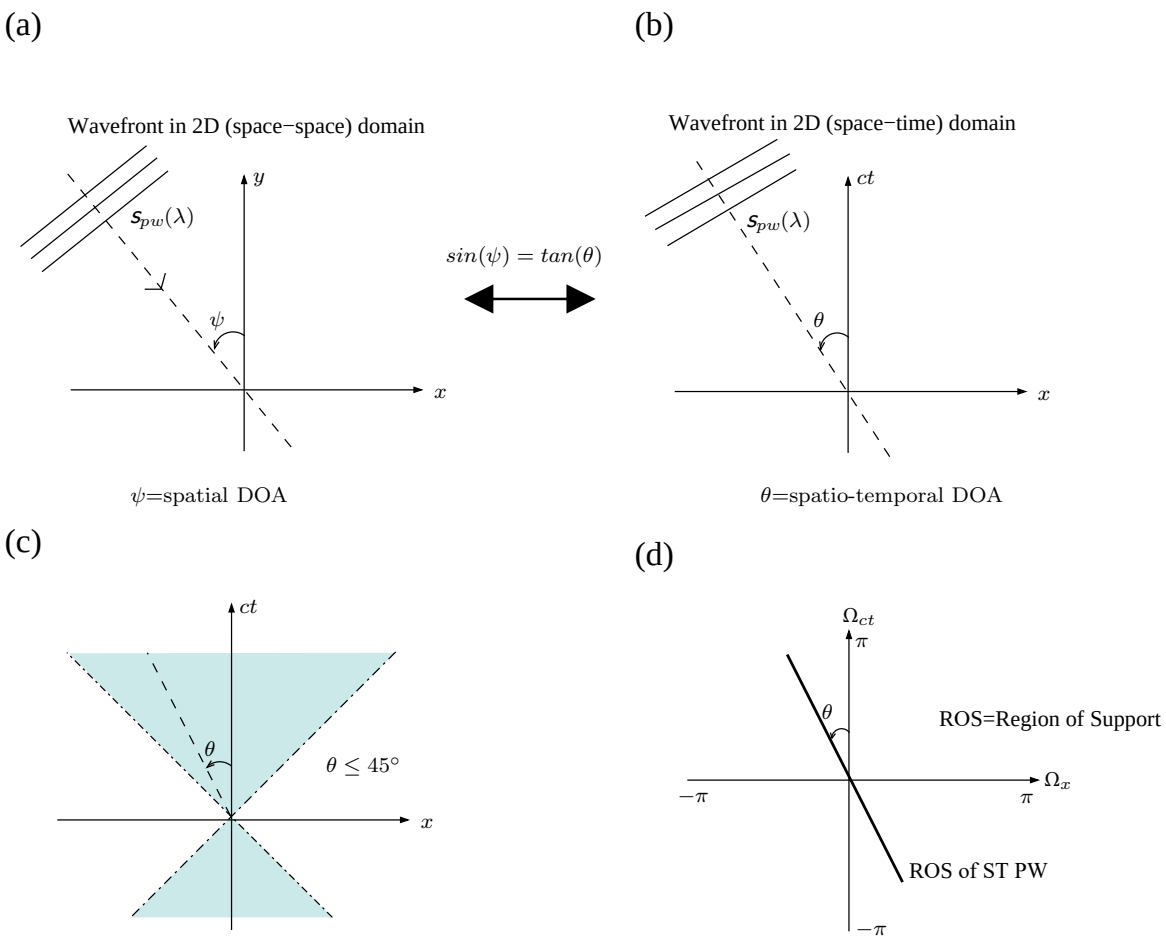

Figure 2.3: (a) STPW propogating in 2D (space-space) domain; (b) STPW propogating in 2D (space-time) domain; (c) Light cone demonstration; (d) ROS of the STPW aligned along spatio-temporal DOA.

The angle ψ is the spatial DOA i.e., the angle between the normal to the x axis (array) and normal to the plane wavefront as shown in Fig. 2.3 (a). Assuming the constant λ surfaces are now 2D iso-lines that contain a slope of $\tan\theta$ as shown in Fig. 2.3 (b), the spatial DOA ψ is related to the spatio-temporal DOA θ [43, 44] as given:

$$\tan\theta = \sin\psi. \tag{2.4}$$

Since the spatial DOA $|\psi| \leq 90°$, the spatio-temporal (ST) DOA is limited to

$|\theta| \leq 45°$. This illustrates that all plane-wave that are propagating in the 2D space-space with an angle ψ are confined to a 45° light cone in the spatio-temporal domain [45] as shown in Fig. 2.3 (c).

2.2 2D ST plane-wave spectrum and its properties

Since most of the work in this dissertation deals with ULAs, this section describes the theory and spectral properties of spatio-temporal plane-waves that are relevant to ULAs. The analysis will be conducted in continuous space-time domain, but it must be noted that, in practical cases, spatial domain is non-continuous because the STPW is sensed by antenna elements that are spaced at discrete locations along the array. To analyze the 2D frequency spectrum of the spatio-temporal PW given in Eq. 2.3, we apply the 2D continuous domain Fourier transform (CDFT). Let it be defined as $W_{pw}(\Omega_x, \Omega_{ct})$ and is given by:

$$W_{pw,2D}(\Omega_x, \Omega_{ct}) = \int_{-\infty}^{\infty} \int_{-\infty}^{\infty} w_{pw}(x, ct) e^{-j(\Omega_x x + \Omega_{ct} ct)} dx dct, \tag{2.5}$$

where $(\Omega_x, \Omega_{ct}) \in \mathbb{R}$ are the angular frequencies with respect to x and ct respectively [44]. Here $\Omega_{ct} = \Omega_t / c$ denotes the temporal angular frequencies of the STPW signal.

With reference to [43], the 2D CDFT in Eq. (2.5) can be further simplified to the expression given by:

$$W_{pw,2D}(\Omega_x, \Omega_{ct}) = S_{pw}(\Omega_t) c \Omega_{ct} \delta(d_x \Omega_{ct} - \Omega_x), \tag{2.6}$$

where $S_{pw}(\Omega_t)$ is the 1D continuous-time FT of the temporal signal $s_{pw}(t)$ and where $\delta(.)$ is the 1D impulse function. According to Eq. (2.6) it can be seen that the region of support (RoS) of the spectrum of 2D STPW is confined to a line in the (Ω_x, Ω_{ct})

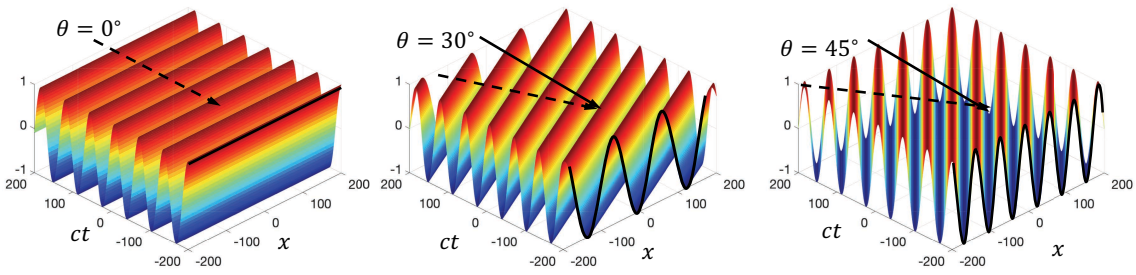

Figure 2.4: Relevance of spatial frequency to direction of arrivals of STPW. In all plots, the x-axis refers to spatial element index and y-axis to the normalized by 'c' time samples. Spatial frequency is the frequency of the wavefront observed from x-axis.

domain as shown in Fig. 2.3 (d) [44]. The ROS of a frequency spectrum is defined as the region where its magnitude is not defined to be zero.

Equation (2.6) indicates the region occupied by the desired STPWs and thus allows us to design beamfilters. Such a filtering technique is called *spatial filtering*. This concept is illustrated in Fig. 2.4 where the relevance of spatial frequency to beamforming is demonstrated. It assumes a 2D sinusoidal STPW arriving at different DoA towards a ULA placed on the x-axis. It is evident that different DoAs will result in different Ω_x values.

2.3 Uniform linear arrays to spatially sample 2D STPWs

Consider a ULA where the elements are spaced Δx apart is being illuminated by a 2D STPW $w_{pw,2D}(x, ct)$, then the spatially sampled ideal signal will be a mixed domain signal in (x, ct) and is given by $w_{pw,2D,m}(n_x, ct)$, where $n_x \in \mathbb{Z}$. The mixed domain FT can be defined for the Fourier transform pair, and it is given in the following equation:

$$W_{pw,2D,M}(\omega_x, ct) = \int_{t=-\infty}^{t=\infty} \sum_{n_x=-\infty}^{\infty} w_{pw,2D,m}(n_x, ct) e^{-j\omega_x n_x} e^{-j\Omega_{ct} ct} dct \tag{2.7}$$

where, $\omega_x = \Omega_x \Delta_x$. Using the reference in [46], the Eq. (2.7) can be expressed as follows:

$$W_{pw,2D,M}(\omega_x, ct) = \frac{1}{\Delta x} \sum_{n_x=-\infty}^{\infty} W_{pw,2D}\left(\frac{w_x - 2\pi n_x}{\Delta x}, \Omega_{ct}\right), \tag{2.8}$$

where $W_{pw,2D}$ is the 2D continuous domain Fourier transform of the 2D continuous domain STPW. From (2.8), it can be understood that the spatially sampled signal will have an infinitely repeating spectrum pattern with a periodicity of 2π along the ω_x axis. In order to avoid aliasing in the spatial frequency domain, the inter-element distance Δx should satisfy the following Nyquist criteria [46],

$$\Delta x \leq \frac{c}{2f_u} \tag{2.9}$$

where f_u is the maximum spatial frequency component in the received STPW and where c is the wave propagation speed. From [46], $f_u = f_{t,max} \sin\theta$, where f_t is the temporal frequency and θ is the DoA of the signal in the elevation plane.

2.4 Spatial filter requirements

From the previous discussion, we found that the RoS of the 2D STPW frequency spectrum lies on a straight line oriented at some angle (which is the corresponding DoA) to the Ω_{ct} axis, and thus spatial filters are required to contain their spectral passband within that RoS region. Such passbands can be generated by either analog or digital filter circuits. The conventional technique is based on phase-shifting; however, they are narrow band and contain the effect of beam squinting. For wideband filtering, the passbands should be frequency independent (i.e., it should be a

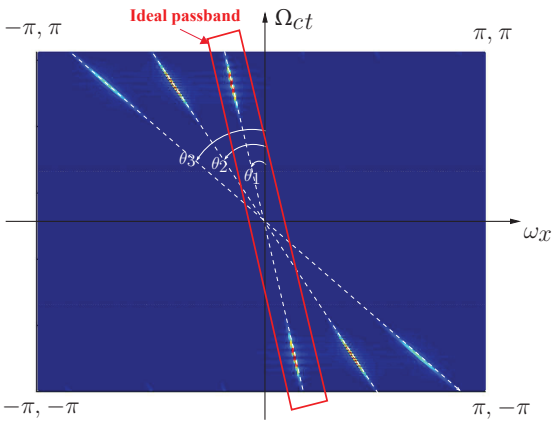

Figure 2.5: 2D mixed-domain (ω_x, Ω_{ct}) frequency spectrum of three broadband Gaussian-modulated cosine pulses.

wideband space-time filter). Figure 2.5 shows the spectrum of three Gaussian cosine modulated signals illuminating a ULA at angles θ_1, θ_2 and θ_3 respectively. If we desire to enhance one PW while filtering out the others, we essentially need a filter with the ideal passband as shown with a red box. Beamforming at such frequencies is known as *RF beamforming*. However, digital beamforming will need the RF signal to be downconverted and downsampled due to limitations of the data convertors on the digital platform. The next paragraph discusses the spectral properties of downconverted and downsampled STPWs.

Fig. 2.6 shows an illustration of the 2D spectral transformation of a 2D broadband bandpass STPW from RF to baseband. Fig. 2.6(a) shows the spectrum of an RF signal with temporal frequency f_c possessing a double-sided bandwidth of 2B and is arriving at a ULA at an angle of ψ, remember that $\sin\psi = \tan\theta$. If there is certain uncertainty in predicting the spatial DoA ψ, say ϵ, then the 2D straight-line RoS of the STPW occupies a trapezoidal region as shown in Fig. 2.6(a), where $\Delta\theta$ is the variation in spatio-temporal DoA θ due to uncertainity in the spatial DoA ψ. The trapezoidal RoS plot of the temporally in-phase (I) quadrature (Q) down-

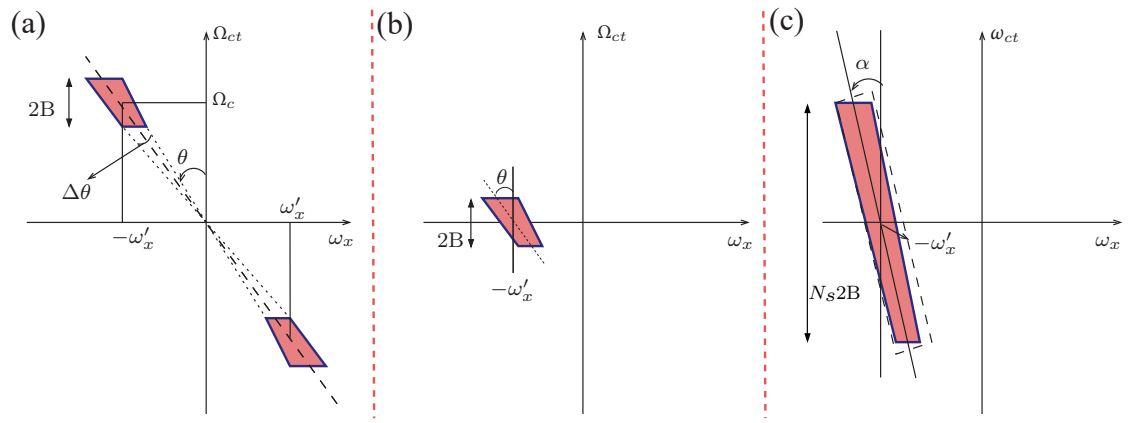

Figure 2.6: (a) RoS of the ST broadband bandpass PWs received by a ULA (b) RoS of the ST broadband bandpass PWs following I-Q downconversion. (c) RoS of the ST broadband bandpass PW following I-Q downconversion and downsampling.

converted signal is shown in Fig. 2.6(b), which corresponds to the Fourier shifting property shown in Eq. (2.10),

$$s(x,ct) \xrightarrow{\mathcal{F}} S(\omega_x,\Omega_{ct}) \quad \Rightarrow \quad s(x,ct)e^{-j\Omega_c ct} \xrightarrow{\mathcal{F}} S(\omega_x,\Omega_{ct}+\Omega_c) \tag{2.10}$$

The temporal down-conversion stage brings the temporal frequency content to the base-band without affecting the spatial frequency ω_x, where $\omega_{ct} = \Omega_{ct}\Delta T_s$. Due to this effect, RoS of the produced signal is spatially shifted by ω'_x, where $\omega'_x = \pm\left(\pi\frac{f_c}{f_c+B}\sin\theta\right)$ [47]. Now the signal is at baseband, and and analog-to-digital conversion (ADC) sampling by a frequency $f_s = 1/\Delta T_s$ down-samples the signal by a factor of $N_s \in \mathbb{Z}$ and causes the spatio-temporal DoA to change to angle α [43] given by Eq. (2.11) and as shown in Fig. 2.6 (c),

$$\alpha = \tan^{-1}\left(\frac{\Delta x}{N_s c\Delta T_s}\sin\psi\right). \tag{2.11}$$

ADC sampling transforms the analog temporal domain Ω_{ct} to ω_{ct}, where $\omega_{ct} = \Delta T_s\Omega_{ct}$. Thus the filter in digital domain should encompass a trapezoidal passband

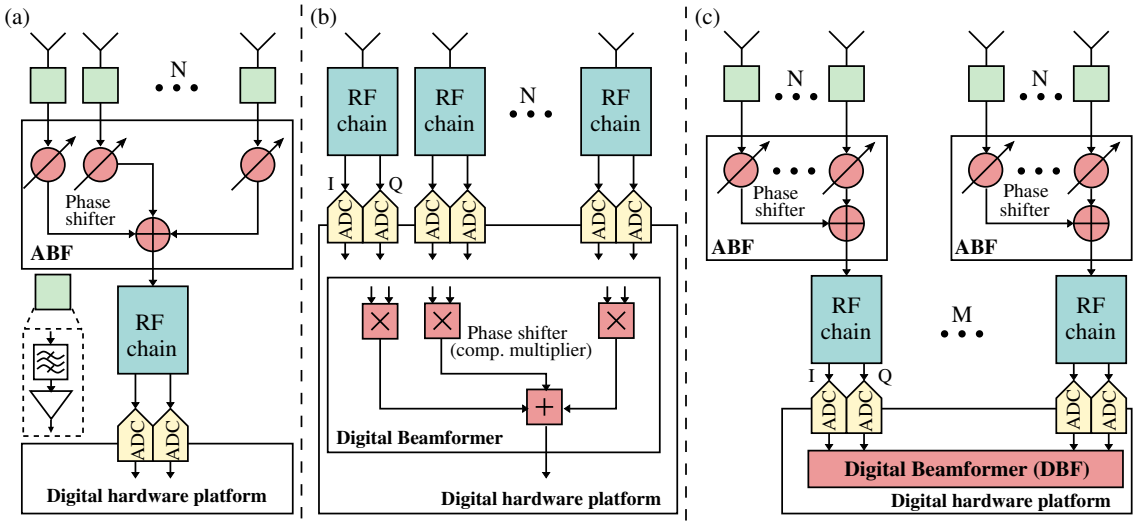

Figure 2.7: Beamforming architectures: 1) Analog beamforming, 2) Digital beamforming, 3) Hybrid beamforming.

that encloses the region $\omega_x = \omega'_x$ and is aligned at α to the ω_{ct} axis, in order to beamfilter the plane-waves that are arriving at an ULA with an angle ψ [43, 48]. Next section describes about such filter architectures.

2.5 Beamforming or spatial filtering techniques

This section provides an overview of beamforming techniques and their architectures. Beamformers are categorized based on the hardware implementations, bandwidth requirements, pattern synthesis techniques, and the type of beam required (fixed or adaptive). Based on these features, the beamforming is accomplished by using three main approaches: analog beamforming, digital beamforming, and hybrid beamforming; their architectures are shown in Fig. 2.7 (a). Analog beamforming implements the spatial filtering operation by employing analog electronics either in RF/IF stages of a phased array. Phase-shift–based analog beamfilters as shown in Fig. 2.7 (a), are widely used among all the analog approaches. Digital beamforming

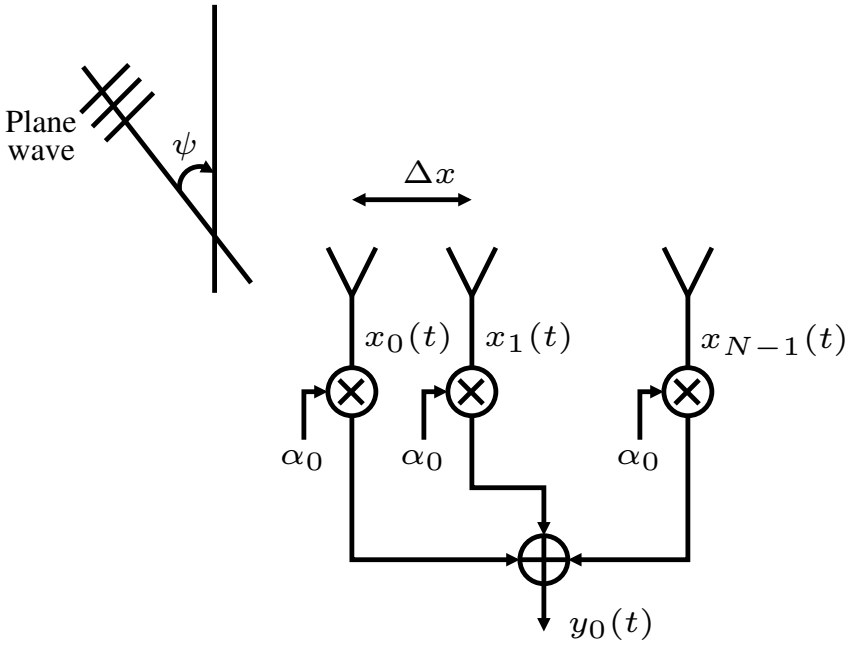

Figure 2.8: Receive mode model of an N-element phased array.

provides maximum flexibility, reconfigurability, and maximum degree of freedom for beam combinations over traditional analog phased-array implementations. An example architecture for a digital beamforming implementation is shown in Fig. 2.7(b). However, digital beamforming requires one RF chain and two ADCs per antenna element assuming I-Q downconversion. This results in high power consumption because of the power-hungry ADCs, especially when larger arrays are implemented with high bandwidths. To get the best from both worlds, a hybrid beamforming approach is developed that is shown in Fig. 2.7(c). It combines the analog beamformers having the lowest power consumption with low-dimensional digital beamformers. This approach typically uses RF phase-shifters, true-time-delays (TTDs), or lenses for level-1 analog beamforming and digital filters/algorithms for level-2 beamforming. In simple terms, all these beamformers can be treated as a circuit with multipliers/weights applied to the incoming signal from the antenna array.

2.5.1 Beamforming implementation with fixed weight set

Consider an N-element ULA with elements spaced at $\Delta x = \lambda_{min}/2$ satisfying the Nyquist spatial sampling as shown in Fig. 2.8. A 2D STPW is arriving at the ULA with an angle ψ and the time-continuous signal received by the array is $\mathbf{x}$, which is given in the equation below:

$$\mathbf{x} = [x_0(t)\ x_1(t)\ \ldots\ x_{N-1}(t)]^{\mathbb{T}}, \tag{2.12}$$

where $x_{n_x}(t)$ is the signal at n_x th spatial location. The signal received from each n_x antenna element is subjected to a specific weight α_{n_x} that is essential to the formation of beams. If the weighting vector $\mathbf{w}$ is given as in Eq. (2.13),

$$\mathbf{w} = [\alpha_0\ \alpha_1\ \ldots\ \alpha_{N-1}]^{\mathbb{T}}, \tag{2.13}$$

then the beamformed time domain output y is given by Eq. (2.14),

$$\mathbf{y} = \mathbf{w}^{\mathbb{T}}\mathbf{x}. \tag{2.14}$$

The beam pattern corresponding to the weight vector $\mathbf{w}$ is related to its DFT [42]. In a narrowband case, these weights are complex constants, to produce a broadband beam, the weights are modified to incorporate the time delay $\tau = \frac{\Delta x \sin\psi}{c}$ rather than just the phase [49], and such an implementation has a weight vector $\mathbf{w}$ that looks like the one shown here:

$$\mathbf{w} = \left[1\ \ e^{-j\Omega_t\tau}\ \ \ldots\ e^{-j\Omega_t(N-1)\tau}\right]^{\mathbb{T}}, \tag{2.15}$$

where $\Omega_t = 2\pi f_t$ is the temporal frequency variable. Since the weights are frequency-dependent that realize a true time delay across the signal bandwidth, such an architecture will produce a wideband squint-free beam. Such implementions are realized in analog using progressive transmission line delays [50], antenna/sensor delay

lines [51] and using analog all-pass filters that realize the required time delays [52]. Wideband implementations in digital domain include both IIR and FIR filter realizations. For IIRs, the filters are designed in such a way that they encompass the trapezoidal pass band of the downconverted, downsampled STPW signal. Several such implementations have already been reported in the literature [53–56]. FIR implementations achieve the true time delay using higher-order FIR or fractional delay filters [43,48,57–60]. Another wideband digital approach is through utilization of FFTs where the wideband signal is decomposed to a set of narrowband outputs, and each output is applied to a specific complex coefficient that realizes the required corresponding phase delay.

2.5.2 Multi-beam beamformers implementation

We have looked at implementations of a single-beam beamformer where the systems are multi-input and single output. However, the maximum beams that can be formed through a phased array is equal to the number of elements in it. Producing multibeams involves realizing more than one complex vector–perhaps a matrix of the vectors that are mentioned in (2.13). Such a matrix is given in Eq. (2.16),

$$\mathbf{W}_p = [\mathbf{w_1}\ \mathbf{w_2}\ \ldots\ \mathbf{w_p}]^{\mathbb{T}} \tag{2.16}$$

where $W_p \in \mathbb{C}^{p\times N}$ is the matrix containing p weighting vectors that is used to realize p beams. From inspection, W_p is a $p \times N$ matrix that takes the form of a Vandermonde matrix [61]. Each beamforming weight vector $\mathbf{w} = \begin{bmatrix}1 & e^{-j\Omega_t\tau_k} & \ldots & e^{-j\Omega_t(N-1)\tau_k}\end{bmatrix}^{\mathbb{T}}$, where $\tau_k = (\Delta x \sin\psi_k)/c$ and $1 \leq k \leq p$, corresponds to a steering weight vector to realize a beam at an angle of ψ_k off broadside. To maximize the degrees of freedom, it is essential that all of the weighting vectors are linearly independent. Choosing $p = N$ will capture all the degrees of freedom from the array.

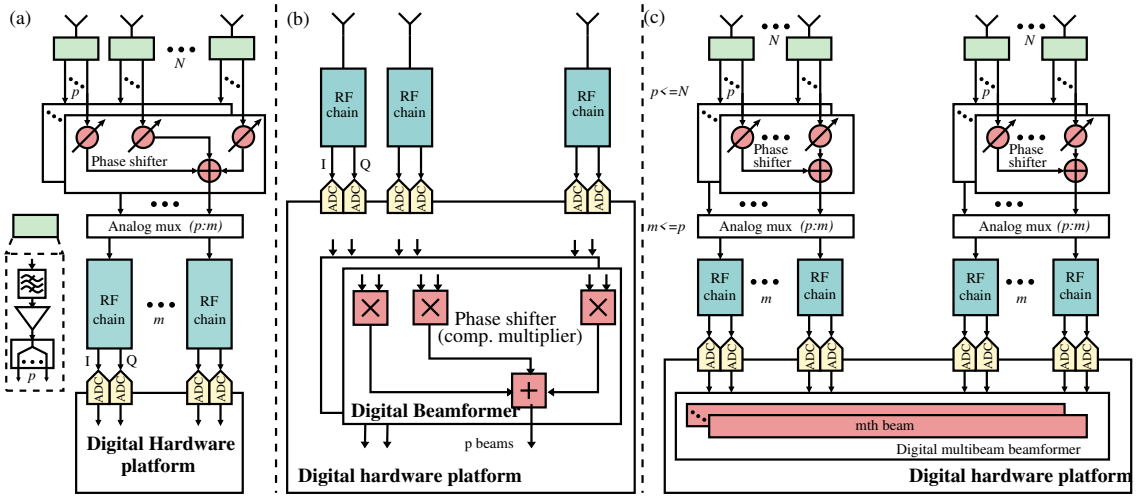

Figure 2.9: Mutibeam beamforming architectures: (a) analog beamforming (b) digital beamforming (c) hybrid beamforming.

Similar to single-beam beamformer approaches, multi-beam beamformers can be categorized into three main approaches: analog multibeam beamforming, digital multibeam beamforming, and hybrid multibeam beamforming. The corresponding architectures for each approach are shown in Fig. 2.9. Realization of multi-beams can be achieved by cascading single-beam realizations to achieve one or more pass-bands. A quite popular way of achieving it is through Fourier transform. A Fourier transform contains an $N \times N$ matrix that contains different weights and is analogous to the weighting matrix as shown in (2.16). Thus, selecting $\mathbf{W}_{p=N}$ to be the N-point DFT matrix produces N RF beams for both transmit and receive multibeam applications. The orthogonal property of the DFT matrix ensures there is no inter-beam interference. The analog-based FFT realizations include implementations based on a Butler matrix and a lens based focal planar array (FPA) [62, 63]. This work contains three multi-beam beamformer implementations that are based on trapezoidal passband IIR filters, FFT algorithms, and lens + FPA structures.

2.6 Conclusion

This chapter presented a review of propagating plane-waves a.k.a spatio-temporal plane-waves (STPW) and their properties relating to the beamforming theory. First, we described the STPWs propagating in 3D space and derived the mathematical function to express those waves in space and time. Continuing the same discussion, this chapter demonstrated the signal processing of the plane waves with different planar antenna configurations. Next, the spectral properties of the STPWs relevant to ULAs were discussed and the spectrum's region of support (ROS) was defined. The trapezoidal passbands of the downconverted, downsampled STPWs signals was demonstrated, and the requirements for digital spatial filters to enhance those signals was investigated. Finally, we discussed different implementation topologies for beamformer implementations. This was extended for multi-beam approaches. The multi-beam beamformers developed in the subsequent chapters of this dissertation will be based on these concepts.

CHAPTER 3

MULTIBEAM ARRAY RECEIVER USING 2D SPATIALLY BANDPASS DIGITAL IIR FILTERS

This chapter provides the background and implementation of multibeam beamformer architectures based on IIR filter topology. These IIR filters employ 2D space-time networks where the network parameters can be tuned to achieve electronical beam steering/filtering. The filters that are proposed in this chapter include the trapezoidal passband required for filtering the 2D ST broadband bandpass PWs; hence they are called 2D spatial bandpass digital IIR filters. First, we will discuss the evolution of such filters from basic circuit theory; next, we will discuss the filter's spectral properties and how the filter will be implemented to achieve beamforming. We will then discuss the realization of a 2.4-GHz 16-element multi-beam digital array receiver that incorporates a 2D spatial bandpass IIR filter in the DSP back-end. The proposed work is verified for a two-beam case. This work, which was done in collaboration with Dr. Chamira Edussooriya of the University of Moratuwa, has resulted in one publication [64].

3.1 Background

In Chapter 2, we discussed the spectral properties of the 2D ST broadband PWs and the requirements for spatial filters to enhance the desired PWs coming from a specific DoA while filtering out the rest. The spectral properties and RoS for a 2D STPWs at various stages in an RF signal processing chain are shown in Fig. 3.1. In this work, we explore multi-dimensional signal processing algorithms that operate on an array of digital receivers to perform the beamforming. The proposed system uses 2D linear space-time invariant frequency plane-wave (FPW) filters possessing

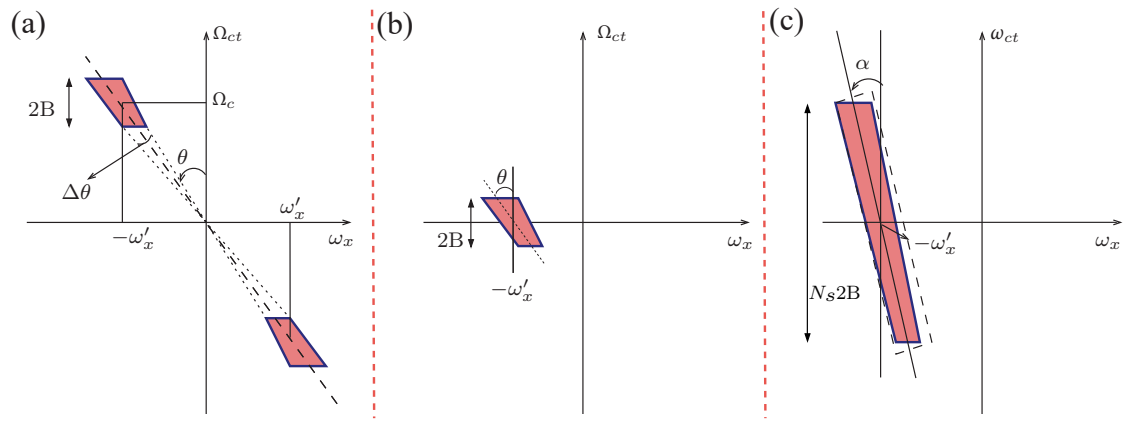

Figure 3.1: (a) RoS of the ST broadband bandpass PWs received by a ULA; (b) RoS of the ST broadband bandpass PWs following I-Q downconversion; (c) RoS of the ST broadband bandpass PW following I-Q downconversion and downsampling.

trapezoidal passbands and with an infinite impulse response (IIR). These filters have been proposed in [53–55] and they have been proven to be stable 2D filters [56, 65]. Although 2D finite impulse response (FIR) filter–based algorithms have desirable properties, such as unconditional filter stability and linear-phase response when required, they have greater DSP computational complexity as compared to 2D IIR filters of similar beam selectivity. Therefore, the 2D IIR filter implementations proposed are preferable for achieving designs with low sizes, weights, power, and costs. This work reports the experimental verification of the use of such multi-dimensional filters for the first time. Trapezoidal 2D spatial bandpass IIR filters are derived from frequency planar filters. Thus, in the next paragraph, we cover the evolution of frequency planar filters.

Two-dimensional IIR frequency planar filters are wideband array processing algorithms that were derived based on the concept of multi-dimensional space-time network resonance [44]. These space-time networks networks were first described by Bruton and Bartley in 1985, and they take the form shown in Fig. 3.2(a). They

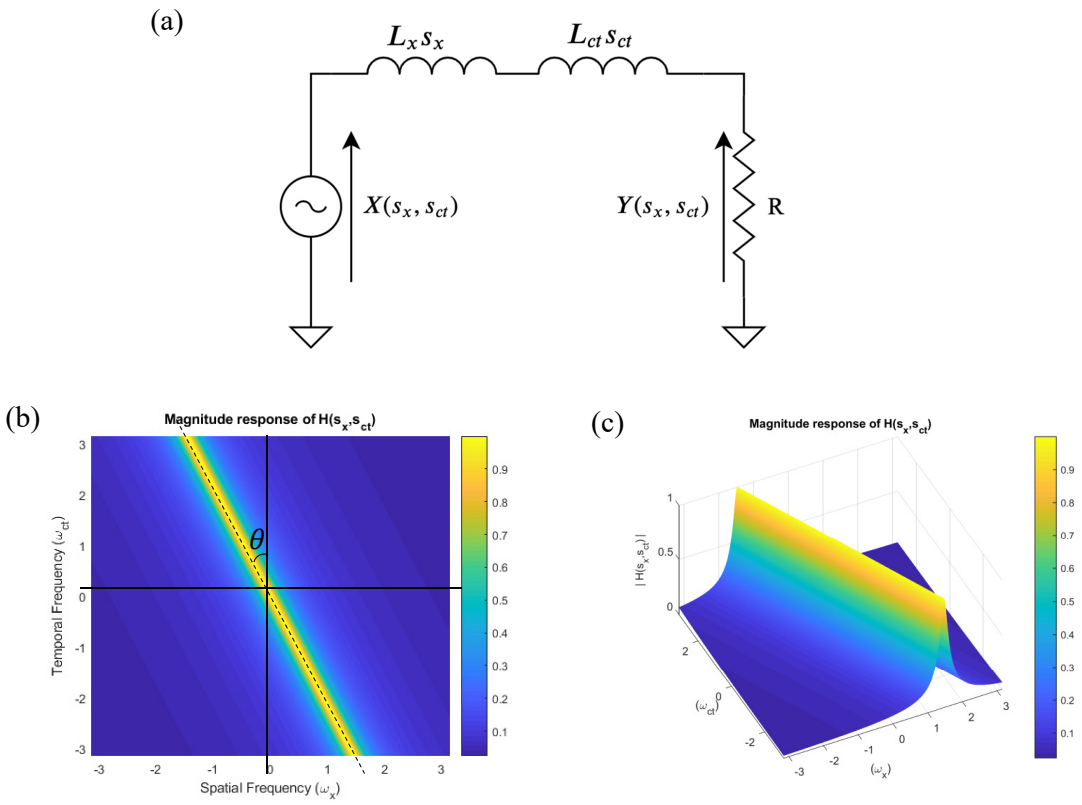

Figure 3.2: (a) A 2D resistively terminated passive prototype network with spatial inductor L_x and temporal inductor L_{ct}; (b) A 2D magnitude response of filter $H(s_x, s_{ct})$, and (c) A 3D view of the frequency response in (b).

are resistively terminated passive networks that achieve filtering using the concept of network resonance [44, 45, 66].

In the prototype networks shown in Fig. 3.2(a), $X(s_x, s_{ct})$ is the input Laplace transform, $Y(s_x, s_{ct})$ is the output Laplace transform, $s_x \in \mathbb{C}$ is the spatial Laplace operator, $s_{ct} \in \mathbb{C}$ is the temporal Laplace operator and $\{L_x, L_{ct}, R\} \geq 0$ are the parameters that define the filter performance. The prototype transfer function in the Laplace domain is given in Eq. (3.1) [44],

$$H(s_x, s_{ct}) = \frac{Y(s_x, s_{ct})}{X(s_x, s_{ct})} = \frac{R}{R + L_x s_x + L_{ct} s_{ct}}, \tag{3.1}$$

The 2D frequency response transfer function (TF) is found by setting the spatial frequency variable s_x to $j\omega_x$ and setting the temporal frequency variable s_{ct} to

$j\omega_{ct}$and as given by Bruton and Bartley [44]:

$$H(j\omega_x, j\omega_{ct}) = \frac{R}{R + j(L_x\omega_x + L_{ct}\omega_{ct})}, \quad \{L_x, L_{ct}\} \geq 0 \tag{3.2}$$

From filter theory, it can be said that this passive prototype network resonates when $L_x\omega_x + L_{ct}\omega_{ct} = 0$. To suit our needs, such a network can be transformed to a 2D IIR frequency planar beam filter by choosing $L_x = \cos\theta$ and $L_{ct} = \sin\theta$ [53, 55]. Hence, this causes the passband of the filter to be aligned to an angle θ to ω_{ct} axis as shown in Fig. 3.2. We recall that θ is the ST DoA of the PW signal.

The prototype transfer function is then converted to a discrete domain by applying the normalized 2D bilinear transform given by $s_k = (1 - z_k^{-1})$, $k \in \{x, ct\}$ to obtain $H(z_x, z_{ct})$ as shown in Eq. (3.3), where the denominator coefficients can be expressed in closed form in terms of the network parameters as $b'_{ij} = \frac{R+(-1)^i L_x+(-1)^j L_{ct}}{R+L_x+L_{ct}}$ with $i + j \neq 0$. The 2D z-domain TF can be mapped into a 2D discrete domain difference equation to achieve real-time implementation [53, 67, 68].

$$H(z_x, z_{ct}) = \frac{1 + z_x^{-1} + z_{ct}^{-1} + z_x^{-1}z_{ct}^{-1}}{1 + b'_{10}z_x^{-1} + b'_{01}z_{ct}^{-1} + b'_{11}z_x^{-1}z_{ct}^{-1}} \tag{3.3}$$

We have shown how 2D frequency planar filters can be utilized to enhance plane waves arriving at a ULA with an angle θ as shown in Fig. 3.1(a). However, these filters perform the beamforming directly at RF frequencies; in contrast, we need to selectively enhance the plane waves following downconversion and downsampling, as shown in Fig. 3.1 (c), and those filters are called 2D IIR SBP beam filters. In the next section, we look into the evolution of the 2D IIR SBP beam filters from 2D IIR frequency planar filters.

3.2 Evolution of first-order 2D IIR SBP beam filters

The 2D IIR SBP beam filters are required to contain a frequency response that encompass the trapezoidal passband of the downconverted and downsampled STPWs that is centered at $\omega_x = \omega'_x$. Thus, if we can center the passband of the frequency planar wave (FPW) filters on spatial frequency ω'_x rather than the origin, we can process the desired STPWs. Therefore, the TF of the 2D IIR SBP beam filter can be obtained by applying spatial modulation to the the impulse response of (3.3) i.e., multiplying the impulse response of the FPW filter by the factor $e^{(j\omega'_x n_x)}$, where n_x is the spatial index.

Consider $h_{FP}(n_x, n_{ct})$ to be the impulse response of the 2D IIR frequency planar filter with a transfer function $H_{FP}(z_x, z_{ct})$ given by (3.4) [53, 54],

$$H_{FP}(z_x, z_{ct}) = \frac{(1 + z_x^{-1})(1 + z_{ct}^{-1})}{1 + b'_{10} z_x^{-1} + b'_{01} z_{ct}^{-1} + b'_{11} z_x^{-1} z_{ct}^{-1}}, \tag{3.4}$$

then the impulse response of the first-order 2D IIR SBP beam filter is obtained as shown in (3.5) [64, 69],

$$h_{IIR}(n_x, n_{ct}) = e^{j\omega'_x n_x} h_{FP}(n_x, n_{ct}), \tag{3.5}$$

where $H_{IIR}(z_x, z_{ct}) \overset{2D}{\Leftrightarrow} h_{IIR}(n_x, n_{ct})$ is the transfer function of the proposed beam filter. Using the scaling property of the z-transforms [70],

$$a^{n_1} h_{FP}(n_1, n_2) \overset{2D}{\Leftrightarrow} H_{FP}(z_1/a, z_2), \quad |a| \leq 1$$

we obtain the normalized transfer function of the 2D IIR SBP beam filter as given in (3.6) [64, 69],

$$H_{IIR}(z_x, z_{ct}) = \frac{(1 + e^{-j\omega'_x} z_x^{-1})(1 + z_{ct}^{-1})}{1 + b'_{10} e^{-j\omega'_x} z_x^{-1} + b'_{01} z_{ct}^{-1} + b'_{11} e^{-j\omega'_x} z_x^{-1} z_{ct}^{-1}}, \tag{3.6}$$

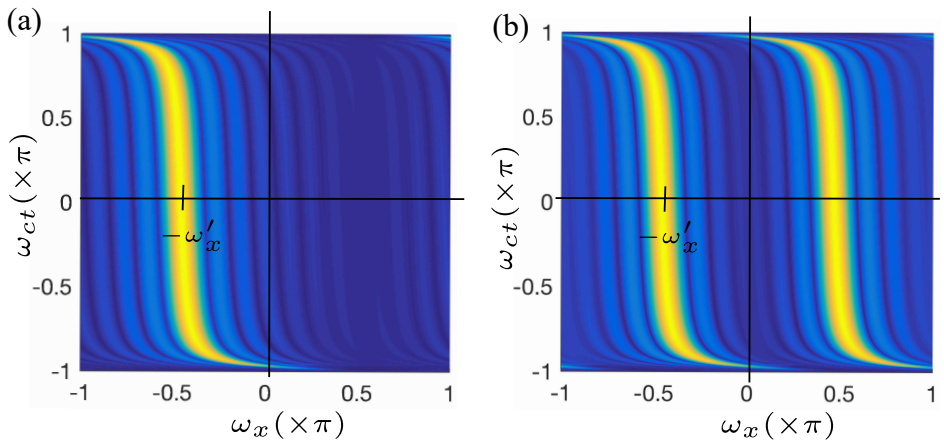

Figure 3.3: Magnitude response of (a) first-order and (b) second-order 2D IIR SBP filter for $\theta = -30°$.

where the coefficients b'_{ij} are defined in (3.7) and are expressed in terms of the ST angle α as follows

$$b'_{ij} \;=\; \frac{R + (-1)^i L_x + (-1)^j L_{ct}}{R + L_x + L_{ct}}, \tag{3.7}$$

for $i, j = 0, 1$, $i + j \neq 0$, and $R > 0$ sets the selectivity of the filter pass band. Here $L_x = \cos\alpha$ and $L_{ct} = \sin\alpha$ (normalized to $\Delta x = c\Delta T_s = 1$), where $0 \leq \alpha \leq \pi/2$ [54, 66]. Thus, the beamwidth ad directivity of the beam can be controlled by changing the value of R. The magnitude frequency response plot for the 2D IIR filter TF given by (3.6) for $\theta = -30°$, $f_t = 2.4$ GHz, and $B_t = 200$ MHz is shown in Fig. 3.3 (a). The filter has a magnitude response that accompanies a beam having a trapezoidal passband shifted on spatial spectral axis. It should be noted that the proposed IIR filter is practical bounded-input-bounded-output (P-BIBO) [66] in only one quadrant (only for negative angles of arrival). The filter can be tuned to positive beam directions by flipping the signs of the antenna inputs to the filter so that the spectrum is mirrored on the ω_{ct} axis.

The 2D IIR SBP beam filter given in (3.6) is a first-order filter, but a second-order version of the filter is proposed in [54] in which the the spatial modulation

is accomplished by multiplying with a factor $\cos(\omega'_x)$ to the impulse response of FPW filter. The magnitude frequency response plot for the second-order 2D IIR SBP filter for the similar parameters considered above is shown in Fig. 3.3 (b). It contains double-sided trapezoidal passbands and such a filter response is suboptimal if we perform a complex I-Q downconversion in which the beam-shaped passband corresponding to a 2D PW occupies only the negative ω_x axis because the extra band that is not occupied by the signal itself still passes noise and interference. Therefore, the first-order single-band version provides a beam in the direction of the RF signal without spurious responses in undesired directions. Moreover, the first-order filter is less complex from a digital arithmetic standpoint (although it requires complex-valued DSP due to its single-band nature).

3.2.1 Architecture and implementation of the 2D IIR SBP filter

If the 2D discrete input and 2D discrete output for the proposed filter are given by $pw_{2\mathrm{D}}(n_x, n_{ct}) \overset{2D}{\Longleftrightarrow} PW_{2\mathrm{D}}(z_x, z_{ct})$ and $y(n_x, n_{ct}) \overset{2D}{\Longleftrightarrow} Y(z_x, z_{ct})$, respectively, its transfer function can be expressed as $H_{IIR}(z_x, z_{ct}) = Y(z_x, z_{ct})/W(z_x, z_{ct})$. Computing the inverse 2D Z-transform of (3.6) under zero initial conditions, the 2D difference equation that can be implemented in digital hardware is obtained. The simplified difference equation of the first-order single-band 2D IIR SBP filter is given by (3.8) [64, 67, 69],

$$\begin{aligned} y(n_x, n_{ct}) = {} & [pw_{2\mathrm{D}}(n_x, n_{ct}) + pw_{2\mathrm{D}}(n_x, n_{ct}-1)] - b'_{01}y(n_x, n_{ct}-1) \\ & + e^{-j\omega'_x}\big[\,[pw_{2\mathrm{D}}(n_x-1, n_{ct}) + pw_{2\mathrm{D}}(n_x-1, n_{ct}-1)] \\ & \quad - [b'_{10}y(n_x-1, n_{ct}) + b'_{11}y(n_x-1, n_{ct}-1)]\,\big]. \end{aligned} \tag{3.8}$$

The direct-form-I implementation of the above difference equation yields a novel parallel processing core module (PPCM) block shown in Fig. 3.4(a), where several such blocks are systollically inter-connected to yield the proposed first-order SBP beam filter for the required number of spatial inputs. The digital architecture for implementing the filter is shown in Fig. 3.4(b). This direct-form-I implementation of the proposed filter requires only one complex multiplier and six real multipliers per antenna element (PPCM), where each complex multiplier is implemented using a Gaussian complex multiplication algorithm that requires only three real multiplications. In contrast, the direct-form-I implementation of the second-order filter requires 13 real multipliers per an antenna element (PPCM); thus, by implementing a complex first-order filter, we are able to reduce the silicon real estate by a margin of four multipliers per element. We have looked into the SBP filters that provide single beam enchancements, however the contents of this work require multi-beam architectures. In the next section, we discuss on how we build multi-beam / multi-band 2D IIR SBP beam filters.

3.2.2 First-order 2D IIR SBP multiband trapezoidal filter

The proposed 2D IIR SBP multiband filters having K multiple trapezoidal passbands (hence, K beams) are designed by combining K 2D IIR SBP filters having single trapezoidal passbands. Multibeam apertures are realized via corresponding multiband digital filters in the DSP system. Each passband of a particular multiband filter generates a far-field beam on the array. The filter-bank structure for the proposed 2D IIR SBP multiband filters is shown in Fig. 3.5, and their corresponding

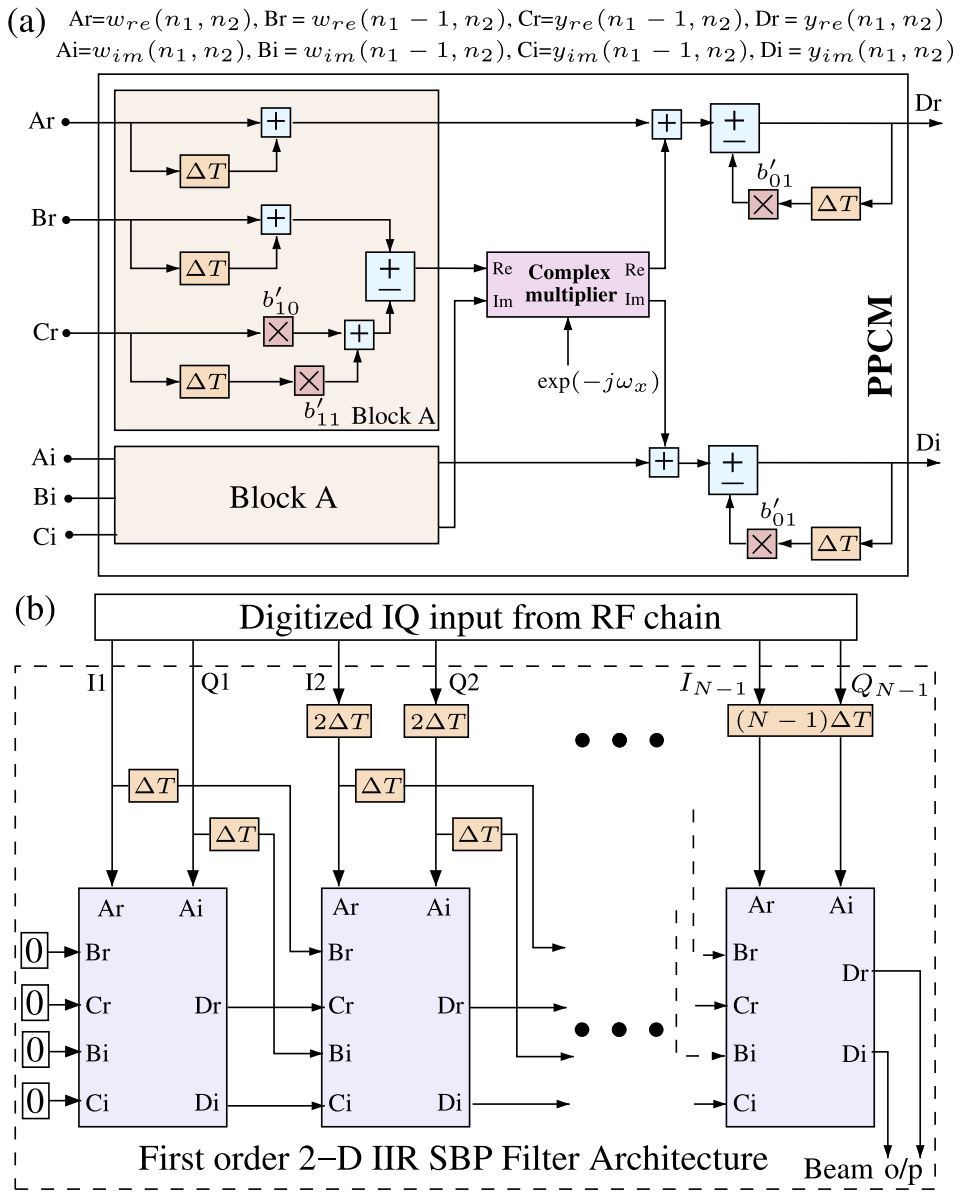

Figure 3.4: (a) Direct-form I implementation of the first-order single-band 2D IIR SBP beam filter. (b) Systolic array architecture of the proposed IIR filter accepting digitized I-Q inputs from the array receiver.

transfer function $H_{IIR,multi}(z_x, z_{ct})$, is given by (3.9),

$$H_{IIR,multi}(z_x, z_{ct}) = \sum_{k=1}^{K} \gamma_k H_{IIR}^k(z_x, z_{ct}), \tag{3.9}$$

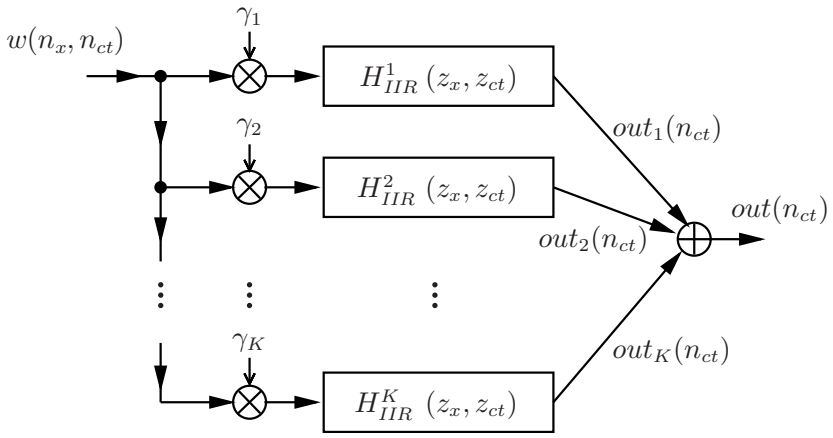

Figure 3.5: Structure for the filter-bank of a 2D SBP multiband trapezoidal filter.

where γ_k, $k = 1, 2, \ldots, K$ are complex-valued constants and $H^k_{IIR}(z_x, z_{ct})$ is the kth 2D IIR SBP filter having a single trapezoidal passband. Note that complex constant γ_k determines the relative contribution to the array pattern by $H^k_{IIR}(z_x, z_{ct})$ corresponding to the kth beam. The special case, $\gamma_k = 1$, $k = 1, 2, \ldots, K$, corresponds to a 2D IIR K-beam filter, in which all the K beams have equal contribution to the array pattern. The temporal output $out(n_{ct})$ of $H_{IIR}(z_x, z_{ct})$ is obtained as given in Eq. (3.10),

$$out(n_{ct}) = \sum_{k=1}^{K} out_k(n_{ct}), \tag{3.10}$$

where $out_k(n_{ct})$ is the temporal output of $H^k_{IIR}(z_x, z_{ct})$.

The multiband version of the proposed first-order 2D IIR SBP filter is evolved by summing up a parallel collection of several such first-order filters for each 2D PW signal of interest (SOI); thus, the transfer function of the K-band version of the proposed filter, $H_{IIR,multi}$ is given by Eq. (3.11),

$$\begin{aligned} H_{IIR}(z_x, z_{ct}) &= \sum_{k=1}^{K} H^k_{IIR}(z_x, z_{ct}) \\ &= \sum_{k=1}^{K} \frac{(1 + e^{-j\omega'_{kx}} z_x^{-1})(1 + z_{ct}^{-1})}{1 + b'_{k10} e^{-j\omega'_{kx}} z_x^{-1} + b'_{k01} z_{ct}^{-1} + b'_{k11} e^{-j\omega'_{kx}} z_x^{-1} z_{ct}^{-1}}, \end{aligned} \tag{3.11}$$

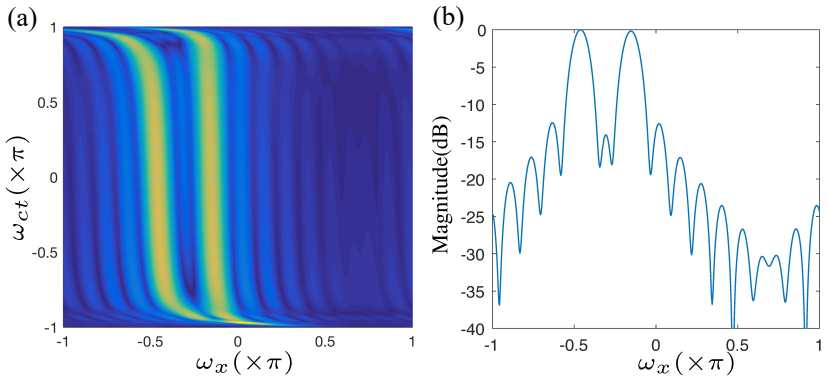

Figure 3.6: (a) Magnitude response of the 2D IIR multiband trapezoidal filter $H_{IIR}(z_x, z_{ct})$; (b) cross section of (a) at $\omega_{ct} = 0$.

where $H^k_{IIR}(z_x, z_{ct})$ is the filter transfer function corresponding to the kth 2D PW SOI, where $\omega'_{kx}, b'_{k01}, b'_{k10}, b'_{k11}$ are the coefficients and spatial shifts corresponding to each individual filter in the filter bank. The outputs from all filters are summed to determine the beam pattern of the multi-beam beam former. The proposed 2D IIR SBP multibeam filter is verified for the case of two broadband bandpass PW SOIs arriving at $\theta_1 = -10°$ and $\theta_2 = -30°$ at a ULA consisting of 16 antennas. Both broadband bandpass SOIs are assumed to have a bandwidth $B_t = 200$ MHz from 2.3 GHz to 2.5 GHz and are quadrature-sampled with a $f_t^C = 2.4$ GHz local oscillator. The inter-antenna distance Δx is 6 cm, and the temporal sampling frequency f_t^S is 240 MHz. The magnitude frequency response plot is shown in Fig. 3.6(a), and the cross section at f_c is shown in Fig. 3.6(b). The two 2D PW are assumed to have different power spectral densities, leading to $\gamma_1 = 1$ and $\gamma_2 = 1.35$. The response consists of two trapezoidal frequency-invariant main lobes, and the PSL is found to be -13 dB.

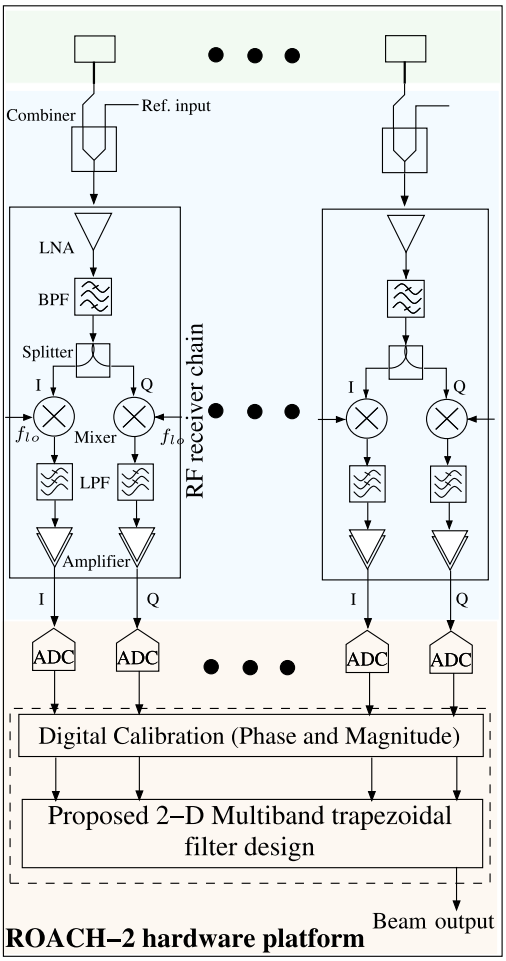

Figure 3.7: Architecture of the test setup for verifying the 2D IIR SBP beam filter.

3.3 Proposed filter validation with a 16-element 2.4-GHz I-Q array receiver

This section describes a 16-element array receiver that is designed and built for real-time verification of the beam patterns arising from the proposed 2D IIR filter designs. The overall system architecture of the test setup is shown in Fig. 3.7. The RF receiver employs a 16-element super heterodyne architecture producing 16 I-Q IF outputs to be sampled by ROACH-2 ADCs. The next section describes the details of the antennas, the receiver chains and the digital back-end.

3.3.1 Antenna array, RF front-end, and digital systems setup

Fig. 3.8(a) shows the practical experimental setup that is used to implement the system architecture in Fig. 3.7. The antenna array consists of 16 rectangular patch antennas operating at 2.4 GHz, and the RF front-end employs a 16-element single-mixer super-heterodyne architecture. The RF front-end shown in Fig. 3.8(b) is implemented using commercial-off-the-shelf components from *MiniCircuits* (combiner - *ZN2PD 63S+*, bandpass filter - *VBFZ 2340S+*, low-noise amplifier - *ZX60-242LN*, mixer - *ZFM-15S+*, lowpass filter -*SLF-550+*, intermediate frequency amplifier - *ZFL-1000LN+*). We employ power combiners prior to the first stage of low noise amplifiers (LNAs) processing, which helps calibrate each RF chain by sending a reference signal. The signal in each chain is then band-pass-filtered, amplified, and received by an I-Q mixing network. The local oscillator (LO) signals are distributed to the 32 identical mixers using a microwave 1:16 splitter. Each of the outputs of the LO distribution system is split to 0°–90° for the I-Q direct-conversion mixers using hybrids. The I-Q downconverted outputs from 16 channels are then low-pass–filtered, amplified, and provided for sampling to the digital platform. The 2D IIR first-order multi-band beamformer is implemented on the ROACH-2–based FPGA system shown in Fig. 3.8(c). ROACH-2–based FPGA system is a standard high-performance FPGA signal processing platform used in the radio astronomy community [71]. The digital conversion of the baseband analog signals from the receiver chains is achieved by using "ADC16x250-8 coax rev-2 daughter cards" [72]. Each daughter card is connected to two ZDOK+ interfaces available in the ROACH-2 platform, via which the sampled data is sent to the ROACH-2's Virtex-6 FPGA over high-speed serializer/deserializer links. This receiver provides a gain of 40 dB and a noise figure of 4 dB. Comprehensive details of the antenna array, RF front-end, and ROACH-2–based FPGA system can be found in [73].

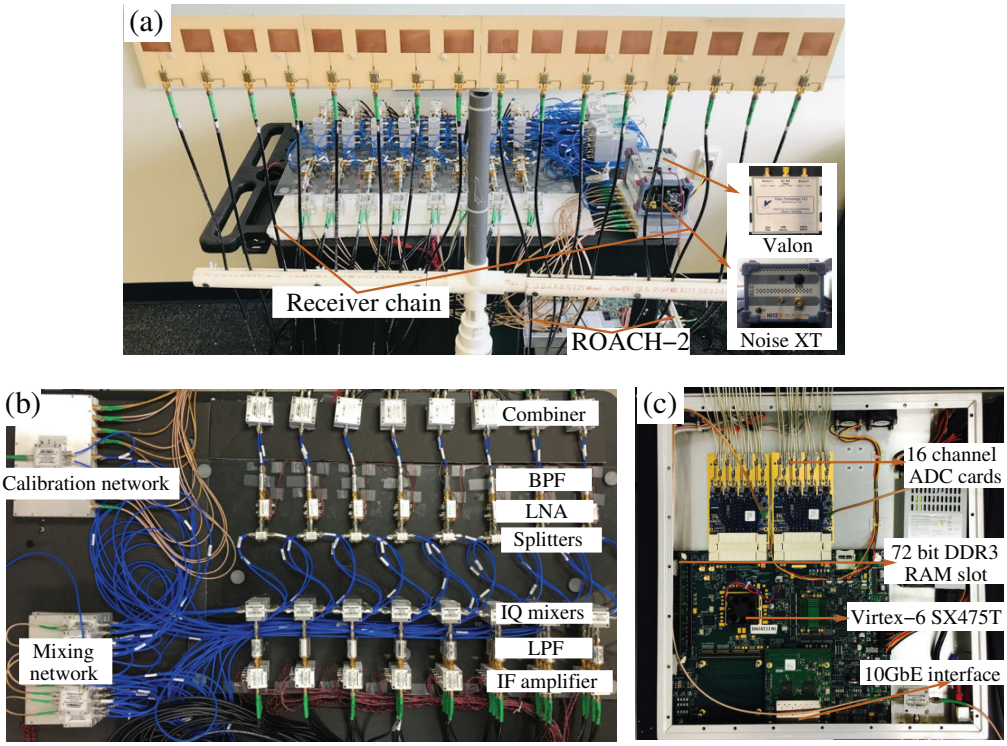

Figure 3.8: (a) The overall experimental setup; (b) RF receiver chain implemented using commercial-off-the-shelf components; (c) ROACH-2 FPGA–based digital back-end.

It is essential that all RF signal generators are synchronized to the same reference clock to avoid frequency drifts. In our case, a 10-MHz reference from the NOISE XT signal generator is used to drive the VALON at receiver side for clocking ROACH-2 analog-to-digital converters (ADCs). NOISE XT generates frequencies from 2 MHz to 7 GHz with a resolution of 1 Hz and ultra-low noise floor down to -178 dBc/Hz. The VALON is a dual frequency synthesizer module whose frequency range spans from 23 MHz to 6 GHz, and it provides 32 dB of attenuation control.

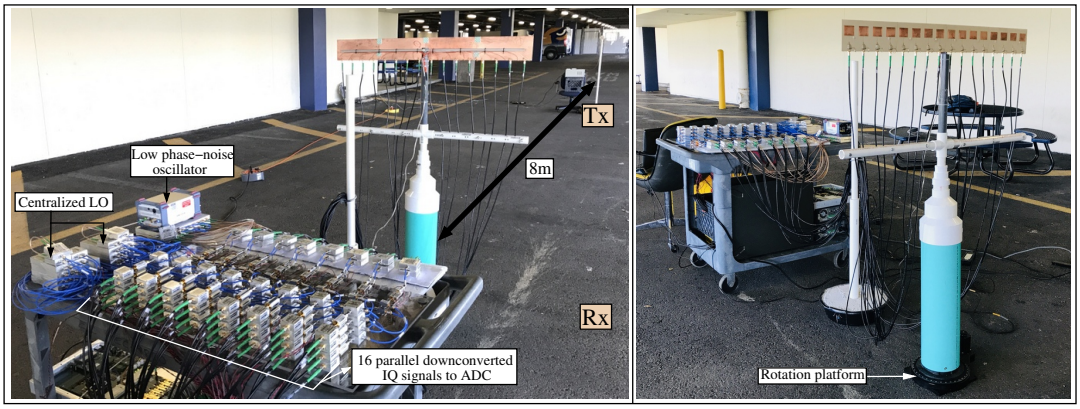

Figure 3.9: Measuring the filter beam patterns from the RF receiver setup placed inside a parking garage.

3.3.2 Measurement setup and limitations

The simulated beam responses assume that the source and transmitter are in the far-field zone. Hence, the measurements have to be computed for the similar setup, which is approximately 16 m for the array under consideration. Such a test setup would require a much larger anechoic chamber than the one that is available to us. Hence, to approximately model the reflection-free anechoic chamber, the measurements are taken in a more spacious environment (a car parking garage), as shown in Fig. 3.9. The designed receiver needs at least -40 dBm of signal power level to reasonably occupy the full scale range of the ADCs; thus, it limits the separation between the transmit antenna and the array to 8 m in order to transmit < 10 dBm. Other limitations include the difference in the polarization reference planes for the transmit and the array and a measuring environment that is not reflection-free.

3.3.3 Measured beams

To measure the beam patterns of the proposed filters, their digital designs are integrated to the array receiver setup. The array was illuminated with a 2.4-GHz

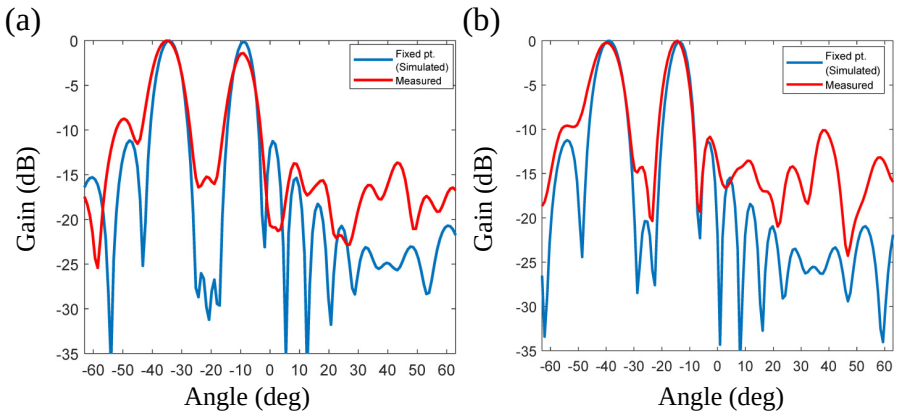

Figure 3.10: Measured beam patterns vs. the fixed-point simulated beam patterns of (a) 2D IIR SBP filter having passbands at $-10°$ and $-35°$; (b) 2D IIR SBP filter having passbands at $-15°$ and $-40°$. The fixed point simulated beams are generated from the digital design from Matlab Simulink and do not incorporate any microwave effects.

sinusoidal carrier and precisely rotated (to keep the transmitter stationary) to obtain a measure of the energy received digitally for each angle of reception. An LO signal of 2.41 GHz was used for downconversion, which corresponded to a signal of 10-MHz at IF. A separate digital circuit was designed and employed for computing the energy received. The effect of channel noise and interference was compensated by periodically switching the transmitter on and off and by using a digital circuit to obtain the difference between the energy accumulated in the two states. Measurement was conducted for a fixed time (10^9 samples) for each angle of reception, and the accumulated signal energy was recorded from $-63°$ to $63°$ with a step size of $0.9°$.

Measurements are performed for two cases. In Case I, coefficients corresponding to the SBP filter having two-beam passbands at $-10°$ and $-35°$ are realized and the beam pattern plot is shown in Fig. 3.10(a). In Case II, the co-efficients are realized, to have two-beam passbands at $-15°$ and $-40°$, and its beam pattern plot is shown in Fig. 3.10(b). The main lobe direction and the peak side-lobe level

(PSL) for both the cases are included in Table 3.1. For both cases, the simulated and measured patterns possessed a maximum absolute error of 0.9° in their beam-directions, whereas the PSL differed by 2.2 dB and 1.7 dB in Case I and Case II respectively.

Table 3.1: Comparison between Simulated and Measured RF Beams

Parameter	Passband (-10,-35) (IIR)		Passband (-15,-40) (IIR)	
	Simulated	Measured	Simulated	Measured
Angle (deg)	(-9,-34.2)	(-9.9,-34.2)	(-14.4,-38.7)	(-14.4,-39.6)
PSL (dB)	-11.1	-8.9	-11.3	-9.6

It can be seen that the measurements are generally in agreement with the theoretical patterns. The mismatches in front-end electronics, deviations in cable lengths, phase noise in clocks and LO signals, interference, and reflections from the test environment leads to the reflected performance degradation of the beamformer. Therefore, the post-calibration errors sets the best case performance of the 2D filter and the overall beamformer.

3.3.4 Contribution and comparison to previous work

The 2D IIR SBP filters proposed in [54,55] are second-order filters that have double-sided trapezoidal passbands. Those filters are sub-optimal since the extra band that is not occupied by the signal itself still passes noise and interference as shown in Fig. 3.3. This work proposes a first-order single-band version which provides a beam in the direction of the RF-signal without spurious responses in undesired directions. In addition, the first-order implementation is less complex from a digital arithmetic standpoint compared to the second-order 2D IIR SBP filter. This work also proposed the multi-beam/multi-band version of the 2D IIR SBP filter to realize more than one beam simultaneously. We reported the experimental verification of

the use of such multi-dimensional filters for the first time. We have discussed and validated a real-time implementation of a 16-element 2.4-GHz 2D IIR SBP filter for two beams. The maximum number of independent beams is limited by the number of antennas in the array; for an N-element array we can realize N-independent RF beams using this approach. It is also possible to have a linear combination of a set of beams to produce a beam in another direction. Considering the relative lower digital complexity of these IIR filters, it is definitely possible to fit more beams into an FPGA when compared to other multi-beam approaches using FFTs, FIRs or true-time delays. A comparison for digital complexity of the proposed beam filters with an FIR implementation is discussed next.

The proposed first-order 2D IIR SBP filter requires nine multipliers per PPCM; thus, for a two-band version of 16-element filter would consume 288 multipliers. An equivalent FIR realization to obtain a similar beam response is found by computing the number of multipliers/coefficients in the impulse response of the IIR filter. The response is obtained for different combinations of angles from two sets ranging from (0° to 90°), and only the filter coefficients whose values are greater than the threshold of (1%) of the normalized response are taken under consideration. Doing so yielded a count of 120 with both I and Q responses combined, and thus is the number of taps required for the FIR for one spatial index. For 16 spatial locations, such a realization would need 1920 multipliers, which is significantly larger compared to the proposed IIR design. The 2D IIR SBP filter implementations are preferable for achieving designs with low sizes, weights, power and costs.

3.4 Conclusion

This chapter presented the design, implementation and the experimental verification of a 2.4-GHz multi-beam array receiver consisting of 16 patch antennas and element-wise fully digital signal processing on a Xilinx FPGA. The IIR SBP PW digital filters having multiple trapezoidal passbands are used to realize multi-beams in real time. These filters are implemented using the ROACH-2 FPGA platform with 32 ADC inputs operating up to 240 MSamples per channel. The measurements are carried out for a two-beam case for two scenarios $(10^\circ, 35^\circ)$ and $(15^\circ, 40^\circ)$. The measured array patterns are in good agreement with the simulated multi-beam patterns, thus validating the proposed 2D IIR multi-beam beamformer. For a two-beam case, the 2D IIR SBP filter saves 81.3% of hardware resources compared to the 2D FIR SBP digital filter implemented on the same FPGA platform.

CHAPTER 4

MULTI-BEAM BEAMFORMING USING FAST FOURIER TRANSFORM

Chapter 2 introduced multi-beam beamforming theory, and we looked at different architectures used to form multi-beams using analog and digital circuits. In this chapter, we discuss multi-beam digital beamforming using fast Fourier transform (FFT) and also realize a four-element receiver array at 28 GHz. The objective of this work is to demonstrate a fully digital multi-beam beamformer at mmW frequencies (27.5–28.3 GHz) with Xilinx RFSoC-based digital back-ends. This frequency range is within the ranges allocated by the Federal Communication Commission (FCC) in the United states for 5G mobile communications. This chapter begins with a brief background on digital multibeam beamforming using fast Fourier transforms (FFT). It continues with a system and link budget analysis of a 28-GHz 32-element receiver array with RF SoC digital back-end, which supports a 64-QAM modulation for 5G orthogonal frequency division multiplexing (OFDM)–based wireless communications. For proof of concept verification, a four-point FFT multi-beam beamforming receiver at 28 GHz is implemented. The antenna array design, receiver array setup and the digital back-end details are presented. A Xilinx ZCU 1275 hardware platform featuring a Xilinx RFSoC device is employed for sampling and to perform the beamforming. This work was done in collaboration with Dr. Elias Alwan at Florida International University and Dr. Ted Rappaport at New York University and with input from my former colleague, Dr. Viduneth Ariyarathna, on the construction of the 28-GHz receiver setup and the realization of the polyphase digital architecture. The research outcomes of this work were disseminated in three publications [33, 74, 75], and the content of this chapter is sourced from these publications.

4.1 Background

As discussed in the Chapter 2, a beamformer is realized by applying a weighting vector W across the spatial samples of a uniform linear array. An N-point DFT matrix contains a set of N complex weights for each antenna element. Thus, selecting $W_{p=n}$ to be the N-point DFT matrix produces N RF beams for both transmit and receive multibeam applications. While the following analysis is conducted on the receiver side, it can be applied to the transmit side due to the reciprocity.

The N-point DFT of a finite duration sequence x_n of length N is defined as,

$$Y_k = \sum_{n=0}^{N-1} x_n e^{-j2\pi kn/N} \; ; k \in [0, N-1], \tag{4.1}$$

where, $Y_k \in \mathbb{C}^{N\times 1}$. Each output Y_k is subjected to a set of weights $e^{-j2\pi kn/N}$ that corresponds to a beam with a peak directivity at $\omega_x = 2\pi k/N$ [76, 77]. Recalling the relation between spatial frequency and temporal frequency $\omega_x/\Delta x = -\Omega_{ct} \sin\psi$ from Chapter 2, solving for beam direction for each output ψ_k for a narrow band system at frequency f_c will produce

$$\psi = \sin^{-1}\left(\frac{kc}{\Delta x f_c N}\right). \tag{4.2}$$

For a ULA with an inter-element spacing $\Delta x = \lambda_c/2 = c/f_c$, the above equation simplifies to

$$\psi = \sin^{-1}\left(\frac{2k}{N}\right) \tag{4.3}$$

Hence, an N-point spatial DFT based approach produces N RF beams with each beam points in a unique direction given by $\sin^{-1}(2k/N)$, where k is the bin number. Fig. 4.1 illustrates the spatial filtering operation performed by DFT algorithms on STPWs. Fig. 4.1 (a) recalls the 2D frequency response of downconverted, down-sampled plane wave and DFT responses in Fig. 4.1(b) approximately realize the

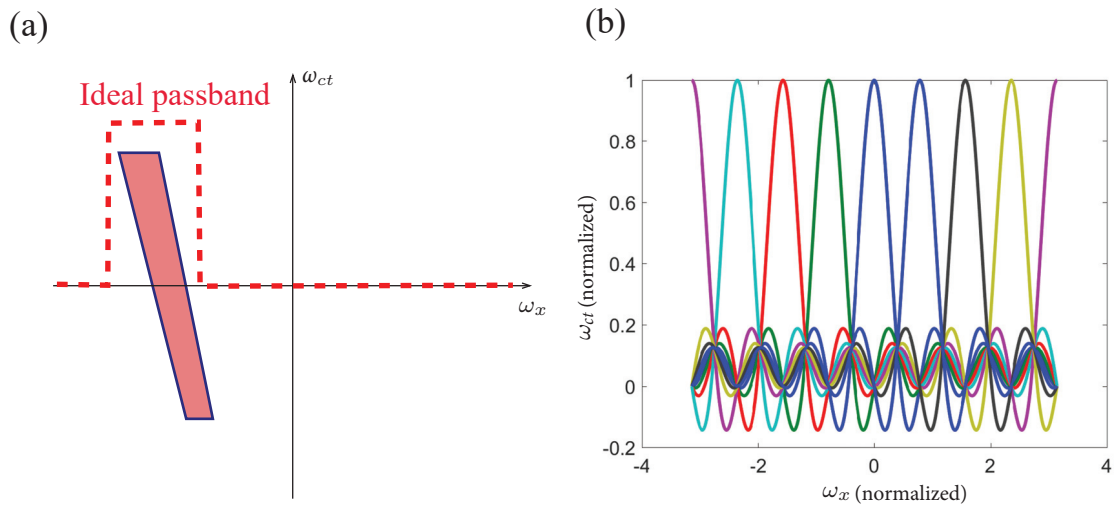

Figure 4.1: (a) 2D frequency response of the I-Q downconverted, downsampled STPW. The red path indicates the ideal passband required by the beamformer, (b) Frequency response of an eight-point DFT filterbank.

filter passbands required for a typical beamformer. The example is shown for N =8, however the filtering resolution increases with higher FFT realizations.

The orthogonality property of the DFT ensures that the main lobe of a given beam falls into the nulls of the other $(N-1)$ beams, in turn, ensuring no inter-beam interference (under the assumption of negligible mutual coupling between elements). The DFT computation at each time step requires an N-point vector of complex valued transceiver signals (i.e., I and Q samples) to be multiplied with the $N \times N$ DFT matrix; thus, direct realizations of the DFT requires digital fixed-point arithmetic circuitry that needs $\mathbb{O}(N^2)$ complex multiplications and parallel additions/subtractions. The DFT computation can be significantly accelerated by using fast algorithms (i.e., FFTs). An FFT factorizes the DFT matrix into a product of sparse matrices, such that the overall multiplicative complexity is reduced. The FFT reduces the digital system complexity (number of multipliers and adders) for an N-point FFT to $\mathbb{O}(Nlog_2N)$. In this work, we employ an FFT based on Cooley–Tukey

FFT factorization [78]. Cooley-Tukey algorithm is the radix-2 decimation-in-time FFT, which splits the N-point DFT computation into two $N/2$-point DFT computations, resulting in an overall reduction in complexity. Recursive use of this algorithm reduces the number of multiplications from $\mathbb{O}(N^2)$ down to $\mathbb{O}(Nlog_2N)$. Thus, formation of N beams in narrowband digital is achieved by employing a digital N-point FFT on each of the complex I and Q signal vector from the array at every time sample. A spatial FFT–based digital multibeam beamformer is discussed in [79], and [80] describes a multibeam digital array for MIMO 5G wireless communications applications. More recent digital multibeam integrated circuits realizations on the same spatial FFT–based multibeam beamforming can be found in [81, 82].

4.2 Development of a 28-GHz 32-element digital receiver array

The proposed work is aimed at designing and developing a 32 element phased array on a 28 GHz receiver to support 64-QAM modulation for 5G OFDM-based wireless communications. The receiver array has been designed to support 845 MHz bandwidth using OFDM that incorporates an FFT size of 512 frequency bins, such that each RF chain establishes a wireless communication link with a bit error probability better than 10^{-5}. Please refer to [83] for details on the theoretical basis for the system design. This section provides the full design schematics of the 28-GHz receivers including the specifications, system design constraints and the RF front-end design.

4.2.1 Design specifications and constraints

The proposed receiver is designed to operate in the frequency range from 27.5 GHz to 28.35 GHz, which is the range allocated for commercial 5G applications in the United States [84]. The OFDM parameters listed below were used for the theoretical calculations: FFT size (N_{FFT}) of 512, modulation (M) of 64 QAM, guard interval (GI) of 1/8, number of data subcarriers of 336, and a subcarrier spacing (CS) of 1.65 MHz. These system parameters provide the required bandwidth (800 MHz) and a maximum data rate of R_b given by the following equation:

$$R_b = \frac{\log_2(M) \times N_D \times \text{CS}}{1 + \text{GI}} = \frac{6 \times 336 \times 1.65 \times 10^6}{1 + 0.125} \simeq 3 \text{ Gbps}. \tag{4.4}$$

To establish a wireless communication link with bit error rate better than 10^{-5} for $M = 64$, E_b/N_0 should be at least 17.8 dB [85]. Hence, the required SNR at the demodulator inputs is given in Eq. (4.5),

$$SNR_{dB} = \left(\frac{E_b}{N_0}\right) + 10\log_{10}\left(\frac{\log_2(M)N_D}{(1 + \text{GI})N_{FFT}}\right) = 23.2 \text{ dB}. \tag{4.5}$$

The receiver chain is designed by taking this SNR value as the design constraint.

4.2.2 Front-end design

A system overview of the proposed front-end design is shown in Fig. 4.2. The front-end design assumes a 16 × 16 beamforming+MIMO architecture that serves as a 5G wireless access point. The performance of a receiver is optimized by designing its electronics to have a low noise figure and high gain. The cascade noise figure of the chain plays a vital role in delivering the required SNR at the digital back-end. The front-end design and the selection of components based on the required SNR are discussed in this section.

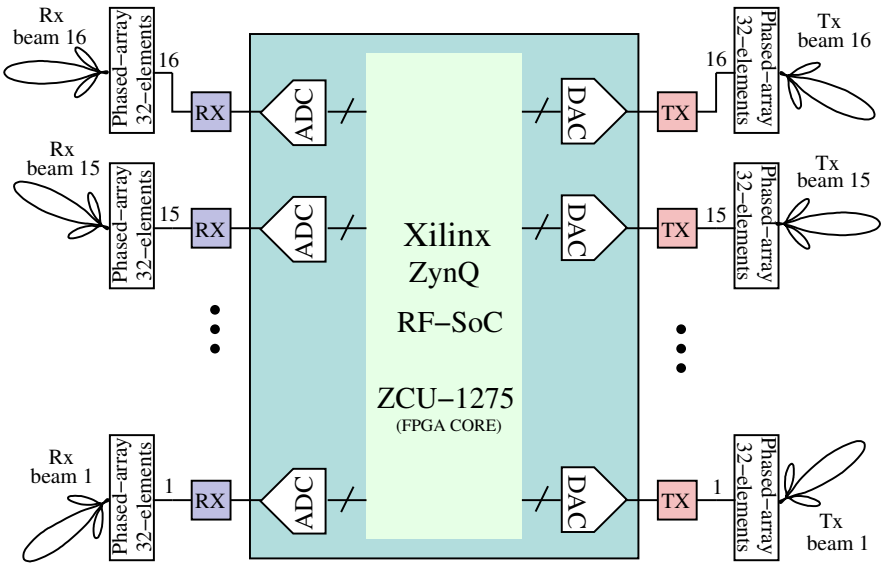

Figure 4.2: System overview: a 16×16 beamforming+MIMO access point for 28-GHz OFDM.

Cascaded noise figure and gain

The analysis for the required noise figure of the receiver chain F_{cas} for a minimum detectable signal P_{in} at its input is as follows,

$$SNR_{out} = SNR_{in,eq} = \frac{P_{in}}{N_{in,eq}}, \tag{4.6}$$

where $N_{in,eq} = kT_0F_{cas}B_n$, $kT_0 = -174\ \frac{dBm}{Hz}$ is the input equivalent noise temperature, and B_n is the noise bandwidth. Converted Equation 4.6 to the log domain and solving for P_{in} (dB) gives the equation in (4.7),

$$\begin{aligned} P_{in,dB} &= SNR_{dB} \ + \ F_{cas,dB} \ - \ 174\ \frac{dBm}{Hz} \ + \ B_n\ dBHz \\ &= 23.2 + \ F_{cas,dB} \ - \ 174\ \frac{dBm}{Hz} \ + \ B_n\ dBHz \end{aligned} \tag{4.7}$$

Since the FCC allocation for 5G 28-GHz band has a bandwidth of 850 MHz, the low-pass filter (LPF) at the end of the RF chain is assumed to have a 3-dB bandwidth of B_n =1000 MHz. Equation ((4.7) is reduced to the following equation:

$$P_{in,dB} = F_{cas,dB} + (-60.8) = \beta. \tag{4.8}$$

The SNR computed above is for a single received path. Hence for an N-element array receiver, the received SNR can be improved by a factor of N. Thus, the input received signal can be as low as $(\beta - 10\log_{10} N)$ for an N-element array by using such a receiver. Hence, if we assume that the signal levels at the input of the antenna are in the range of -85 dBm, for a 32-element array with a gain of 15 dB for each element, the required P_{in} at the receiver chain will be -55 dBm. When substituting this value into Eq. (4.8), a noise figure of $F_{cas,dB} = \mathbf{5.8}$ is obtained for the RF receiver design, which is a tolerable noise figure. The cascaded gain of the chain was calculated based on $P_{in,min,dB}$ computed above, assuming the signals are being sampled by by the ADCs on the Xilinx RF SoC. The full-scale input power for these ADCs are 1 dBm [86]. To operate at 0 dBm (1 dBm below full scale), the cascaded gain $G_{cas,max}$ should be 55 dB. To accommodate the gain, the receiver chain includes an LNA at the beginning and two stages of amplification (IF-VGA amplifiers in cascade) after mixing; this enables the gain to be reduced to fit the IF signal to the ADC full scale for higher input power levels.

Thus, the components for the receiver chain are selected based on the reported noise figure and gain value requirements, which are 5.8 dB and 55 dB, respectively.

Architecture and component selection

A heterodyne I-Q receiver architecture as shown in Fig. 4.3 is employed for our receiver array. The narrow-band nature of patch antennas eliminated the need for separate band-pass filters. A low-side local oscillator is used at the I-Q downconverter (HMC1065LP4E) to generate an intermediate frequency signal of 0.15 to 1 GHz, which is further amplified and sampled by high-speed RF-SoC ADCs. Careful

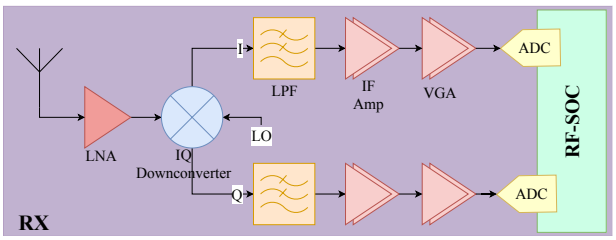

Figure 4.3: Architecture of the single receiver chain of the proposed mmW heterodyne receiver array.

selection of components is critical for providing the desired NF and gain values. Components with higher third-order intercept levels are desirable to provide better linearity and thus higher dynamic range. The final component selections are shown in Table 4.1.

Table 4.1: Components and specifications for the mmW receiver design

Component	**Gain** (dB)	**NF** (dB)	**OIP3** (dBm)
LNA (MAAL-01111)	19	2.5	20
Downconverter (HMC1065LP4E)	9	3	14
Low-pass filter (LPF) (LFCN-900+)	-1	1	N/A
IF amplifier (RAM-8A+)	[31.5,24]	2.6	24.4
VGA (ADL5331)	[-15,15]	9	39

Ideal values of cascaded gain and NF using the selected components are computed using standard formulas [37], resulting in $G_{cas,dB} = 70$ dB and $F_{cas,dB} = 2.5$ dB. For computing the cascaded gain, the maximum gain of the variable gain amplifier (VGA) and the mid-band gain of the IF amplifier are taken into account. The receiver's noise performance is within the NF requirements and, with the help of the VGA, it can provide 30 dB of adjustable gain to increase the dynamic range, which will keep the amplified signal levels within the full-scale range of the ADCs.

4.3 Design of a four-point FFT multi-beam beamforming receiver at 28 GHz

Following the receiver design analysis and component selection, the 32-element 28 GHz receiver array has to be developed. However, due to cost limitations, the experimental setup in this dissertation is limited to only four elements, and a 32-element implementation is reserved for future work. For the proof of concept verification, a four point FFT multi-beam beamformer at 28-GHz is implemented. This 28-GHz four-element receiver array design is a collective effort made by me and my former colleague, Dr. Viduneth Ariyarathna. I have taken the primary responsibility of designing the 28-GHz receiver array starting with the antenna array design and fabrication, component selection of RF-Front ends, and implementation of the four-point FFT design in the RF-SoC FPGA of ZCU1275 board. The individual parts of the antenna array, the RF front-end and FPGA board are integrated to build this four-element, 28-GHz receiver array. Dr. Ariyarathna has contributed towards construction of the 28-GHz setup and fabricating the balun boards needed to interface the analog front-end to the ADCs of the RF-SoCs. He also helped in RF-SoC configuration, ADC calibration, and the building of the polyphase architecture for the FFT digital design; the details of his work can be found in his Ph.D. dissertation [87]. The same setup was also used by Dr. Najath Akram in his Ph.D. research work for validating frequency division multiplexing method at mmWave frequencies [88]. Hence, it must be noted that a overlap of the content and the figures is expected. The following section describes the design and performance of the antenna.

4.3.1 Patch antenna design

For this work, a patch antenna is used due to its advantages, which include but are not limited to low cost, small size, easy to feed, and easy to use in an array. Due to the requirement of high gains at mmW frequencies, we use an eight-element, series fed, vertical sub-array is designed. This sub-array employs a series feeding structure to provide more directive gain in the elevation plane. The geometry of the sub-array to be designed is shown in Fig. 4.4. The vertical sub-array decreases the width of the field patterns in the vertical plane (elevation) so as to suppress interference and spurious signals. Additionally, designing a series fed array with tapered patch widths helps in significantly reducing the side lobe levels (SLLs) of the field patterns along the axis of the array. In series feeding, elements are spaced a guided wavelength apart along a uniform transmission line. By tapering the widths from one edge to the center element in ascending order, excitation is maximum at the center and decreases as it approaches the edge, which results in a slight increase in beam width and a reduction of gain when compared to uniform excitation (i.e., a non-tapered structure). The 28 GHz eight-element subarray is designed with a

Table 4.2: Specifications for the patch antenna

Frequency (f_0)	28 GHz
Substrate	RO4350B
Dielectric constant (ϵ_r)	3.66
Dielectric height (h)	0.254 mm

linear tapering having a -6 dB pedestal that controls the SLL. The patch array is evaluated using a transmission line model [42] in conjunction with wavelength-apart series-fed analysis [89], to compute the dimensions of each patch that produce the corresponding amplitude excitation for the board specifications shown in Table 4.2. The materials were chosen to optimize performance at mmWave frequencies as well

as to account for practical element and transmission line dimensions at these frequencies. The subarray is designed in CST studio suite antenna simulation software. The optimized dimensions for each patch are shown in Table 4.3.

Table 4.3: Dimensions for the Patch Antenna Design

Patches	**1st, 8th**	**2nd, 7th**	**3rd, 6th**	**4th, 5th**
Width (mm)	1.55	2.06	2.59	3.12
Length (mm)	2.81	2.77	2.74	2.72

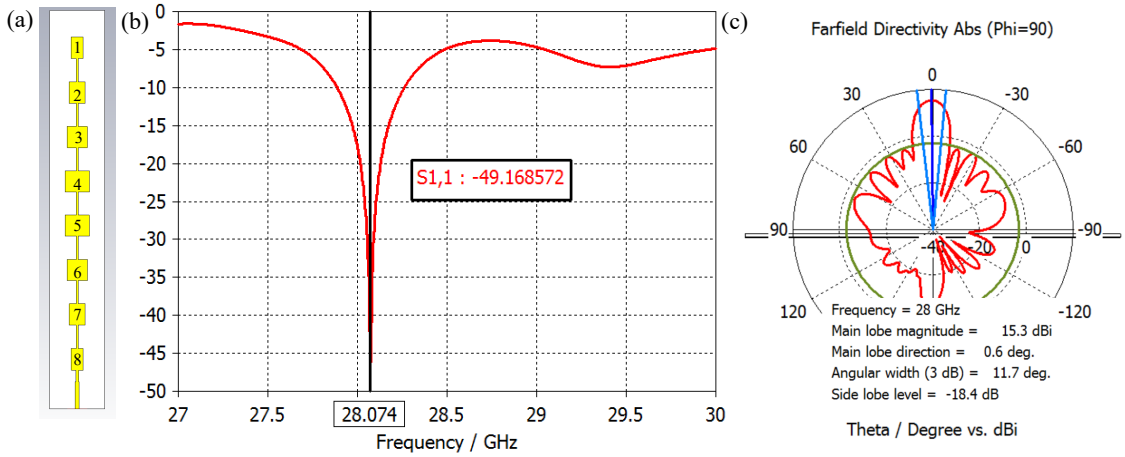

Figure 4.4: (a) Geometry of the designed antenna sub array (b) CST-simulated return loss (c) CST-simulated polar pattern of the sub-array at 28 GHz. Note that the polar pattern is along the axis of the array i.e., in the elevation plane.

Matching to the 50- Ω feed is based on a quarter-wave transformer. Full-wave EM analysis for the patch designed with the optimized dimensions in performed using CST studio suite, and the simulation results were extracted. Simulated $|S_{11}|$ and the far-field patterns (vertical plane) are shown in Figs. 4.4(b) and 4.4(c), respectively. The proposed antenna resonates at 28.05 GHz with a return loss of 27.41 dB. The tapered 28-GHz array results in a side lobe level lower than -18 dB in the elevation plane as compared to a -13 dB for the side-lobes for a non-tapered rectangular structure. The subarray layout was exported and the patch was fabricated using LPKF laser fabrication tool. The fabricated patch is shown in Fig.4.5 (a). The

measured return loss $|S_{11}|$ is shown in Fig.4.5 (b) and the patch resonates at 28.05 GHz with 800 MHz of bandwidth.

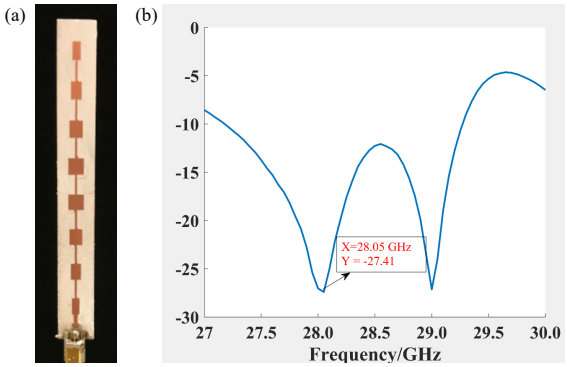

Figure 4.5: (a) Close-up image of the fabricated antenna sub-array. (b) Measured return loss of the fabricated antenna.

4.3.2 Patch antenna array

To develop the four-point FFT multibeam beamformer, a four-element ULA is designed and fabricated by replicating the available patch layout four times. The inter-element spacing of the four-element array that was used for the digital beamforming setup has been set to 0.75λ (8 mm) at 28-GHz. The antenna array is shown in Fig. 4.6. The inter-element spacing requirement for an antenna array to have Nyquist spatial sampling of 0.5λ [42]. Choosing 0.75λ would give rise to grating lobes within the scanning angle range $[-90°, 90°]$ [42] at the broadside of the antenna. However, these grating lobes would occur near to the edges, where the gain of the antenna is drastically reduced compared to the broadside at 0°. In turn, this extra spacing gives us more room to work, considering that the smallest available edge-mount connectors are atleast 6 mm wide. The left and right edges of the patch are at a distance of 16 mm $(2 * 0.75\lambda)$ from the subarray. This would completely reduce any fringing-field effects occuring at the edges of the patch array [42]. A sub-

miniature push-on micro (SMPM) edge connector is soldered onto the 50 Ω trace and is interfaced to the front-end circuits using a SMPM to 2.92mm cable.

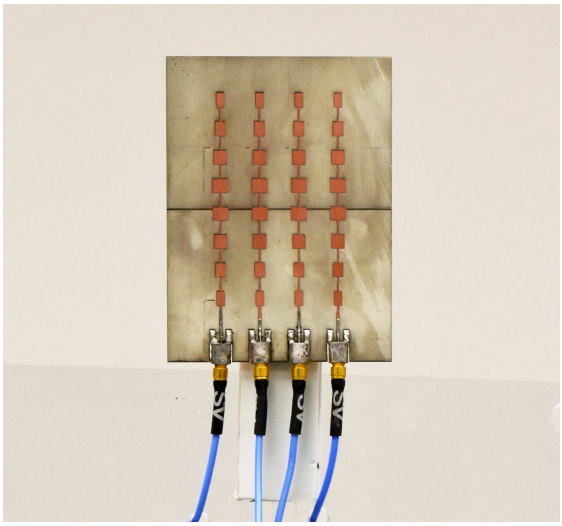

Figure 4.6: A four-element ULA developed from the single patch subarray with an inter-element spacing of 8 mm.

4.3.3 Receiver chain

The initial setup containing the ULA is verified with the downconverter component mentioned in Table 4.1. The receiver array front-end containing the ULA and the down-converter module is shown in Fig. 4.7(a). The downconverter module contains an Analog Devices HMC1065LP4E chip operating in the frequency range of 27 to 34 GHz with a baseband bandwidth of 4 GHz [4]. It provides a small signal conversion gain of 13 dB with 17 dBc of image rejection and 2 dBm of input intercept point (IP3). The Analog Devices chip utilizes an RF LNA followed by an I-Q mixer which is driven by an x2 active frequency multiplier as shown in Fig. 4.7(b). Due to this internal frequency doubler, the LO input can be driven at half the frequency of the RF band. IF1 and IF2 mixer outputs are provided, and an external 90° hybrid is needed to select the required sideband. The I/Q mixer topology reduces the need

for filtering of the unwanted sideband. A centralized LO distribution network is used to simultaneously and coherently drive all the channels from the array. This downconverter module is employed in our setup to mix down the 28-GHz band to baseband (up to about DC-1 GHz). The entire receiver array setup stands on a rotation platform with the support of polyvinyl chloride (PVC) pipes as shown in Fig. 4.7(c). The receiver array setup rotates in tandem with the rotation platform, which enabled us to measure the signals from each direction of arrival to plot the beam patterns.

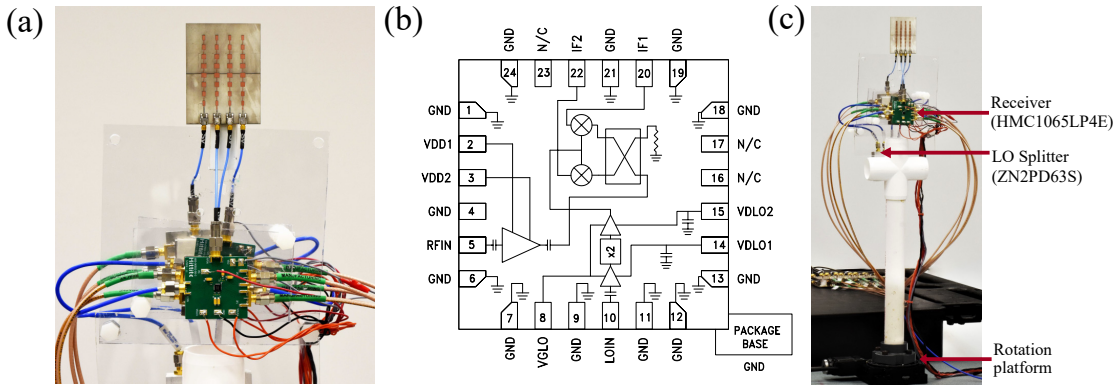

Figure 4.7: (a) Four-element receiver array front-end with HMC1065LP4E I-Q down-converter. (b) Functional block diagram of HMC1065LP4E [4]. (c) Receiver array mounted on a rotating platform

4.3.4 Digital back-end

A Xilinx ZCU1275 evaluation board [90] is used as the digital processing back-end of the 28-GHz array receiver. Fig. 4.9(a) shows a close up of the Xilinx ZCU 1275 board. The board contains a XCZU29DR-2FFVF1760E Zynq UltraScale+ RF-SoC chip, which integrates high-speed data converters along with a programmable logic fabric and application processing unit. Specifically, the chip supports 16 ADC channels up to 2 GSPS and 16 DAC channels upto 4 GSPS [5]. In the RF-SoC ar-

chitecture, the 16 ADC/DAC channels are distributed into four tiles, where each tile contains four ADCs/DACs as shown in Fig. 4.8(a). The ADCs/DACs on the RF-SoC can be configured through a "data-converter IP" included in the Xilinx Vivado IDE. This IP allows each tile of the RF-ADC or RF-DAC to be clocked either using an external clock input or using the phase-locked loop (PLL) that is inbuilt into each tile. Each RF-ADC and RF-DAC tile includes a clocking system with an input clock divider, a PLL, and an output divider. For any internal PLL use, the frequency system has the formula *Fs = (Fin/R)*(FBDiv/M)* as shown in Fig. 4.8(b), where Fs is the PLL frequency output and Fin is the reference frequency. When used with the SYSREF reference signal input, the clocking system can be synchronized in multi-tile or multi-device designs. The multi-tile synchronization mechanism is discussed in [5].

The ZCU1275 board is shipped with a HW-CLK-102 analog super clock module as a solution to provide phase-locked clocking to the data-converters. The HW-CLK 102 has two PLLs: PLL-A and PLL-B. PLL-A is able to provide four-phase aligned RF clocks in differential form for clocking the RF-ADCs and DACs in the RFSoC. PLL-B is able to generate two pairs of differential clocks. It also provides three phase-aligned reference clocks for synchronization. The programming instruction steps for configuring the clocks on this module are provided in [91].

The ZCU1275 board provides Bull's Eye interfaces to access all the RF SoC's data converters. The RF data converters with bulls-eye interface demand differential input signals for AC coupled operation mode, hence the I-Q downconverted signals are converted to differential from single-ended using a custom set of balun boards that contain the baluns (MiniCircuits TCM2-33WX+) shown in Fig. 4.9(b). The array receiver uses eight ADC channels in the RF SoC to synchronously sample the four I-Q IF signal pairs from the 28-GHz antenna front-ends in order to perform

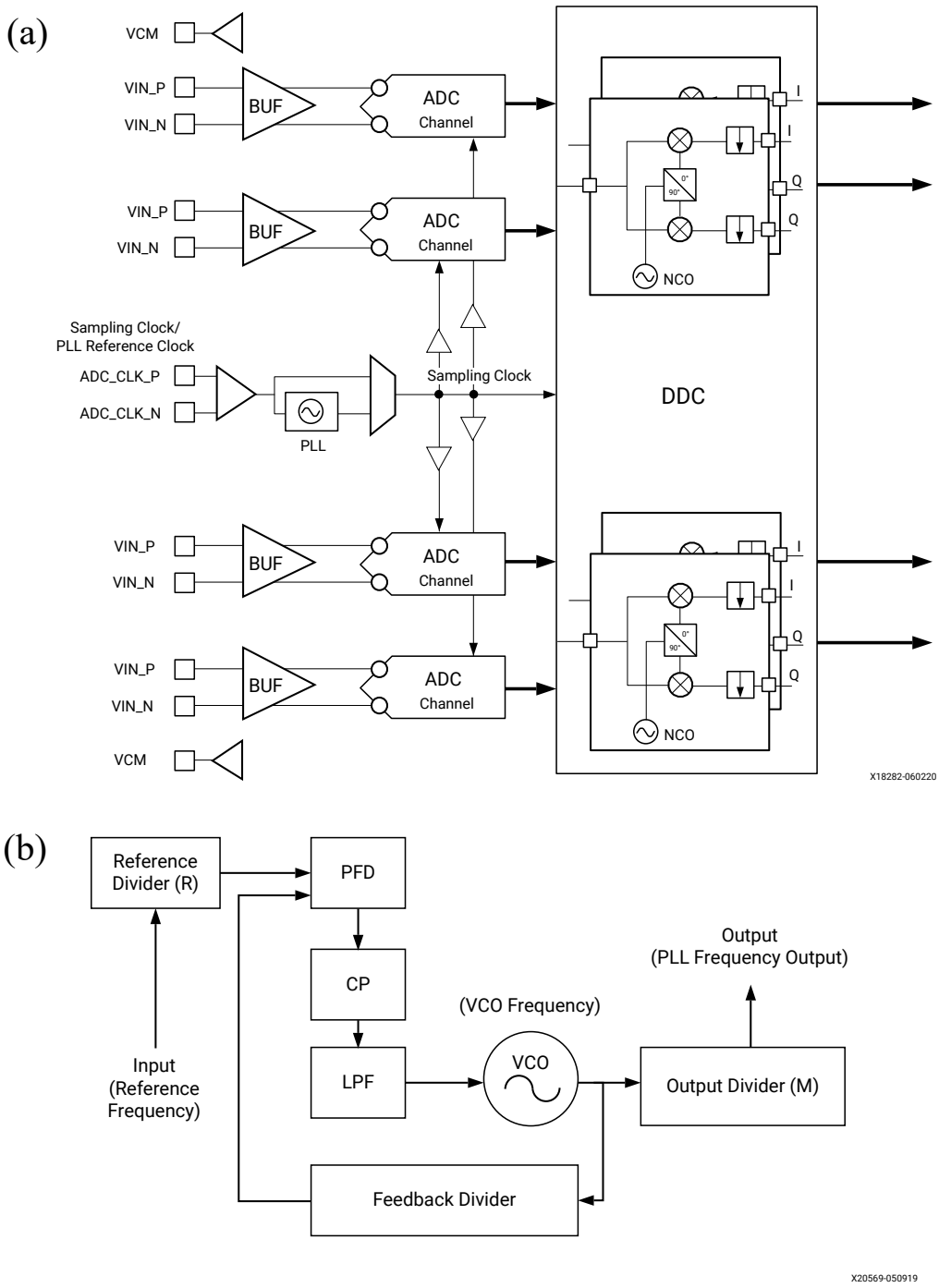

Figure 4.8: (a) RF-SoCs Quad RF-ADC tile overview (b) PLL clocking system in RF-SoC data converter chip. Taken from [5].

digital signal processing (DSP) in real time. Eight balun boards were fabricated on a 20-mil-thick RO4350B board were tested, and these boards are employed in our setup. Dr. Viduneth Ariyarathana has provided his support for this work by designing the custom balun boards and helping to configure the RF-SoC ADCs.

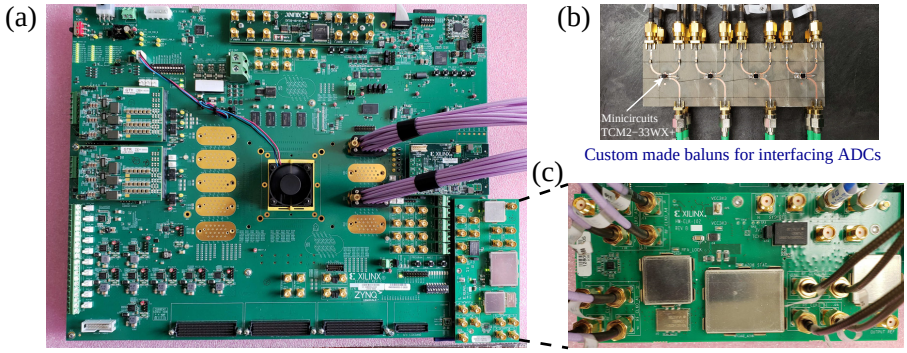

Figure 4.9: RF SoC digital back-end used for the implementation of four-point FFT beamformer at 28-GHz.

4.3.5 Four-point FFT digital design

In the experiments, the IF signals are connected to the data converters of the Xilinx RF SoC, which are configured to sample at 1966.08 MHz. Since the FPGA fabric cannot handle such high clock frequencies, a polyphase architecture containing eight parallel cores is employed for digital designs to accommodate the entire 850 MHz of bandwidth[1]. Therefore, the inbuilt first in first out (FIFO) of the XDCIP core was configured to output a sample rate of 1966/8= 245.76 MSps rate with 8 sampled words per clock edge streamed into the digital beamforming cores. The outputs of each FIFO clocked memory stream are synchronized to a single reference clock at 245.76 MHz that was derived from the analog sampling clock. The four-point FFT

[1]The polyphase digital architecture for this work is designed by Dr. Viduneth Ariyarathna

digital core is designed across the four spatial channels to realize four simultaneous beams. As shown in the Fig. 4.10, the digital design uses eight parallel such digital cores to process the entire sampled bandwidth.

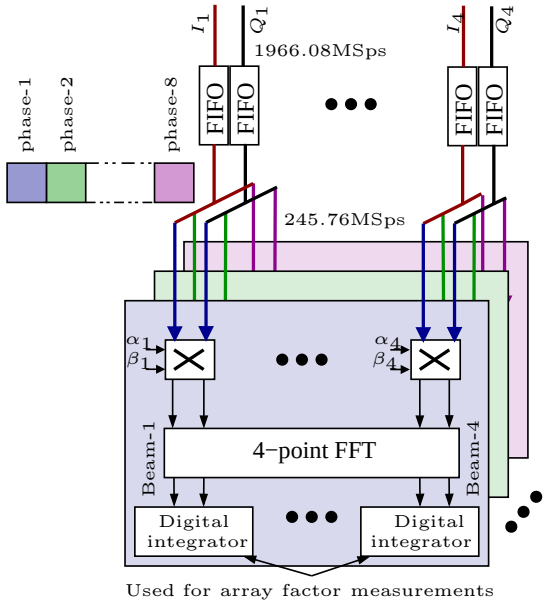

Figure 4.10: Architecture of the digital back-end with a four-point FFT digital core. Each core is realized in a polyphase manner to support wide bandwidths.

4.3.6 Real-time beamforming and measurement setup

Fig. 4.11 shows the entire 28-GHz transmitter and receiver array setup used for measuring beams in real time. A transmit horn antenna is used to send out a 28-GHz carrier onto the receiver array placed at distance of 1 m. The local oscillator frequency is set to 27.9 GHz to generate 100-MHz baseband signal. The accuracy of the measurements require RF chain and ADC calibrations. The next section talks about the calibration technique.

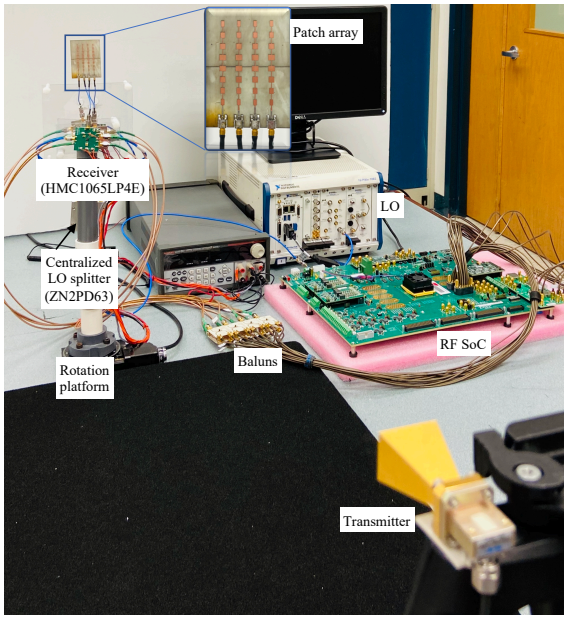

Figure 4.11: A 28-GHz transmitter and receiver array setup for taking measurements.

4.3.7 Calibration

The calibration mode of each ADC channel was set to "Mode-2" [5] in the XDCIP. In this mode, ADC calibration is handled by the start-up finite-state machine of the XDCIP. In addition, the RF front-ends were digitally calibrated using gain and phase correction. For this purpose, a complex multiplier is added at each phase of each channel as shown in Fig. 4.10. The gain and phase mismatches with respect to a reference receiver were pre-measured using a reference signal. Complex calibration constants $\alpha_i + j\beta_i$, where $i = \{0, 1, 2, 3\}$ and $\{\alpha, \beta\} \in \mathbb{R}$, were then estimated for each channel. Typical I and Q baseband channel data measured before calibration at an IF of 100 MHz are shown in Fig. 4.12(a), whereas Fig. 4.12(b) shows the digitally calibrated versions that are fed into the digital beamforming cores.

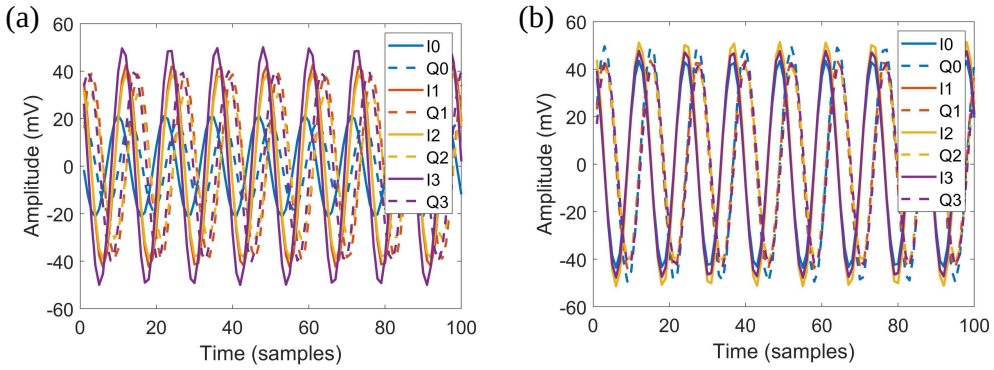

Figure 4.12: (a) The sampled I and Q channels of each baseband signal at an IF of 100 MHz. (b) The digitally-calibrated channels fed to the digital beamforming cores.

4.3.8 Real-time beam measurements

For measurement of the beam patterns, the angle of arrival of the incident wave was slowly varied by rotating the receiver array. The beamformed outputs of each beam of each phase is then used to compute the received energy for each direction of arrival using digital integrators. Fig. 4.13 compares the measured and simulated beams that correspond to outputs of 4-bins of the 4-point FFT operation. Measured beams are indicated in red and the simulated beams in blue. Simulated beams are generated from fixed-point simulations of the four-point FFT design in Matlab Simulink, and they do take the element pattern into effect. The beam look directions are set by the antenna spacing and adhere to the values given by (4.2). The beam corresponding to bin-1 points to the bore-sight direction (0°) whereas bin-2 and bin-3 produce beams at ±19.5°. Since the antenna array is not Nyquist spaced, grating lobes occur for angles beyond ±41.8° and, hence, the beam corresponding to bin-3 points at ±41.8° with two main lobes.

The plots convey that the measurements and simulations are well-matched with respect to beam direction as well as side lobe performance, thus validating the proposed 28-GHz four-element digital array receiver. Hence, this prototype 4-element

receiver array can be scaled to higher number of antenna elements to produce more number of simultaneous multi-beams which could be a subject of future work.

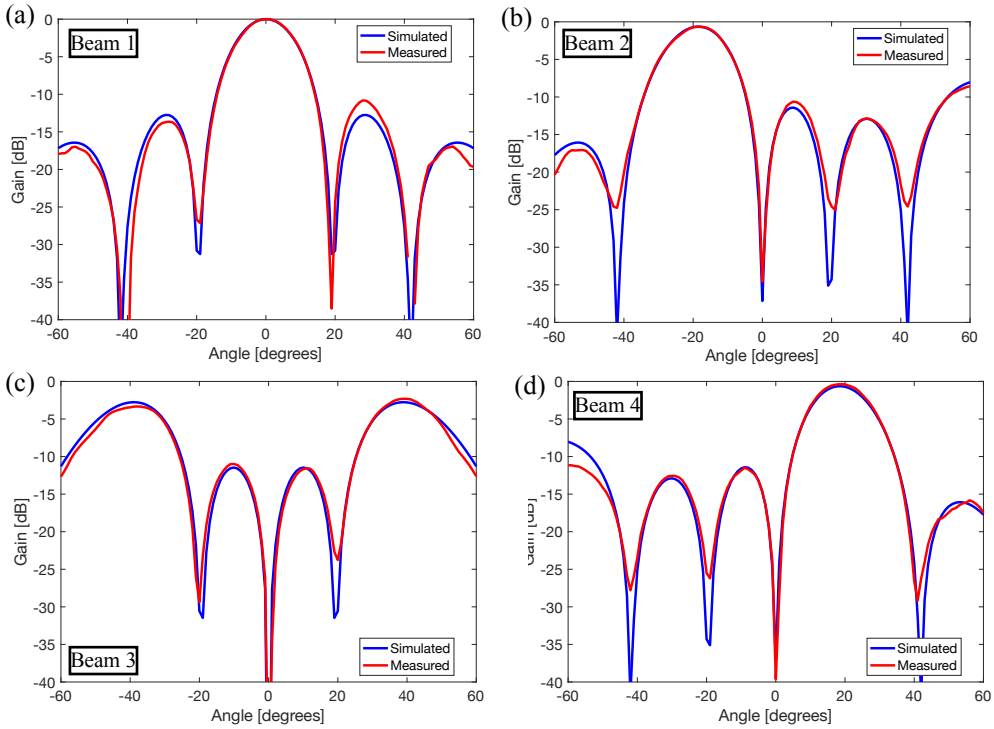

Figure 4.13: Four-point FFT real-time digital multi-beam beamforming at 28 GHz. Simulated and measured beam patterns corresponding to each output of the FFT multi-beam beamformer at $f_{IF} = 100$ MHz.

4.4 Contribution and comparison to previous work

The concept of Fourier transforms is well-known and the attempt to realize simultaneous multi-beams using 8-point, 16-point, 32-point FFT algorithms has been accomplished in our prior works reported in literature [73, 92, 93]. In [93], the authors have implemented a 32-point FFT on a 32-element 5.8-GHz receiver array with ROACH-2 digital hardware platform as its digital back-end to achieve 32-orthogonal simultaneous beams. Similarly, the other multi-beam beamformer implementations

have been limited to sub-6 GHz bands. In this work, we demonstrated a fully digital FFT based multi-beam beamformer at mmW frequencies (27.3-28.5) GHz with Xilinx RFSoC–based digital back–ends. The 28 GHz beamforming implementations that have been reported prior to this work have been limited to analog implementations such as the ones in [94–96]. This work utlilized the concept of FFTs to realize fully digital simultaneous multi-beams at mmWave frequencies and leverages the larger bandwidths supported by the latest Xilinx RF-SoC–based digital hardware platforms. To accommodate such larger bandwidths on a FPGA fabric, we developed polyphase architectures. The design details of such an architecture was discussed here as well. These 28-GHz multi-beam wideband implementations are very likely to be used in the future mmWave wireless access points to achieve maximum capacity in a multi-path channel scenario. This work presented complete design details for a four-element 28-GHz implementation using an RF-SoC platform that are capable of handling signals up to 800-MHz bandwidths. Beam patterns measurements are conducted to verify the proposed work. The design details presented here could very well be used for implementing larger arrays.

4.5 Conclusion

This chapter presented a four-element digital beamforming array receiver at 28 GHz. The RF-front end including a custom-designed high-gain four-element ULA of patch antennas is integrated with a Xilinx RFSoC-based ZCU1275 platform as the digital back-end. The Xilinx RF-SoC platforms are equipped with high-speed RF data converters and are used for huge bandwidths at mmW frequencies, in our case 800 MHz at 28 GHz. Two ADC tiles in the RFSoC have been used to sample all eight I-Q channels into digital to perform a four-point spatial-FFT–based

multibeam beamforming to produce four simultaneous mmW beams. Polyphase digital architectures have been employed to support the full baseband bandwidth as the permitting FPGA fabric clock rate is way less compared to the ADC sampling rate. The measured digitally formed multi-beams are very well in agreement with the simulated beams, thus validating our implementation.

This 28-GHz array receiver is also employed by my ex-colleagues Dr. Viduneth Ariyarathna and Dr. Najath Akram in their respective Ph.D. research studies [87, 88]. Dr. Ariyarathna has contributed towards construction of the 28-GHz setup and fabrication of the balun boards needed to interface the analog front-end to the ADCs of the RF-SoCs. He also helped in RF-SoC configuration, ADC calibration, and building of the polyphase architecture for the FFT digital design.

CHAPTER 5

MULTI-BEAM BEAMFORMING USING LENSES AND FOCAL PLANE ARRAYS

The previous chapter discussed the theory of multi-beam beamformers using digital Fourier transforms, and presented a four-point FFT implementation to realize four simultaneous RF beams. Such a beamforming approach is known as an aperture array beamformer, where an array receiver is used in conjunction with a digital algorithm to create beams. Whereas analog implementations use front-end analog electronics to achieve beamforming through approaches such as RF phase shifting [97], progressive transmission line delays [98], analog all-pass filters to realize the true-time delays [99, 100], Butler matrices [62, 63], analog lenses [101, 102], and others. Of these implementations, beamforming using phase shifters is the most conventional and widely used method. However, phase-shifting based approach is narrow band and possess highly complex architectures. Lens-based architectures replace the network of analog phase shifters with a lens in order to reduce the complexity and power consumption. This chapter discusses a lens and focal plane array (FPA) assembly where multi-beam beamforming is achieved along with high gain supported by the lens. This is the first attempt to realize a lens and focal plane array beamformer at a mmWave frequency of 28 GHz.

This chapter begins with a discussion of the motivation and background for the lens-based approach and continues with the architecture needed for such an approach. A four-element, 28-GHz receiver array to realize four simultaneous high gain beams is designed. An acrylonitrile butadiene styrene (ABS) dielectric lens is chosen for this work and a four-element, 28-GHz patch antenna array attached to its base acts as its focal plane array. The lens design and simulations are presented before we discuss the system implementation and the measurements. A Xilinx RFSoC

based ZCU 1275 platform was used as the digital back-end for sampling the four I-Q channels with its integrated, high-speed RF ADCs clocked at 2 GHz. The measurements are provided for a 100-MHz IF signal with with a carrier frequency of 28.1 GHz, and these measurements are compared with simulation results for evaluation purposes. This work is done in collaboration with Dr. Shubhendu Bhardhwaj; he designed the 28-GHz lens as per the requirements and specifications. The contents of this work and the results have been published in [75] and were presented at the 2020 International Microwave Symposium.

5.1 Background

Wireless communications in the mmW bands require highly directional beams to circumvent high path loss. However, as wavelength is reduced with an increase in frequency, for a given physical aperture size, the antenna produces gains that are high enough to maintain link budgets. The use of aperture arrays allows maximum flexibility in digital beamforming. Nevertheless, sharp beams (i.e., beams with high gain) can only be achieved with large numbers of antennas and their dedicated transceivers, making aperture arrays a relatively high-complexity (and a higher cost) approach. Dielectric lens antennas are of great interest in this regard because they allow high-gain with beam steerability when fed using a focal plane array (FPA) [103, 104]. The use of the lens allows sharper beams due to the inherent high-gain arising from the larger physical aperture of the lens, albeit at the same degrees of freedom as an aperture array, because the number of degrees of freedom depends only on the number of independent channels (i.e., four). The spatial filtering algorithms, in conjunction with the FPA feed, are used to mitigate radio frequency interference [39, 105]. Exploiting the high gain lenses along with beamforming abilities of the

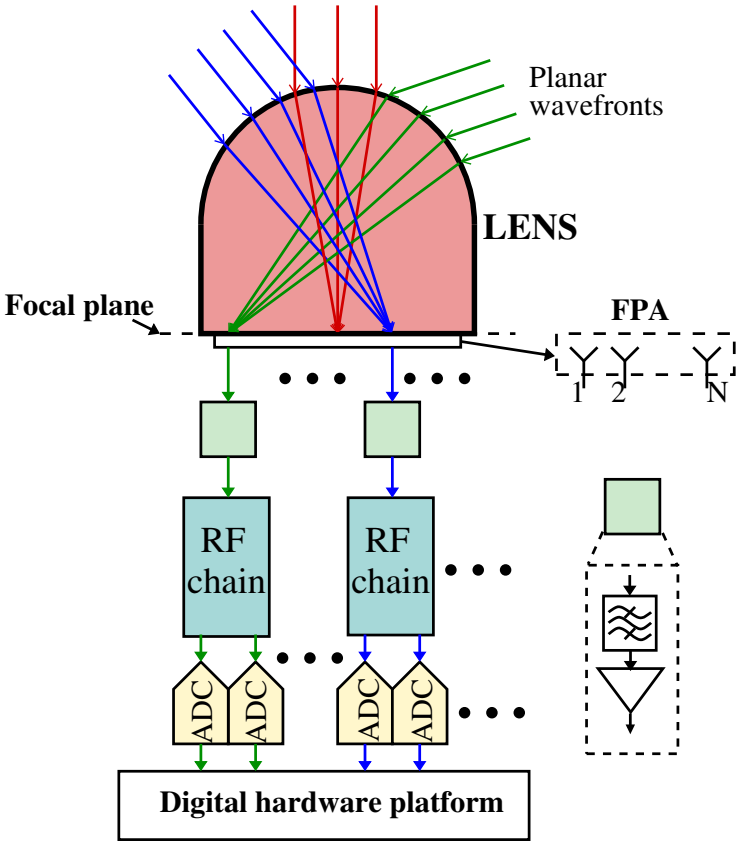

Figure 5.1: Architecture of a lens + focal planar array (FPA)–based multi-beam beamforming.

aperture antennas has critical applications for the upcoming 5G/6G communication links [106]. The digital beam forming on the array aperture allows multiple beams, while the lens allows for gain enhancements and directivity improvements in such approaches.

5.2 Architecture of multi-beam beamforming using lens and FPA assembly

Figure 5.1 shows the system architecture of a lens + FPA multibeam beamformer to realize multiple simultaneous beams. The antenna array is located on the focal

region of the lens and hence, is termed as an FPA. The lens is an analog passive device that uses refraction to compute a spatial Fourier transform in the frequency band of interest. The plane waves impinging onto the lens surface at a specific angle will converge at a unique point on the focal plane of the lens as shown in Fig. 5.1. So for every DOA, we probe at that particular point on the focal plane fo the lens to capture the incoming plane wave. The number of beams realized is equal to the number of sensors/antennas located on the focal plane. Each element of the FPA is connected to dedicated receivers (or transmitters) that are interfaced to digital radio for post-processing.

5.3 Design of a four-element, 28-GHz multi-beam beam-former

To realize and verify the multi-beam production using a lens based approach, dielectric lens is designed specific to 28-GHz band. A 28-GHz, four-element array serves as the FPA and is connected to four dedicated direct-conversion receivers. The digital back-end employs a Xilinx ZCU 1275 RF-SoC digital platform to generate four 28-GHz RF receive-mode beams with a bandwidth of 850 MHz per beam. The following sections discusses the lens design, array setup, simulations, and measurements. The lens used for this work is designed by Dr. Shubhendu Bhardwaj at FIU.

5.3.1 Lens design

A hemispherical lens with a cylindrical base was designed by first determining the aperture area of the lens based on the desired directivity of 29 dBi and then by

calculating the height of cylindrical section based on the known dielectric constant of the ABS printing material. A lens radius of $r = 5$ cm was used to obtain a directivity $D = 10log(4\pi \times 2\pi r^2/\lambda^2)$ of 29.3 dBi for $\lambda = 10.7$ mm at 28 GHz. The geometry of the designed lens is shown in Fig. 5.2(a). The hemispherical lens is indeed an approximation of ellipsoidal lens with an antenna positioned at the focus. An elaboration of the equivalent design equations for this approximation can be found in [107]. The length of the base is calculated to be $L = 5.7$ cm using the following design equations [107],

$$L = b\frac{1+\frac{1}{n}}{\sqrt{1-\frac{1}{n^2}}} - r \quad \text{where } b = r(1+\frac{1}{3n^2}). \tag{5.1}$$

Here $n = \sqrt{\epsilon_r}$=1.581 is the refractive index of the ABS material as per $\epsilon_r = 2.5$. The performance of the array and lens structure was then evaluated using full-wave electromagnetic simulation as shown in Fig. 5.2(a). Beam steering is made possible by changing the position of the 1D array x_o, which emulates the excitation of two of the four 1D arrays implemented in the patch array. The beam position by considering two other positions x_o= -4 and -12 mm (not shown in the figure) are found to be at symmetrical elevation angles. Simulation and measurement results of patch antennas with lenses are shown and discussed in Figs. 5.2(c) and (d).

5.3.2 28-GHz digital array receiver specifications

The 28-GHz four-element array receiver designed for FFT multibeam beamformer in Chapter 4 is employed for this work as well. The RF front-end consists of a 28-GHz four-element patch antenna array supported by four downconverters. Each individual antenna has been built as an eight-element series fed vertical sub-array to provide higher gain in the elevation plane to aid the real-time beam measurements. The four-element patch antenna array is taped to the back of the lens on its focal

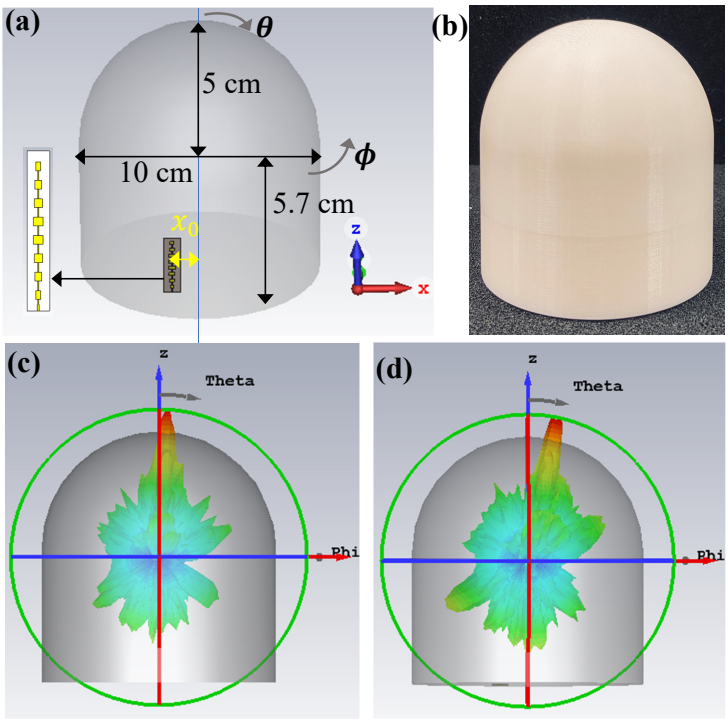

Figure 5.2: Validation of the lens + 1D array using full-wave electromagnetic simulations using CST studio suite. (a) Designed lens structure along with dimensions. Parameter x_o was varied as $x_o = -12, -4, 4, 12$ mm to emulate the beams radiated by the four 1D arrays. (b) 3D printed lens used for measurements. 3D beams with peak at $\theta = 4^o$, 12^o resulting due to $x_o = 4$ and 12 mm are shown in (c) and (d) respectively. For $x_o = -12, -4$ mm cases, beams in opposite directions were obtained (not shown).

plane and serves as the focal plane array/ feed array. For the 28-GHz receivers, a HMC1065LP4E downconverter chip from Analog devices is used to mix down the 28-GHz RF signal to baseband. The I-Q downconverted signals are passed through the balanced-to-unbalanced RF transformers baluns (sourced from MiniCircuits TCM2-33WX+) so as to interface to the ADCs of the digital back-end RF SoC.

The digital back-end is implemented using Xilinx ZCU-1275 [86] development platform, which incorporates a Zynq Ultrascale+RF SoC. The array receiver uses eight ADC channels in the RF SoC to synchronously sample the four I-Q IF signal pairs from the 28-GHz antenna front-ends in order to perform digital signal processing (DSP) in real time. Similar to the one designed for FFT multi-beam measurements, a digital design with polyphase architecture containing eight parallel cores is employed. The polyphase architecture is needed to accomodate the 850-MHz bandwidth. Calibration of the RF front-ends were performed by employing a complex multiplier at each phase of each channel to correct the gain and phase mismatches. Comprehensive details of receiver design and specifications along with digital back-end details can be found in Chapter 4.

5.3.3 Measurement setup for 28-GHz lens

The experimental setup to measure the RF beams is shown in Fig. 5.3. A 28-GHz horn antenna is used as a transmitter and LO is set to 27.9 GHz. Eight ADC channels of Xilinx RF SoC are configured to sample the four I-Q signals at 1966.08 MHz. To emulate the direction of arrival for beam pattern measurements, the array setup is rotated along its axis while keeping the transmitter fixed. ADC samples from each channel are passed onto a digital integrator block to compute the gain for the respective angle.

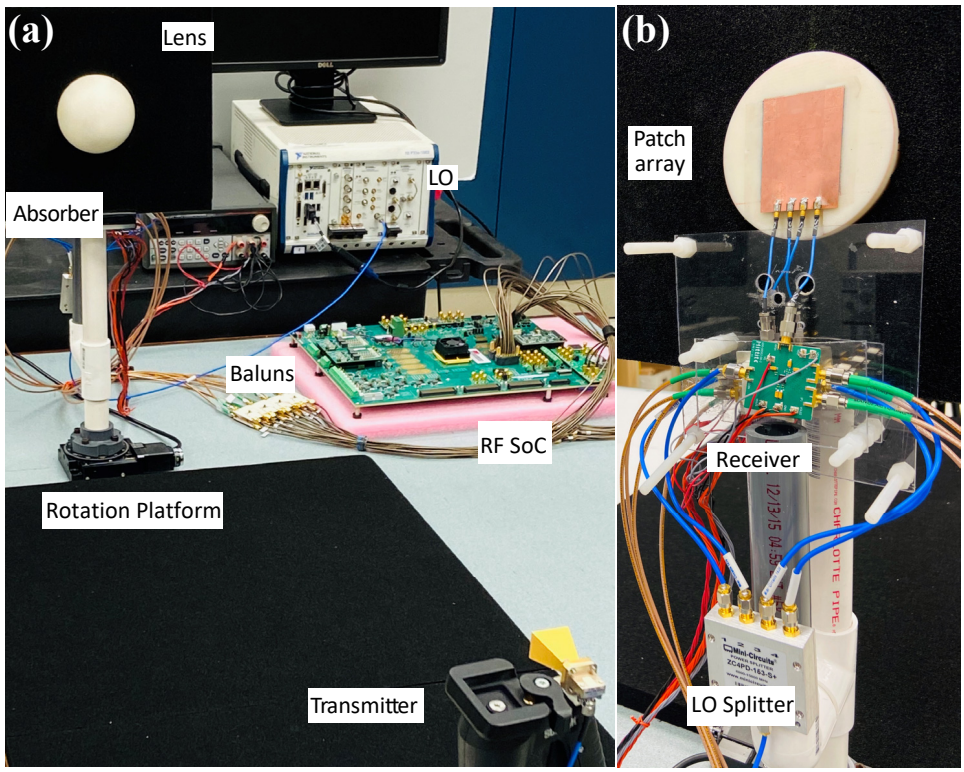

Figure 5.3: (a) Experimental setup with digital back-end RF SoC system and local oscillator (b) Receiver chains for the four-element FPA (and aperture array) with array taped to the base of the ABS plastic lens. The LO is split four-ways using a microwave divider network.

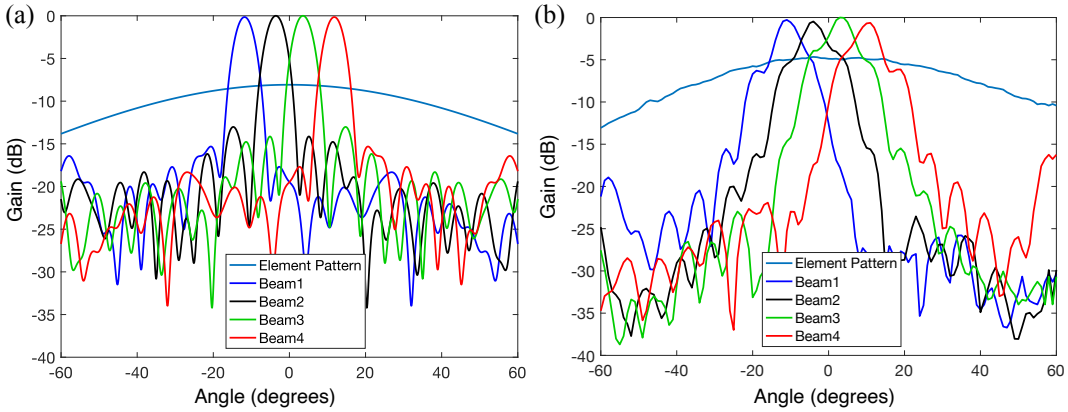

Figure 5.4: (a) Simulated normalized gain patterns of the beams using fullwave electromagnetic simulation using CST studio suite. Elemental subarray gain pattern (normalized by the maximum of beam pattern) is shown for comparison. (b) Measured normalized gain patterns of the beams extracted from RF SoC and corresponding normalized elemental subarray pattern.

5.3.4 Measured 28-GHz lens + FPA digital beams

Fig. 5.4 (a) shows the normalized gain patterns of the lens and array configuration using the CST simulation setup shown in Fig. 5.2. The 4-beams are indicated in red, green, black and blue. The elemental pattern (1D patch subarray without a lens) is also shown in sky blue, showing the relative gain improvement due to introduced lens. Similar beam patterns and elemental subarray patterns were also extracted from the measurements utilizing the RF SoC platform for digital signal processing. For this measurement, the LO was set to 27.9 GHz at mixer to provide 100-MHz IF signal. Fig. 5.4(b) shows the corresponding measurements obtained from the Xilinx RF SoC ZCU 1275 digital platform, where it independently received and integrated the samples from each of the receivers connected to the FPA at the base of the lens. Comparing the simulation and measurement results, we observed there is good agreement in the position of the beam in elevation space and gain enhancement of 8 dB is noticed due to lens placed over the patch array. This gain

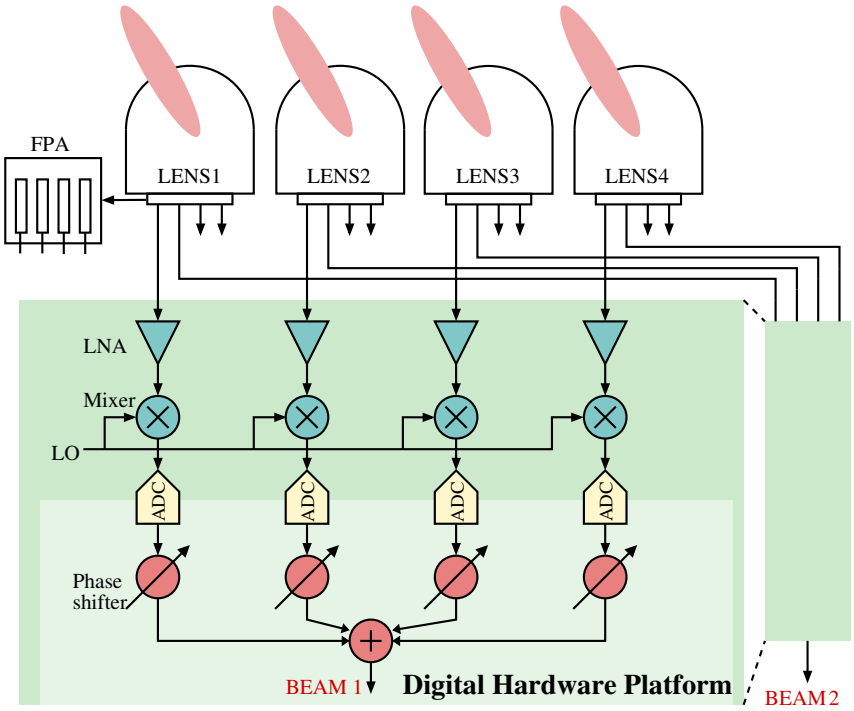

Figure 5.5: System overview of cascaded Lens + FPA multibeam beamformer to generate sharper beams.

is much smaller than the anticipated gain of the lens, since the theoretical design equations of the lens assumed an isotropic point source positioned at the focus of the lens. In practice, due to its high gain, 1D subarray's focal point lies behind the base of the lens and should be adjusted to match with lens' focal point. These effects were not considered in current work and will be part of our future work. Furthermore, comparing the simulated and measured peak gain values, 2 to 3.5 dB difference between the simulated and measured data is observed. We expect these differences to be due to (1) material losses in ABS material, which are not accounted for in the simulation model and (2) due to uncertainties in the knowledge of dielectric constant which is reported to be between 2.5 to 3.0 in prior literature. Consideration of these effects will further improve the effectiveness of the lens design and will be the subject of future work.

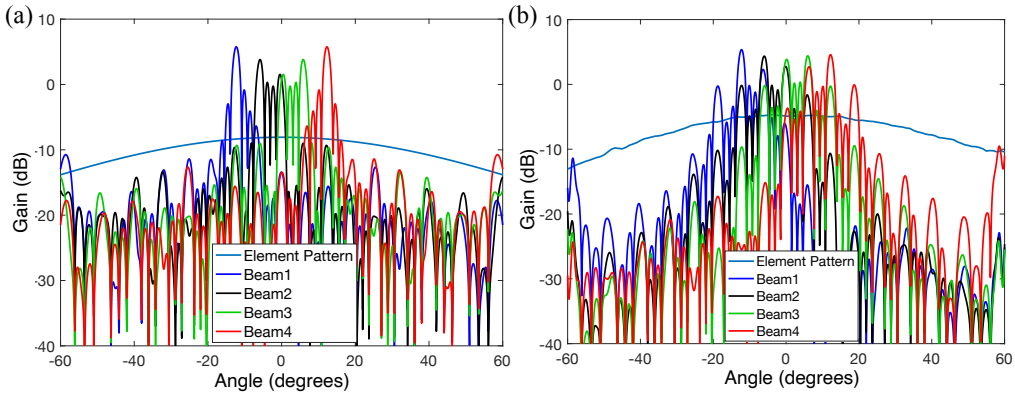

Figure 5.6: (a) Simulated beam patterns from lens+FPA setup for a lenslet array. (b) Simulated beam patterns obtained from cascaded lens+FPA setup using measured lens beam data.

5.3.5 Simulated 28 GHz beams using lenslets

The beams obtained from the original setup can be further narrowed down by cascading several such array structures and feeding to a phased array digital beamformer. A system overview of such lenslet approach is shown in Fig. 5.5. A MATLAB simulation is set up to illustrate this effect using measured data from a single lens. The setup assumes four lens+FPA (current setup) placed next to each other, such that interelement distance between two corresponding antenna elements is equal to the diameter of the lens i.e., 10 cm. To compute the beampatterns for this setup, measured beampattern for one antenna is multiplied with the array factor of a four-element phased array beamformer. Fig. 5.6 (c) and (d) shows the simulated and measured beampatterns respectively. It is observed that the beams are much narrower now and provide an additional gain of 6 dB achieved due to the 4-element digital phase shifting beamformer. We can use additional windowing methods in our digital approach to improve side-lobe performance in the obtained beam measurements.

5.4 Contribution and comparison to previous work

We have discussed in the early stages of this dissertation that there are several ways of performing analog beamforming; using phase shifters [97], Butler matrices [62, 63] or analog lenses. Phase-shifting approaches are narrow band and possess highly complex architecures. Lens–based architectures replace the network of analog phase shifters with a lens in order to reduce the complexity and power consumption. Similarly, lens based architectures are better compared to Butler matrices in terms of implementation complexity, broadband performance and flexibility of choosing arbitrary number of beams and array ports. The use of lens in the beamforming setup will not only allow formation of multiple sharper beams which are essential to overcome high path losses but also exploit multi-path channels in a typical mmWave wireless communication scenario.

A discrete lens array beamforming for continuous aperture phased (CAP) MIMO is discussed in [25]. Analog beamforming based on Fourier Rotman lens for multi-beam applications are discussed in [108, 109]. Unlike the discrete array or dielectric lens–based approach, in the Rotman lens, the output ports are lower than the number of the elements in the antenna array, hence reduction in number of beams. The array implementations for the above reported work in literature are under 10 GHz. A multi-beam MIMO prototype for real-time multi-user communication at 28 GHz is reported in [104]. The authors in [104] utilized a Xilinx VC707 evaluation board with Virtex-7 FPGA as its digital back-end. Whereas, in this work, we employ a Xilinx ZCU1275 evaluation board with a XCZU29DR RF–SoC FPGA chip as the digital back-end. The RF–SoC architectures are very advanced compared to the VC707 architectures since they integrate high speed RF ADCs with an FPGA on the same chip and contain several other sophisticated features as mentioned in Chapter

4. By employing a RF–SoC based architecture, we can realize a wideband lens based beamformer. The objective of this work is to discuss how a powerful FPGA platform that is available to us can be used for a lens plus FPA based analog beamformer. In this work, we designed a dielectric lens–based analog beamformer that incorporates a 4-element, 28-GHz patch antenna receiver array as its focal plane array to realize four simultaneous high gain beams with a bandwidth of 850 MHz per beam. The lens antenna design, CST studio simulations, configuration of integration of the RF front-end with RF-SoC–based digital back-end are all discussed in detail. The measured beams for a 100 MHz IF case were reported and are compared with the simulated beams. While the results are promising, addressing the hardware impairments would achieve the full potential of our lens based beamformer. We have also proposed a hybrid beamforming approach that integrates lens–based analog beamformer in level-1 and a digital phase shifting beamformer in level-2. This cascaded lens array architecture would further narrow down the beam patterns and produce much sharper beams. This approach is also validated by the measurements obtained from the lens setup.

5.5 Conclusion

This chapter presented an analog implementation of a multi-beam beamformer using a lens and a focal plane array setup at 28 GHz. Lens based architectures replace the conventional analog phase shifters to produce sharp beams with reduced complexity and power consumption. The lens dimensions are designed to provide a directivity of 29 dBi with ABS as its dielectric material. It was 3D printed and is attached to four-element ULA of patch antenna array operating at 28 GHz, acting as a focal plane array. The Xilinx RFSoC based ZCU1275 platform is used as the digital

back-end here as well due to its support for high bandwidths. The four I-Q channels sampled at 2 GHz are passed to the digital circuits implemented in the RF SoC's programming Logic (PL). This core is constructed with a polyphase architecture similar to the one in Chapter 4, and it realizes an integration logic to compute the power for each channel/beam. The measurements were carried out for a 28.1-GHz transmit frequency producing a 100-MHz IF. The simulated array factors are generated using Microwave CST studio suite. Although the gain enhancement due to the lens is not as anticipated, the beam positions are very well aligned which validates our implementation. Further, the measured data is used in simulating a lenslet array, an hybrid beamforming approach to provide very sharp beams with certain degrees of freedom arising from the digital end.

CHAPTER 6

REAL-TIME FPGA BASED MULTI-BEAM DIRECTIONAL SENSING

The review chapter introduced us to various applications of beamforming especially for the multi-beam beamforming approaches. In this chapter we explore one such application that relates to the RF directional spectrum sensing for exploration of white spaces within the spatio-temporal regions. In this work, a real-time directional sensing system is proposed for 2.4-GHz ISM band by exploiting the concept of spatio-temporal spectral white spaces. The proposed system consists of a 16-element patch antenna array supported by a 16-point FFT-based multi-beam beamformer. A ROACH-2 based digital hardware platform is used as our digital back-end to sample the incoming 16 I-Q streams and also to realize the FFT beamformer and the energy detectors. This energy detector is a simple integrate-and-dump circuit used to compute power for directional sensing. The system design details, digital back-end details and the measurements obtained using Wi-Fi devices to verify the proof-of-concept are all presented as the chapter proceeds. This work is done in collaboration with Dr. Chamira at University of Moratuwa and Dr. Chamith at University of Queensland. This work has contributed to one publication [110], and the content of this chapter is based on the same publication.

6.1 Background

Abundant growth and usage of wireless devices led to scarcity of the available radio spectrum as the wireless frequency channels being occupied are increasing with time [111–113]. Spatio-temporal properties of the wave propagation is a hot topic that is being explored for frequency reuse. This scheme adopts sharing of the carrier

frequencies as a function of the wave propagation direction. Wireless channels are sparsely spread in the spatio-temporal frequency domain and the white spaces within these regions can be used for directional channel multiplexing for increased system capacity [114].

There are many theories and implementations to alleviate the spectral scarcity that are discussed in this section. Cognitive networks exploit the opportunistic communication channels via a spectrum sensing and monitoring subsystem within an overall dynamic spectrum management and allocation system [111–113,115,116]. Similarly, there are approaches that explore the opportunistic spectral access via spatial domain sparsity i.e., spatial reuse of the available spectrum [117–126]. These approaches exploit directional transmission and reception using various methods of beamforming.

This chapter proposes a RF multi-beam array receiver for the sensing of RF sources operating at 2.4 GHz ISM band, such as Wi-Fi devices. This spectrum sensor takes into account both channel frequency and direction of propagation. The directional spectrum sensing is employed at baseband stage of the RF using spatially bandpass beamfilters implemented using FFT algorithms. This is more efficient compared to the directional spectrum sensing presented in [114], because of the significantly lower temporal sampling in our approach.

6.2 ROSs of the spectra of plane waves and white spaces

In this section, we look into the theory of directional sensing of an electromagnetic wave emanating from an RF source [1]; in our application a Wi-Fi enabled device located in the far field by a ULA as shown in Fig. 6.1(a). In Chapter 2, we have looked

[1]Equations and the mathematical analysis involving the multi-dimensional space-time spectrum theory in this section is provided by Dr. Chamira Edussooriya.

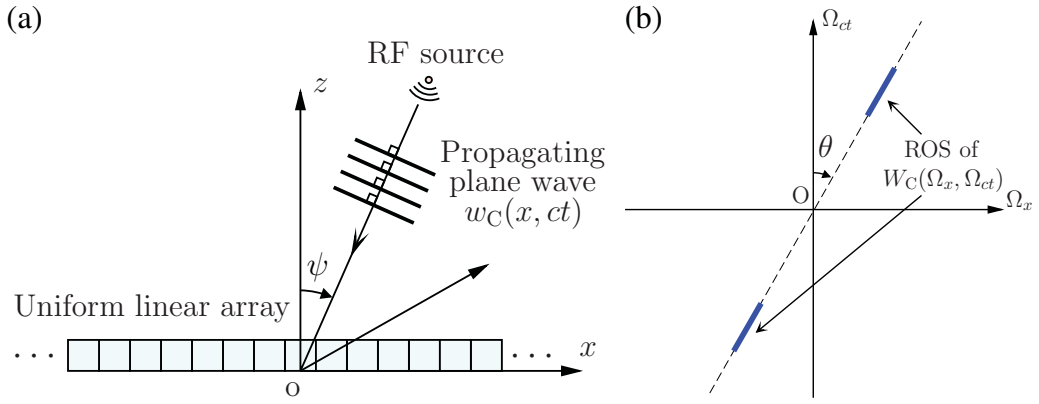

Figure 6.1: (a) An RF signal received by a ULA; (b) The ROS of the spectrum of a plane wave signal in the 2D frequency domain.

into the spectral properties of a 2D spatio temporal PW received by a ULA. Considering $w_C(x, ct)$ be the incoming PW in the 2D continuous temporal domain (x, ct) arriving at an angle ψ, we concluded that its ideal continuous-domain spectrum say $W_C(\Omega_x, \Omega_{ct})$ lies on a straight line going through the origin of $(\Omega_x, \Omega_{ct}) \in \mathbb{R}^2$. Precisely, ROS consists of two segments lying on that straight line as shown in Fig. 6.1(b), where the length of the segments is determined by the temporal bandwidth of the plane wave.

However, for an RF signal having a fractional bandwidth less than 50%, temporal sampling at the baseband is more economical than at RF stage. Hence, the signal is downconverted to the basband using LOs, processed through low pass filters and provided for quadrature sampling with I and Q components. Assuming $w_D(n_x, n_{ct})$ is quadrature-sampled 2D discrete domain signal, the ROS of its spectrum $W_D(\omega_x, \omega_{ct})$, consists of line segments inside the principal Nyquist square $\mathcal{N}$ [64,127] as shown in Fig. 6.2(a). It can be observed that this line segment is generated by down-shifting the upper segment of the ROS of $W_C(\Omega_x, \Omega_{ct})$. The principal Nyquist square $\mathcal{N}$ is defined as region where $\{(\omega_x, \omega_{ct}) \in \mathbb{R}^2, -\pi \leq \omega_x, \omega_{ct} < \pi)\}$,

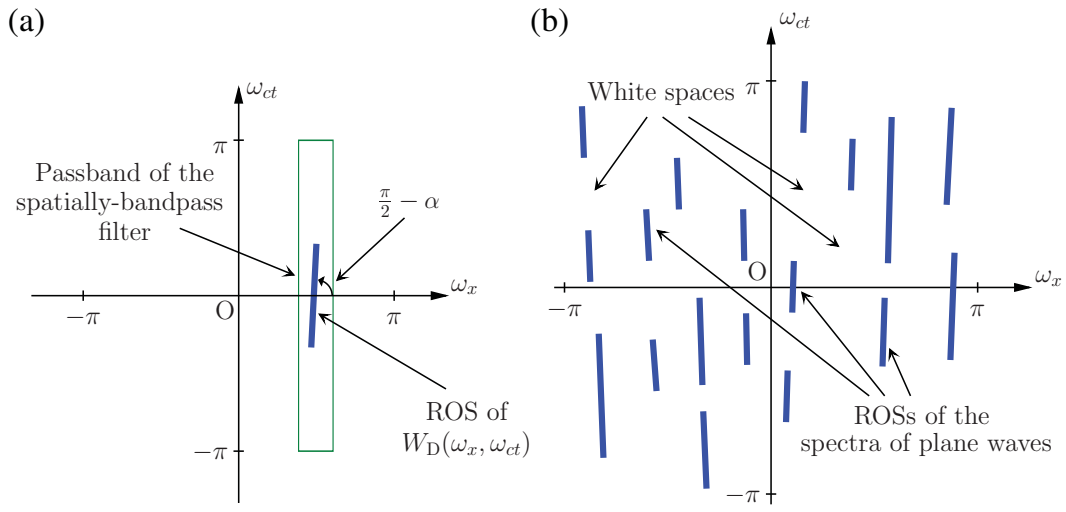

Figure 6.2: (a) The ROS of the 2D spectrum of a quadrature-sampled plane wave; (b) ROSs of the spectra of plane waves and white spaces.

and $\omega_i = 2\pi\Omega_i/\Omega_i^S \text{for} i = (x, ct)$, where Ω_i^S is the corresponding sampling frequency. If we consider the case where M (≥ 2) plane waves with different DOAs are received by the ULA, the ROSs of the spectra of quadrature-sampled plane waves consist of M single line segments inside the principal Nyquist square $\mathcal{N}$ as shown in Fig. 6.2(b). The location of a straight line segment depends on the temporal bandwidth and the DOA of a plane wave. The presence of a plane wave or the absence of a plane wave (i.e., a white space) with respect to the DOA can be sensed using a multi-beam beamformer having spatially bandpass responses as described in the next section.

6.3 Sensing over multi-beams

The 2D spectrum of a discrete-domain plane wave is computed by using the 2D discrete Fourier transform (DFT) using the FFT algorithms [128]. The 2D DFT is a row-column separable operation. Therefore, we may compute the spatial FFT

for each temporal sample, and then compute temporal FFTs along each of the spatial-FFT's column outputs, which appear as temporal sequences. The outputs of the spatial-FFT bins are in fact directional RF beams, with beam axis defined by the bin number of the spatial FFT. The N-point spatial-FFT can be computed using fixed-point arithmetic at arithmetic complexity $\mathcal{O}(N \log N)$ or approximated at low-complexity without using any multipliers at all, with about a 2 dB loss in directivity [92].

6.4 Design of a 16-element FFT multi-beam based directional sensor for 2.4 GHz Wi-Fi sources

To verify the concept of directional sensing, a multi-beam beamformer is designed using spatial-FFT and is realized on an FPGA. The beamformer produces RF beams, which are in the mixed spatial-Fourier-temporal domains. These beams are used here for directional sensing using energy detectors presented in Sec. 6.4.2, for real-time directional sensing of 2.4-GHz Wi-Fi sources.

This section presents the 16-element RF receiver array setup, the digital architectures for a multi-beam directional energy detector and a 2D FFT-based spatio-temporal energy detector, and the experimental measurements obtained using Wi-Fi sources operating at the 2.4-GHz ISM band.

6.4.1 RF receiver array setup with 16-point FFT beamformer

The 2.4 GHz 16-element patch antenna array receiver described in Chapter 3 is employed for this work as well. The RF receiver employs a 16-element super het-

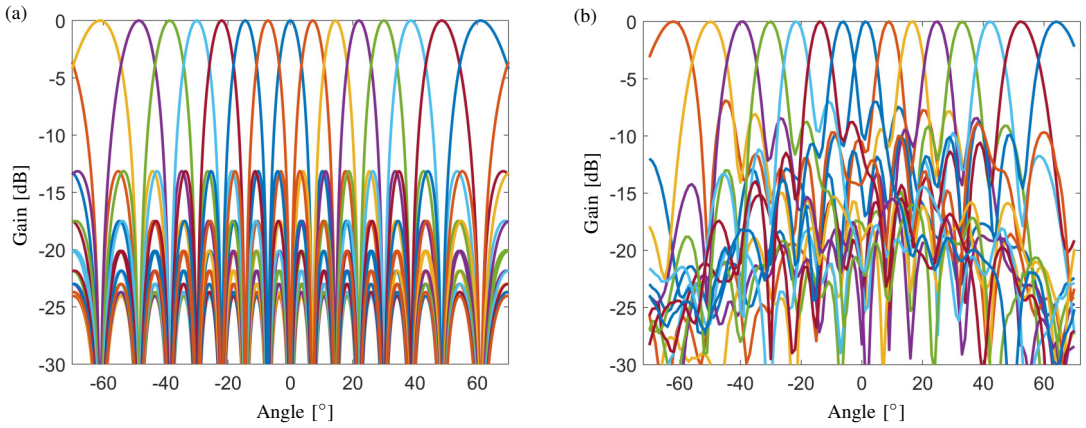

Figure 6.3: (a) Theoretical RF beams corresponding to the spatial FFT outputs; (b) the experimentally measured beams using a fixed-point implementation of the 16-point FFT.

erodyne architecture producing 16 I-Q IF outputs to be sampled by ROACH-2 ADCs. A 16-point FFT is implemented on ROACH-2 digital platform along the 16-element receiver array to form 16 simultaneous beams. Fig. 6.3(a) shows the expected theoretical RF beams. Fig. 6.3(b) shows the measured beams from experimental evaluation using an anechoic chamber, with the FPGA operated at a clock frequency of 200 MHz.

6.4.2 Multi-beam directional energy detectors

Fig. 6.4(a) shows the full system implementation of the multi-beam directional energy detectors. Here, each of the parallel multi-beam RF signals are squared, integrated, and down-sampled (standard integrate-and-dump algorithm) for measuring the receive signal power at 16 simultaneous look directions using the FFT-based multi-beam beamformer. This is a simple energy detector where the signal content and features are not considered. The only measurands are DOAs and average received energy per beam (using a sliding-window approach). This energy detector

allows the directional sensing but can not differentiate sources based on frequency, modulation type, bandwidth, or other features of the plane waves received. This work provides real-time experimental results for such "crude" RF sensing of Wi-Fi devices, operating in the 2.4-GHz ISM band, using the proposed RF multi-beam receiver.

6.4.3 Average 2D FFT-based power spectral density function

Fig. 6.4(b) shows ongoing extension to the architecture presented in the previous subsection, where temporal DFTs are employed for each of the beams obtained from the spatial-DFT based multi-beam beamformer. In fact, the 2D DFT of the antenna array output signal is computed with respect to both discrete spatial and temporal dimensions, i.e., power spectral density (PSD) function. The architecture therefore requires one spatial-FFT core for the 16 beams, and 16 more temporal FFT cores for computing the temporal DFTs. Therefore, the digital circuit area is $\times 17$ larger than that of the previous architecture, based on the FFT-core area alone. In practice, the digital complexity is even larger due to bit-growth of the system word size as the signal progresses from the 32-ADC ports and through the different FFT stages. The 2D FFT output bins correspond to an 16×8 matrix, assuming a basic 8-point temporal FFT per beam. The clock frequency of 160 MHz is chosen for the design so that each of the temporal FFT bin approximately covers a 20 MHz channel of the 2.4 GHz ISM band. The 2D FFTs are integrated in a traditional integrate-and-dump loop to improve the signal to noise ratio (SNR) under the assumption of a quasi-static condition for the incident RF plane waves. The integration of K samples of each of the 2D FFT bins leads to improve the SNR in the order of $\sqrt{K}$

because the signal is correlated and wide sense stationary additive white Gaussian noise is uncorrelated. The outputs of the integrate-and-dump circuits update at a relatively slow rate (in kHz) compared to the 160 MHz clock frequency of the system. Therefore, software registers in the ARM core in the Xilinx Virtex-6 FPGA of the ROACH-2 system can be used for update. The software registers are read into the random access memory of the host computer using a Python script. The experimental verification of the 2D FFT-based spectral measurements is reserved for future work.

6.4.4 Experimental setup

Measurements are carried out with the 2.4-GHz antenna array placed in two different situations as shown in Fig. 6.5(a). For this experimental setup, the transmitter sources are placed at 30° apart relative to the 16-element receiver array. The signals received from the array are sampled by ROACH-2 ADCs and are provided to the spatial-FFT core implemented on the ROACH-2 FPGA. The outputs of each FFT bin are then passed on to the digital integrator block for power computation. For each beam output corresponding to a spatial-FFT bin, the energy detector is configured to integrate $160,000$ temporal samples, which corresponds to 1 ms of time duration. The system is configured to produce 1000 samples of such outputs, hence the total time of energy capture is 1s.

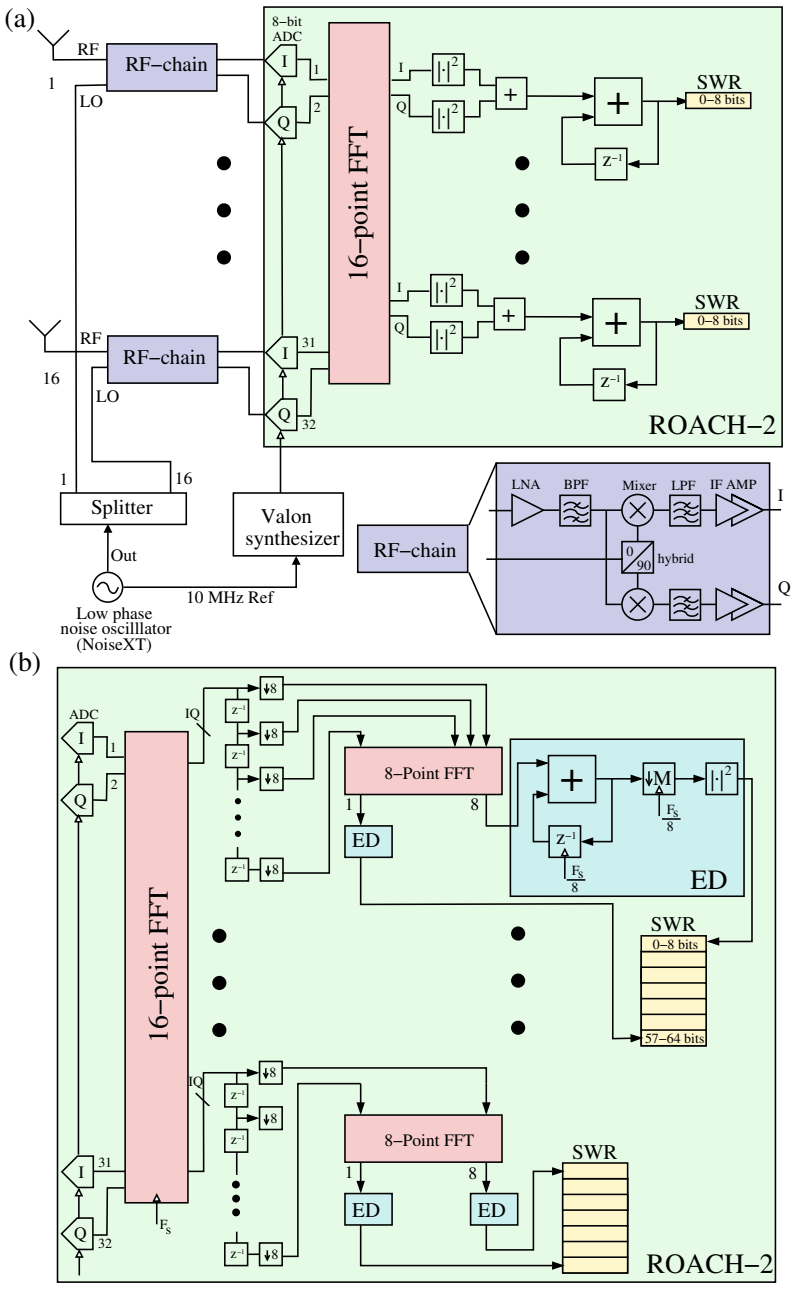

Figure 6.4: Digital architectures for directional sensing of RF sources; (a) multi-beam directional energy detector; (b) average 2D FFT-based PSD function.

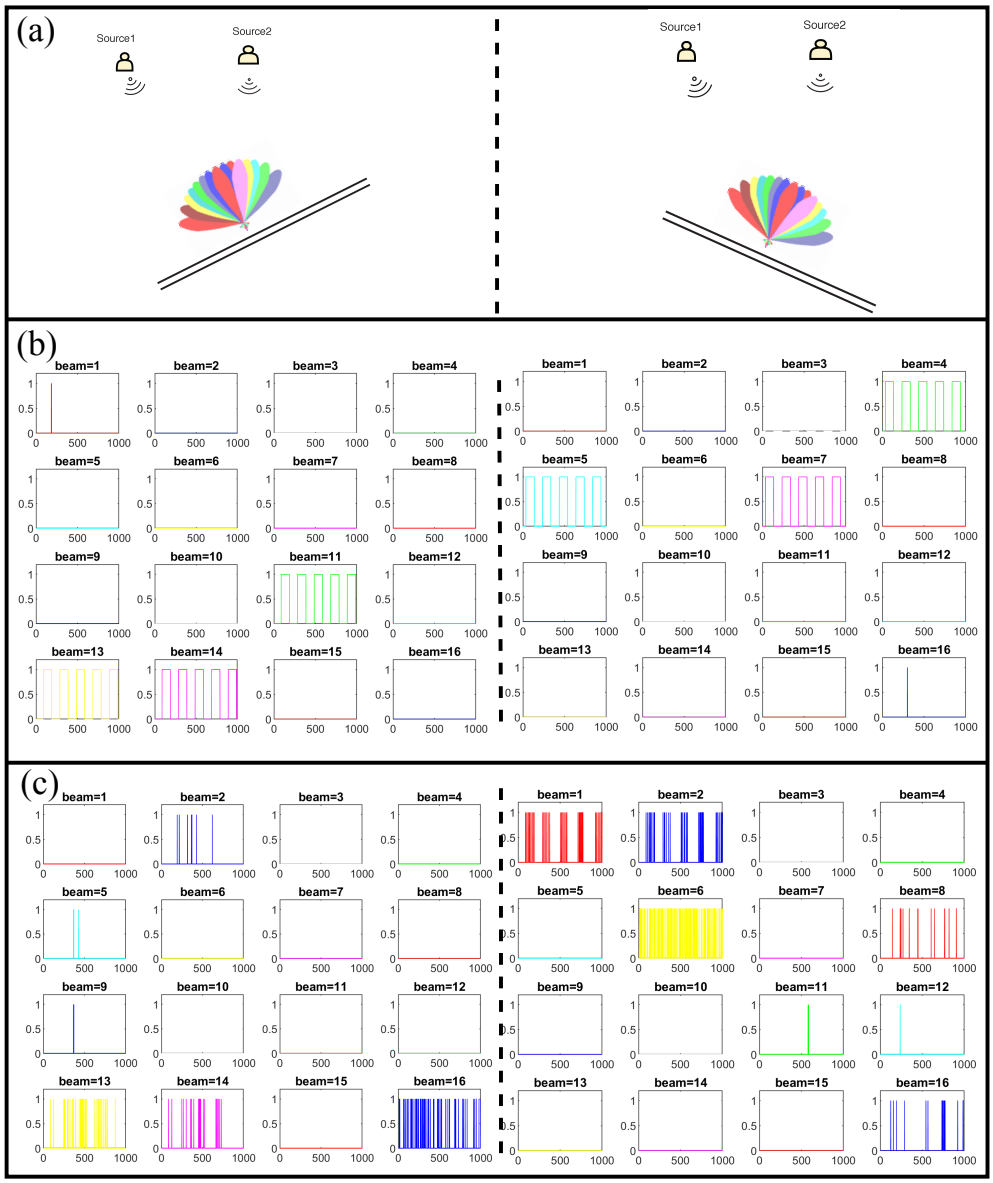

Figure 6.5: (a) Different situations in which measurements are performed; (b) measurements for the case of known RF sources; (c) real-time measurements using Wi-Fi access points. The detected energy is subjected to thresholding to make a binary decision for spectral occupancy.

6.4.5 Control experiments with known sources and directions

As a proof of the concept of the proposed directional sensor, directional sensing of known sources with fixed carrier frequencies is considered. For this, an RF signal

modulated by a 5-Hz square wave is transmitted. So, in a 1 s duration, RF signal contain 5 pulses. Fig. 6.5(b) shows the computed received energy per beam for a transmission frequency of 2.412-GHz while the LO frequency is set to 2.4-GHz. The chosen frequency corresponds to 802.11n Wi-Fi channel number 1. Our plots contain 16 windows with each window corresponding to one of the 16-bins of the FFT and specifies whether that channel is occupied or not. To specify spectral occupancy in a channel, we mapped the measured energy to either 0 or 1 with respect to a threshold. The plots in each window are color-coded that correspond to a particular beam in the 16-point FFT beamformer. The average beam separation between two beams in a FFT approach is 18° and since the two sources are 30° apart, we should expect the spectral occupancy in windows that are only one beam apart.

In scenario I, where the antenna array is oriented at $-45°$, the spectral occupancy is observed in beam 11 corresponding to source 1, and beams 13,14 corresponding to source 2. For a particular source we can expect the occupancy in two beams if it falls within the region between those two beams. However, this can be eliminated by increasing the number of beams to obtain much precise beams. Once we orient the antenna array to 45° and keep the sources at their original position, we observe spectral occupancy in beams 4,5 corresponding to source 1, and beam 4 corresponding to source 2. Thus, the beams containing energy are shifted according to the array direction verifying the performance of our directional sensor.

6.4.6 Real-world measurements

The experiment described in section 6.4.5 is repeated in an indoor environment with the presence of real Wi-Fi access points. The Wi-Fi signals are generated by continuously streaming Youtube videos and attending skype calls on a laptop. This

will generate continuous stream of data that will be enough to measure the energy occupied by our multi-beam beamformer and validate our concept. These access points are kept at 30° apart similar to source 1 and source 2, whereas the antenna array is randomly placed at a particular direction in quadrant 1 and quadrant 2 for two experimental scenarios. The integration is performed for the same time duration of 1s. The corresponding measurements are shown in Fig. 6.5(c). As expected, we observe the bins/beams that contain significant energy is shifted to the bins in one quadrant to the other, with directions corresponding to the two sources. And since the streamed data is not as pure as the transmit sources used in the fixed point sources we expect the measured energy to be non-uniform. Also, we detected energy in other random directions which we believe is due to some external Wi-Fi access points not used in our experiment. It should be noted that the case we consider here only corresponds to the antenna array placed in the two quadrants, as shown in Fig. 6.5(a), and is not exactly aligned for the case of known RF transmission and real-world measurements. Hence, this accounts for a mismatch in the results in beam directions in both cases. Through these measurements, we have thus validated our multi-beam directional sensor in real-time for 2.4 GHz Wi-Fi sources.

6.5 Conclusion

In this chapter, an FFT-based spatio-temporal RF directional sensing system is proposed for the 2.4-GHz ISM band. The objective of these systems is to exploit the concept of spatio-temporal spectral white spaces and be able to provide more opportunistic channel access in the crowded spectrum. The system consists of a 16-element patch antenna array and a FFT based multi-beam beamformer implemented on a ROACH-2 based FPGA system. The 16 I-Q channels are sampled by ROACH-2 ADCs at 160-MHz sampling rate. The incoming samples after beamforming are passed through energy detectors that employ integrate-and-dump circuits. The proposed system performs sensing over 16 look directions simultaneously and each beam output is analyzed through a temporal FFT in order to sense spectra of RF signals corresponding to each beams. Experimental measurements obtained for Wi-Fi devices with a single Wi-Fi channel verify the proof-of-concept directional sensing of the proposed system.

CHAPTER 7

DIGITAL MUTUAL COUPLING COMPENSATION USING FROST FIR FILTERS

Up until this point, we have discussed the importance of fully-digital beamforming, several ways of its implementation and further walked through one of its applications for directional sensing of RF sources. Although plethora of array factors can be realized by using fully-digital approaches, the real time performance on an array of elements is typically reduced due to the non-ideal effects present in the real-world antenna systems particularly electromagnetic mutual coupling (MC). This chapter proposes a technique for compensating electromagnetic mutual coupling (MC) effects between nearest neighbors of wideband antenna array receivers. A closed-form mathematical model for MC in uniform planar arrays (UPAs) is derived with the help of measured S-parameters across a dense set of frequencies in the bandwidth, measured LNA reflection coefficients and transmission line parameters. Mutual coupling in uniform linear arrays (ULAs) is a special case of this model. Further, we look into a wideband beamformer design that incorporates the estimated MC transer function to deembed the MC effects digitally. The design of the beamformer is formulated as a design of multi-dimensional finite impulse response filters which are optimal in the minimax sense. A wideband 7×7-element tightly coupled dipole array operating in the frequency range of 1 to 7 GHz and a 32-element patch antenna array operating in the frequency range of 5.7 to 6 GHz are employed as a UPA and a ULA, respectively, to verify the proposed MC compensation technique. The experimental setup employs ROACH-2 board featuring Virtex-6 FPGA and a Xilinx ZCU-1275 hardware platform featuring the XCZU-29DR RF SoC chip as the digital back-ends for the ULA and UPA implementations, respectively. Real-time performance with and without MC compensation is discussed further. This work

is done in collaboration with several members of RF COM research team at FIU, Dr. Chamira Eddussooriya at University of Moratuwa (Sri Lanka), Dr. Chamith Wijenayake at University of Queensland (Australia) and Dr. Leonid Belostotski at University of Calgary (Canada). The research outcomes of this work has produced one publication at IMS 2020 [129].

7.1 Background

For decades, analog beamforming has been the predominant approach and a standard in providing directional gain in wireless transceiver applications. However, fully-digital beamforming has come into limelight and is replacing the analog ways of implementing beamformers, thanks to the advanced field programmable gate arrays (FPGAs). Currently, fully-digital beamforming has its applications in radio-frequency (RF) antenna array systems, including phased-array radar, communications, space systems, positioning, and imaging [130]. Although it requires a dedicated transceiver chain for each antenna element, it offers several degrees of freedom in terms of beam flexibility, reconfigurability, simultaneous multi-beam capability when compared to analog implementations [93,131]. With significant advancements to FPGAs such as the Xilinx RF-SoCs [132] that are capable of clocking in the GHz range, wideband fully-digital beamfilters with more than two GHz bandwidth are on the verge of becoming reality. Also, the antenna engineers are coming up with designs that assume a small form factor while providing huge bandwidths, one example would be a tightly coupled dipole array [36]. But, due to smaller physical area, the mutual coupling between the antenna elements for lower frequency bands tends to be higher and directly reflects the real-time performance. Mutual coupling arises due to near field interaction of electric and magnetic fields which causes changes to element radiation patterns compared to the patterns of individual

antennas [133, 134]. For high-performance receiver arrays, it can significantly impact the stop-band performance (that is, the side-lobe (SL) level and nulls) of the receiver. Hence, the advantages of the fully-digital approaches to realize plethora of array factors is shadowed by the fact that its real-time performance is typically reduced due to the electromagnetic mutual coupling present in real-world antenna systems. In addition, other non-ideal effects such as the impedance mismatches between the antennas and the low-noise amplifiers (LNAs) across the radio band of interest cause significant deviation of the measured performance compared to theoretical best-cases developed in computer based simulations [38]. The consideration of these effects is beyond the scope of this Dissertation and is reserved for future work.

This chapter proposes a wideband Frost finite impulse response (FIR) filter [6] based digital beamformer design that de-embeds the effect of MC from the array factor leading to improved side-lobe and null performance. The proposed filter design is shown in Fig. 7.1. We start the chapter by presenting a signal processing model for 3D Frost FIR beamformer for MC compensation. A 3D spatio-temporal coupling transfer function that models the effect of MC from the measured S-parameters is derived. Next, it presents the theoretical formulations for designing a 3D complex-coefficient FIR filter, optimal in the minimax sense [135], for the beamforming back-end. The 3D MC transfer function derived earlier is incorporated into this 3D FIR filter design to de-embed the coupling effects as well as to perform beamforming. In particular, it is shown that the multi-dimensional filter design problem can be converted as a second-order cone programming problem. To the best of our knowledge, the proposed minimax design is the *first* optimization-based design technique for 3D FIR filters having complex-valued coefficients. A 2D wideband beamformer employed with uniform linear arrays (ULAs) is a special case of the proposed MC

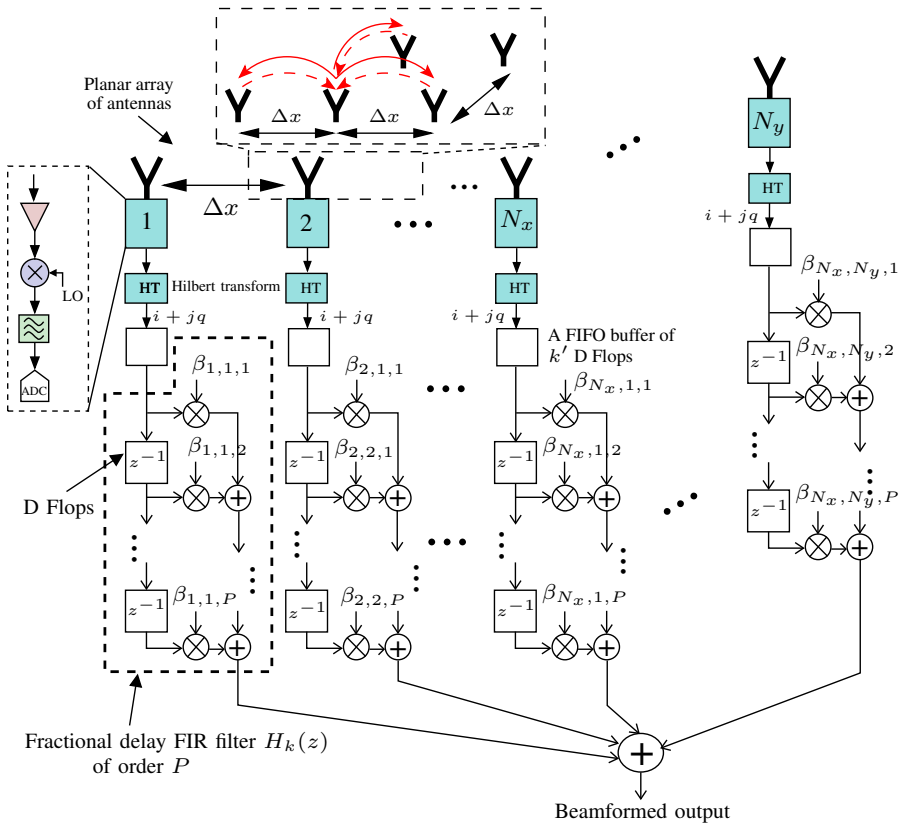

Figure 7.1: Structure of a Frost beamformer [6] implemented for a $N_x \times N_y$ UPA. The coefficients $\beta_{i,j,k}$ can be derived to realize either a true-time-delay beamformer or a more generic 3D FIR frustum filter, while taking into account the effect of MC such that the effect of MC is de-embedded in the resulting array pattern.

de-embedding technique. The proposed models are validated for the 2D case using experiments on two ULAs: a seven-element tightly-coupled dipole array (TCDA) operating in the frequency range of 1 to 7 GHz and a 32-element patch antenna array operating in the frequency range of 5.7 to 6 GHz.

7.2 Signal processing model

This section presents mathematical models for designing 3D Frost FIR beamformers with MC compensation. The Frost digital beamforming structure is a general

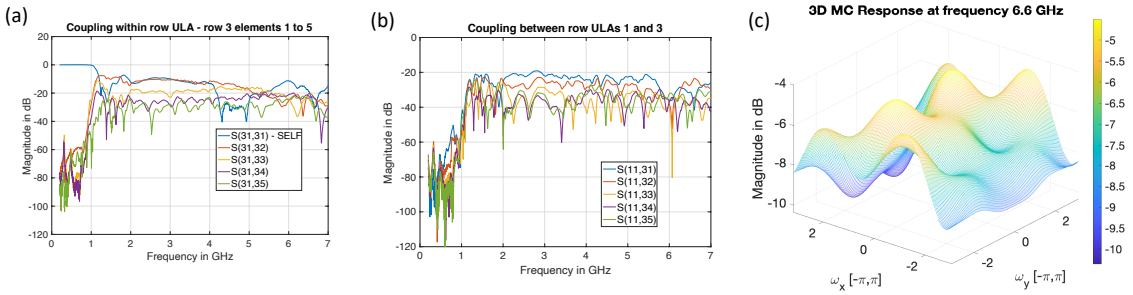

Figure 7.2: Measured S-parameters of a tightly coupled 5×5 uniform rectangular array showing (a) coupling between elements within a row ULA (b) coupling between two row ULAs. (c) Frequency response of the 3D MC transfer function in (7.1) for this TCA considering $\eta = 13$ as the reference element in the 25×25 coupling matrix $\mathbf{K}_c$.

purpose FIR filterbank that implements a filter-and-sum output between multiple receivers. The Frost structure is employed for true-time-delay wideband beamformers by employing fractional delay filters as the FIR filters. Alternatively, the Frost structure can be utilized for realizing other wideband beamforming algorithms, including adaptive beamformers (e.g., Applebaum filters), adaptive nulling filters including spatial notch filters, and 2D trapezoidal filters [48, 136]. Next, we continue with the derivation of the 3D MC transfer function that needs be incorporated into our Frost FIR filter design. This derivation and analysis of the 3D MC transfer function is performed by Dr. Chamith Wijenayake.

7.2.1 Three dimensional mutual coupling transfer function for uniform planar arrays

The effect of electromagnetic MC can be modeled via a coupling matrix, whose elements are either estimated using numerous parametric estimation methods [137] or explicitly found, using methods such as Fourier decomposition of measured element patterns [138], measured using Wheeler caps [139] or measured S-parameter based

formulations [140]. This work employs S-parameter based approach, where a vector network analyzer is employed to obtain measurements of the S-parameters between nearest neighboring elements on the array. The measured S-parameters are not directly related to beamformer behavior due to the effects of the reflection coefficient at each LNA input port, and the finite propagation delay and transmission-line effects due to the finite length transmission lines that appear between antenna ports and their corresponding LNAs. The S-parameters lead to a coupling matrix $\mathbf{K}_c$, an $(N \times N)$ square matrix, for an N-element uniform linear array (ULA). This coupling matrix can be computed in terms of the S-parameters, transmission line characteristic impedance, and LNA driving point impedance, across each antenna location in the array. As presented in [140], the coupling matrix can be used to derive a spatio-temporal coupling transfer function, which in turn can be used to de-embed the effects of mutual coupling during the beamformer design stage. This work extends the 2D spatio-temporal coupling transfer function in [140] to the 3D case corresponding to uniform planar arrays.

For a uniform rectangular array (URA) of antennas of size $N \times N$, the S-parameter matrix can be formulated as a block matrix $\mathbf{S} = (\mathbf{P_{ij}})_{N \times N}$, where each sub-matrix $\mathbf{P_{ij}}$ is of size $N \times N$. Note that, the diagonal sub-matrices $\mathbf{P}_{ij}$ for $i = j$ represent mutual coupling within each ULA row of the URA (see Fig. 7.2(a)) and the off-diagonal sub-matrices $\mathbf{P}_{ij}$ for $i \neq j$ represent mutual coupling between the rows in the URA (see Fig. 7.2(b)). Also note that, in the flattened form of this S-parameter block-matrix $\mathbf{S} = (s_{ij})_{N^2 \times N^2}$, element s_{ij} represents coupling between the antenna elements $(n_x = q, n_y = p)$ and $(n_x = n, n_y = k)$ in the URA, with the index mapping

$$i = N(p-1) + q$$

$$j = N(k-1) + n$$

where $p, k, q, n = 1, 2, ..., N$. Using the above S-parameter matrix, we can find the mutual coupling matrix $\mathbf{K}_c$ of size $N^2 \times N^2$ using the formulation given in [140] as, $\mathbf{K}_c = \mathbf{Z}_A \left(\mathbf{Z}_M + \mathbf{Z}_A\right)^{-1}$, where $\mathbf{Z}_A = Z_A \mathbf{I}_N$, $\mathbf{Z}_M = \left(\mathbf{I}_N - \mathbf{S}\right)^{-1} \left(\mathbf{I}_N + \mathbf{S}\right) \mathbf{Z}_0$, and $\mathbf{Z}_0 = Z_0 \mathbf{I}_N$, where $\mathbf{S}$ is the measured S-parameter matrix, $\mathbf{I}_N$ is the $(N^2 \times N^2)$ identity matrix, Z_0 is the characteristic impedance of the transmission line connecting the antenna to LNA and Z_A is the LNA input impedance.

We obtain $\mathbf{K}_c = \left[m_{i,j}(s_{ct})\right]_{(N^2 \times N^2)}$, where $m_{i,j}(s_{ct})$ represents the temporal frequency dependent coupling coefficients in the normalized Laplace transform domain. By extending [140, Equation 3], we can obtain the corresponding 3D spatio-temporal coupling transfer function, considering the middle antenna element in the URA as the reference, which corresponds to the reference element $m_{\eta,\eta}$, $\eta = (N^2 + 1)/2$ in $\mathbf{K}_c$ as,

$$H_C(z_x, z_y, s_{ct}) = \sum_{n_y=-n}^{n} \sum_{n_x=-n}^{n} m_{\eta,\eta-(Nn_y+n_x)}(s_{ct}) z_x^{-n_x} z_y^{-n_y}, \tag{7.1}$$

where $n > 0$ defines the URA size as $N = 2n + 1$. Here, z_x, z_y are the spatial **z**-transform variables corresponding to discrete spatial dimensions x, y (on the URA plane) respectively, and s_{ct} is the Laplace transform variable corresponding to the continuous and normalized time dimension ct. The frequency response of the above coupling transfer function can be obtained by evaluating (7.1) for $z_x = e^{j\omega_x}$, $z_y = e^{j\omega_y}$ and $s_{ct} = j\omega_{ct}$, where $-\pi < \omega_{x,y} \leq \pi$ are the spatial frequency variables and $-2\pi F_{max}/c < \omega_{ct} \leq 2\pi F_{max}/c$ is the normalized temporal frequency variable, assuming a maximum frequency of operation F_{max}, which is typically set by the bandwidth of the antennas and RF front-end. Fig. 7.2(c) shows the magnitude of the coupling frequency response for our URA of size 5×5, computed using measured S-parameters and evaluated at frequency 6.6 GHz. The effect of mutual coupling on the overall array pattern can be then obtained by computing the above 3D frequency

response in terms of spatial angles θ and ϕ (elevation and azimuth, respectively) as,

$$H_M(\theta, \phi, \omega_{ct}) = H_C(z_x = e^{j\omega_{ct}\sin\theta\cos\phi}, z_y = e^{j\omega_{ct}\sin\theta\sin\phi}, s_{ct} = j\omega_{ct}). \tag{7.2}$$

7.2.2 Frost 3D FIR beamformer

For a URA of size $N \times N$ with analog to digital conversion at each antenna, the Frost beamformer can be described in **z**-transform domain as

$$Y(z) = \sum_{p=0}^{N-1}\sum_{q=0}^{N-1} X_{p,q}(z)H_{p,q}(z), \tag{7.3}$$

where $H_{p,q}(z)$ are the 1D FIR filter transfer functions, and $X_{p,q}(z) \in \mathbb{C}$ are the z-transforms of the outputs of the digital receivers at antenna array location (p, q) on a URA of receivers. In true time delay beamforming, the filter design problem amounts to approximating a series of time delays $\tau_{p,q} = p\frac{\Delta x}{c}\sin\psi\cos\phi + q\frac{\Delta y}{c}\sin\psi\sin\phi$ in the digital domain, where c, $(\Delta x, \Delta y)$ and (ψ, ϕ) are the wave speed, inter-antenna spacing in (x, y), and beam direction, respectively. This is usually achieved by expressing the time delays in the form $\tau_{p,q} = k'T_s + \tau_f(k)$ where $0 \leq \tau_f(k) < T_s$, $k' = \lfloor \left(p\frac{\Delta x}{c}\sin\psi\cos\phi + q\frac{\Delta y}{c}\sin\psi\sin\phi\right)/cT_s \rfloor$ and where $T_s = 1/F_s$ is the temporal sampling period of the analog to digital converters clocked at frequency F_s at each antenna. The FIR filters of order P take the form $H_{p,q}(z) = \sum_{i=0}^{P-1}\beta_{p,q,i}z^{-i}$, where the coefficients are selected based on a fractional time delay interpolation scheme. The integer delays of k' sample duration is realized as first-in first-out (FIFO) buffers using clocked D-flops as shown in Fig. 7.1.

The complete Frost beamformer realized by these element delay filters $H_{p,q}(z)$ can be described by a 3D FIR filter of order $(N-1) \times (N-1) \times (P-1)$ having a suitable passband shape (typically beam or frustum shaped [44, 141–143]). The coefficients $\beta_{p,q,i}$ represent the value of the 3D filter impulse response $h(n_x, n_y, n_t)$

at $(n_x, n_y, n_t) = (p, q, i)$, where $0 \leq n_{x,y} \leq (N-1)$ and $0 \leq n_t \leq (P-1)$. Note that $h(n_x, n_y, n_t) \in \mathbb{C}^3$. In this case, the complete 3D transfer function of the filter is given by,

$$H(z_x, z_y, z_t) = \sum_{n_x=0}^{N-1} \sum_{n_y=0}^{N-1} \sum_{n_t=0}^{P-1} h(n_x, n_y, n_t) z_x^{-n_x} z_y^{-n_y} z_t^{-n_t}. \tag{7.4}$$

In the next section, we present how to design this 3D filter using numerical optimization techniques, while taking into account the previously derived 3D coupling transfer function. This mathematical analyis is done by Dr. Chamira Edussooriya, and the design of the complex-coefficient FIR filter was done by his student, Ashira Jayaweera at University of Moratuwa, Srilanka.

7.2.3 Frequency-dependent array factor

Considering the outputs $X_{p,q}(z)$ of the digital receivers at each antenna, the directional 3D input of the URA can be expressed as

$$X(\theta, \phi, \omega) = X_k(e^{j\omega}) e^{-j\omega(p \sin\theta \cos\phi + q \sin\theta \sin\phi)}, \tag{7.5}$$

where θ and ϕ are elevation and azimuth angles respectively, and $\omega < 2\pi F_s/2$ is the normalized (radian) frequency. The array output in the 3D angular-frequency domain is therefore given by $Y(\theta, \phi, \omega) = X(\theta, \phi, \omega) H_T(\theta, \phi, \omega)$, where $H_T(\theta, \phi, \omega)$ denotes the total array pattern of the directional receiver, which, following the principle of pattern multiplication, is given by $H_T(\theta, \phi, \omega) = H_E(\theta, \phi, \omega) H_A(\theta, \phi, \omega) H_M(\theta, \phi, \omega)$, where $H_E(\theta, \phi, \omega)$ is the element radiation pattern of a signal antenna in isolation, $H_A(\theta, \phi, \omega)$ is the array factor produced by the 3D Frost beamformer, and $H_M(\theta, \phi, \omega)$ represents distortions in the array pattern caused by the effect of MC

as given by (7.2). Here, the array factor of the Frost beamformer is given by

$$\begin{aligned} H_A(\theta,\phi,\omega) &= \sum_{p=0}^{N-1}\sum_{q=0}^{N-1} H_{p,q}(e^{j\omega})e^{-j\omega(p\sin\theta\cos\phi+q\sin\theta\sin\phi)} \\ &= \sum_{p=0}^{N-1}\sum_{q=0}^{N-1}\sum_{i=0}^{P-1} \beta_{p,q,i}e^{-j\omega(p\sin\theta\cos\phi+q\sin\theta\sin\phi+i)} \end{aligned} \tag{7.6}$$

having the magnitude response $\rho(\theta,\phi,\omega) = \|H_A(\theta,\phi,\omega)\|$.

7.2.4 Proposed design with compensation of MC

The MC on the URA produces a 3D coupling transfer function $H_M(\theta,\phi,\omega)$ that is both angle and frequency dependent. The presence of MC modifies the input signal from the array such that if the original input signal is $X(\theta,\phi,\omega)$ the signal that is practically available at the output of the URA is $X(\theta,\phi,\omega)H_M(\theta,\phi,\omega)$. This coupling function modifies the beamformer array factor to $H_A(\theta,\phi,\omega)H_M(\theta,\phi,\omega)$. Therefore, we propose that the FIR filters in the beamformer be modified using an MC compensation function $\frac{1}{\|H_M(\theta,\phi,\omega)\|+\epsilon}$, where $\epsilon > 0$ is a small real-valued constant chosen to avoid division by zero at the zeros of $H_M(\theta,\phi,\omega)$ yielding the required form

$$\begin{aligned} \rho_{new}(\theta,\phi,\omega) &= \|H_M(\theta,\phi,\omega)\| \cdot \left\| \sum_{p=0}^{N-1}\sum_{q=0}^{N-1} \frac{H_{p,q}(e^{j\omega})e^{-j\omega(p\sin\theta\cos\phi+q\sin\theta\sin\phi)}}{\|H_M(\theta,\phi,\omega)\|+\epsilon} \right\| \\ &\approx \rho(\theta,\phi,\omega) \end{aligned}$$

Small ϵ limits the depth of array factor nulls to $-10\log_{10}\epsilon^2$. Typical values around $\epsilon = 0.01$ leads to nulls that do not go down below -40 dB after compensation of MC. Next, we look into the design of complex-coefficient FIR filter using optimization techniques.

7.3 Design of complex-coefficient FIR filters

The 3D FIR filter design is formulated as a convex optimization problem [144, ch. 14.7]. To this end, we first write the array factor $H_A(\theta, \phi, \omega)$ of the 3D beamformer filter as

$$H_A(\theta, \phi, \omega) = \sum_{n_x=0}^{N_x-1} \sum_{n_y=0}^{N_y-1} \sum_{n=0}^{P-1} h(n_x, n_y, n) \times e^{-j[\omega \sin(\theta)\cos(\phi) n_x + \omega \sin(\theta)\sin(\phi) n_y + \omega n]}. \tag{7.7}$$

Note that the order of the 3D beamformer filter is $N_x \times N_y \times P$, which corresponds to a UPA having $N_x \times N_y$ antenna elements, and each signal of these antenna elements is temporally processed by a P-tap filter. Here, $h(n_x, n_y, n)$ denotes the complex-valued coefficient (i.e., weight) of the 3D beamformer, corresponding to the n-th tap of the (n_x, n_y) antenna element. For brevity and to comply with the standard notation of 3D filters [145, ch. 3], we denote $\omega \sin(\theta)\cos(\phi)$ and $\omega \sin(\theta)\sin(\phi)$ as ω_x and ω_y, respectively. Then, we express the $H_A(\theta, \phi, \omega)$ as a frequency response of a 3D FIR filter with the standard notation [145, ch. 3] as

$$\begin{aligned} H(e^{j\boldsymbol{\omega}}) &= H_A(\theta, \phi, \omega) \\ &= \sum_{n_x=0}^{N_x-1} \sum_{n_y=0}^{N_y-1} \sum_{n=0}^{P-1} h(n_x, n_y, n) e^{-j[\omega_x n_x + \omega_y n_y + \omega n]}, \end{aligned}$$

where $\boldsymbol{\omega} = (\omega_x, \omega_y, \omega) \in \mathcal{F}$ and $\mathcal{F} = \{\boldsymbol{\omega} \in \mathbb{R}^3 \mid -\pi \leq \omega_x, \omega_y, \omega < \pi\}$).

In order to achieve approximately equal SL levels, the optimal design, i.e., the impulse response $h(n_x, n_y, n_{ct})$, is obtained with respect to l_∞ norm (called the minimax design). This convex optimization problem can be converted to a second-order cone programming problem, which can be efficiently solved using optimization toolboxes with MATLAB. To avoid the intensive mathematical analysis, the problem formulation is not presented here, and the reader is referred to [135] for a formulation

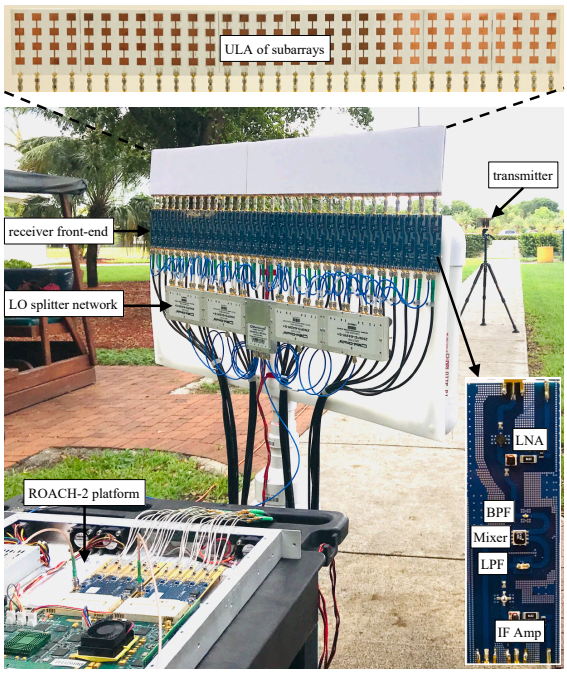

Figure 7.3: The 5.8-GHz 32-element antenna array setup used for experimentally verifying the 2D case of the proposed MC compensated Frost beamformer.

of minimax design of the 3D FIR filters. The design of 2D FIR filters is a special case of the proposed design method. In order to design a 2D FIR filter of order $N_x \times P$ that corresponds to a ULA having N_x antennas, we can use the same design procedure, however, with $N_y = 1$ and $\phi = 0°$. In this case, $\omega_y = 0$ and $H(e^{j\boldsymbol{\omega}})$ in (7.8) reduces to the frequency response of a 2D FIR filter. In the next section, we cover the implementation of the proposed FIR MC compensated Frost beamformer for a 2D case.

7.4 Experimental validation of 2D FIR MC compensated beamformer

The antenna array and the RF front-end is described in the next subsection.

7.4.1 Receiver array setup

The antenna array consists of 32-element ULA where each element is a 4-element vertical subarray that provides an enhanced gain in the elevation pattern. The horizontal spacing of the antenna array has been set to 31 mm. As shown in Fig. 7.1, the front-end includes a single mixer-based receiver architecture. Each RF chain employs the following components in sequence- low noise amplifier (LNA) $\rightarrow$ bandpass filter (BPF) $\rightarrow$ mixer $\rightarrow$ lowpass filter (LPF) $\rightarrow$ IF Amplifier. The receiver chains are fabricated on FR-4 PCB using the surface-mount devices corresponding to the RF components. The LNA (LEE-39) being the crucial component to dictate the cascade noise figure provides a low noise figure of 2.4 dB with 16 dB Gain. A centralized LO is developed for all 32 elements using commercial-off-the-shelf power splitters (ZN2PD-63-S). Mixer (SIM-83-LH) downconverts the incoming amplified-and-bandpass-filtered signals using the common LO signal. All 32 IF channels are sampled in the ROACH-2 platform using two ADC16x250-8 analog-to-digital converter (ADC) cards, where each card supports 16 analog channels at a rate of 240 MSps. An FIR filter based implementation of the Hilbert transform is used to obtain the in-phase and quadrature-phase (I-Q) channels for each sampled IF channel. The I-Q digital streams of each channel are then used for calibrating each receiver channel to get rid of gain and phase mismatches by using a complex multiplier in the data path. This 5.8-GHz 32-element array receiver has been a collective work of several members from The University of Akron. The antenna design and selection of components was done by Suresh Madishetty. The development of layouts for the PCB design and construction of the array receiver is done in collaboration with Suresh and Dr. Viduneth. This array has been utilized in many of our previous works to implement multi-beam beamformers [131,146]. The complete details of the array design can be found in [147].

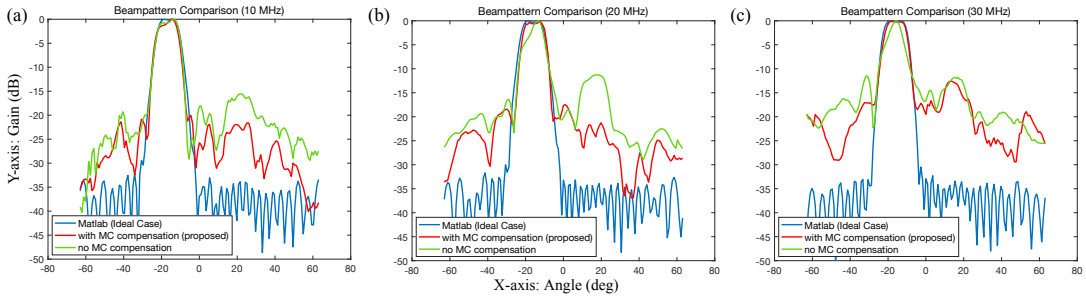

Figure 7.4: Measured beam patterns in comparison with the ideal beam patterns for cases (a) 10-MHz IF signal; (b) 20-MHz IF signal; (c) 30-MHz IF signal for the 5.8-GHz 32-array 2D FIR filter implementation.

7.4.2 Experimental setup and beam measurements

The 2D FIR trapezoidal filter is realized at a bandwidth of ±30 MHz centered at 5.86-GHz. The number of antennas and dedicated receivers (i.e., N) is 32, see Fig. 7.3. 2D FIR trapezoidal filters with and without the proposed MC compensation are implemented and tested in real-time to evaluate the relative improvements of SL levels (i.e., directional beam selectivity as a function of frequency across the 30 MHz band of interest). Fig. 7.4 shows measured beam patterns obtained for three different IFs where the center frequency was fixed at 5.8-GHz. The IFs were selected at 10-MHz, 20-MHz, and 30-MHz, with a digital clock frequency (same as ADC sample frequency) of 160 MHz. The transmitter was a horn antenna (gain 13 dBi) placed in the array plane at a distance of 6.3 m.

7.4.3 Limitations

The presence of 32 elements requires a relatively large area for experiments because the near field region now extends to about 700λ. The use of a fully anechoic antenna test chamber of such dimensions is prohibitively expensive for the authors; therefore, a large underground parking garage was used for conducting the experiments. The

Table 7.1: SL Level Reductions Achieved with the Proposed Approach

Parameter (dB)	IF		
	10 MHz	20 MHz	30 MHz
Reduction of worst-case SL level	7.5	11.2	5.6
Reduction of average SL level	5.1	5.2	2.1
Maximum reduction of SL level	12.1	13.5	11.7

garage was clear of obstacles within four meters height but there exists metal piping close to the ceiling which causes some strong reflections. The concrete ceiling and tarred floor of the building are also expected to contribute to strong multipath reflections which prevents more accurate measurement of SLs and directional nulls.

7.4.4 Discussion

This section described real-time antenna, microwave and digital signal processing systems for implementing digital Frost beamforming receivers across up to 32 antenna elements on a ULA. The 5.8-GHz realization supports up to 100-MHz of bandwidth but non-ideal effects in the antenna array and microwave circuitry limits its performance compared to theoretical best-case of the digital beamformers. The reflections in the measurement chamber further degrades measurement of the deep SLs. However, we demonstrate that measured S-parameters from the antenna array can lead to optimized digital circuit designs that de-embed the MC effects between elements up to the first order, thereby allowing reduced SLs compared to direct implementation of a given digital beamformer. The improvements in SL performance by the proposed approach is shown in Table 7.1 for the 30-MHz band. We observe 5.2 dB and 13.5 dB reductions in the average SL level and the worst-case SL level, respectively, at an IF of 20-MHz. Furthermore, more than 11.7 dB maximum reduction of SL levels are achieved for the 30-MHz band.

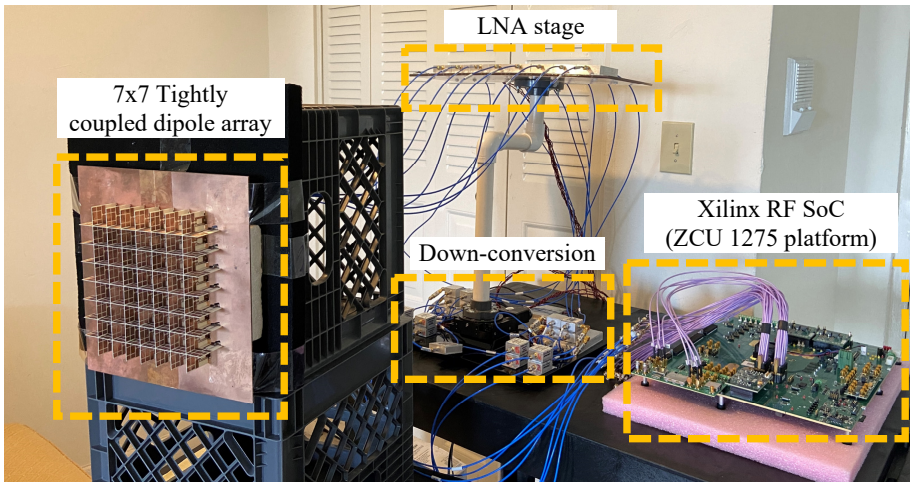

Figure 7.5: Setup for TCDA array measurements. A seven-element ULA (part of the 7×7 TCDA) was connected to broadband receivers (1-6 GHz).

7.5 Experimental validation of 3D FIR MC compensated beamformer

To demonstrate the real-time functionality of the proposed approach for a 3D case, a tightly-coupled dipole array (TCDA) based seven-element fully digital receiver array shown in Fig. 7.5 is employed. This version of the TCA is designed by Dr. Alexander Johnson of the RFCOM lab at FIU. Dr. John Volakis, Dr. Satheesh Venkatakrishnan, Dr. Elias Alwan are few among others from this lab who have worked on TCA's in the past and am grateful for their contribution for this work. The following sections describe the details of the hardware setup that include the antenna array design, RF chains design and the digital hardware platform.

7.5.1 Antenna array design

A low profile and wideband performance is key to the operation of modern active electronically scanned arrays (AESAs). An ultra-wideband (UWB) array replaces

several narrowband antennas to reduce the space, weight, power, and cost (SWaP-C) requirements in digitally controlled arrays. These multi-functional arrays also require high isolation and polarization purity to enable polarization dependent communications and simultaneous transmit and receive (STaR) capabilities [148]. Additionally, such arrays must maintain these features across a wide angle scanning range for comprehensive spatial coverage.

UWB phased arrays are often hindered by their size, bandwidth, and efficiencies. For example, Vivaldi or tapered slot arrays are known for their large (10:1) impedance bandwidths, but are multiple wavelengths tall [149] ($> 3\lambda_{High}$) and show high cross-polarized (X-pol) gains in the diagonal planes. As an alternative to Vivaldi, Tightly Coupled Dipole Arrays (TCDA) have demonstrated large impedance bandwidths and scanning performance with lower cross-polarized gain levels and lower profiles on the order of $\lambda_{High}/2$. Recent TCDAs have demonstrated UWB performance by increasing the capacitive coupling between antenna elements and introducing integrated wideband printed feed networks [36,150–153] to control impedance matching. Further optimization of TCDAs have extended impedance bandwidths to 50:1 via substrate loading [151, 154] and scanning down to 70° using Frequency Selective Surface (FSS) superstrates [152, 153].

The TCDA design in Fig. 7.6(left) employs two independent linear polarizations using an egg-crate arrangement. This array uses a microstrip configuration, on a single 0.5 mm (20 mil) Rogers 4003 substrate to achieve a low-cost UWB TCDA. The UWB and low-angle scanning performance is achieved through a Marchand balun and metal FSS superstrate following the design considerations in [36, 152]. The balun consists of a series open stub (Z_{oc}) and a parallel short stub (Z_{sc}), whose lengths and characteristic impedances are tuned to achieve wideband matching and common-mode cancellation. The FSS superstrate consists of sub-wavelength metal-

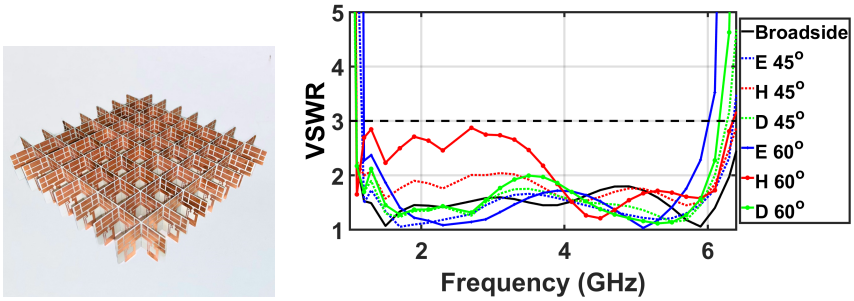

Figure 7.6: Fabricated dual polarized microstrip TCDA (left) with infinite array active VSWR (right), showing VSWR <3 scanning down to 60° in the principle (E/H) and diagonal (D) planes.

lic rectangles printed above the dipoles, which produce an effective dielectric constant (ϵ_{eff}) and replace thick and heavy dielectric slabs as free space matching layers.

Initially, an infinite array simulation was used to represent the 8 × 8 finite element array using ANSYS HFSS v.19. The infinite array VSWR in the principle planes, with scanning to 60° is given in Fig. 7.6(right). As seen, the array provides a VSWR < 2 across 1.05-6.3 GHz at broadside and VSWR <3 in all planes when scanning down to 60°. Notably, it is difficult to maintain low reflection impedance matching across an UWB when scanning in the H-plane [150]. The trade-off between impedance bandwidth and maximum mismatch comes from a high reactance seen when scanning in the H-plane [155], which can be difficult to control over a very wideband without significant increases in height and complexity.

7.5.2 Receiver chain and digital back-end

Due to resource limitations, a ULA of seven elements (center row) part of the 7×7 TCDA planar array, is considered for the prototype work. The seven-element ULA is connected to broadband receiver chains employing a single mixer direct down-

conversion architecture, and built using commercial-off-the-shelf components. Each antenna under consideration is connected to a LNA (*Minicircuits-ZRL2400LN+*) that provides 30 dB of gain and a low noise figure within the frequency range 1-2.4 GHz. The signals are then routed to a downconversion stage that includes Mixer (*Minicircuits-ZFM15S+*) and LPF (*Minicircuits-VLF-1450+*) for bringing down the RF to baseband. This downconversion stage support upto 1.5 GHz of bandwidth. To provide a common local oscillator signal for all the mixers, a centralized LO stage is built using the power splitters (*ZN-2PD-63-S+*). A external RF frequency synthesizer is connected to this centralized LO stage to provide eight LO signals. Post downconversion, the baseband signals are passed on to the digital back-end.

The Xilinx ZCU-1275 hardware platform board is used as the digital back-end for this work as well. The calibration of the RF chains was performed digitally. For this, an RF source placed in the far-field region of the ULA transmits a desired signal onto it's broadside, and from the ADC samples captured from each receiver chain, we computed the gain and phase mismatches. A digital complex multiplier is employed to compensate for these mismatches while taking real-time beam-filter measurements.

7.5.3 Measurement setup and beam measurements

Figure 7.7 shows the overall system architecture of the measurement setup. For beam measurements, the angle of arrival is emulated by rotating the TCDA array using a rotation platform while keeping the transmitter fixed. The transmitter is a Vivaldi antenna operating in the frequency range of 1 to 3 GHz and is at a distance of $4m$ from the receiver array. The digital back-end interfaced to Xilinx Vivado software collects the ADC samples for desired degrees of interest, and a MATLAB

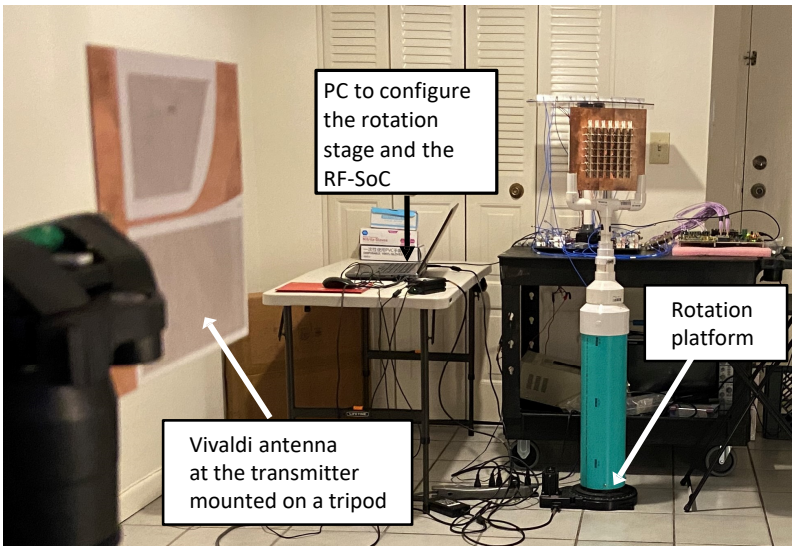

Figure 7.7: Experimental setup for measuring the filter beam-patterns using the TCDA array.

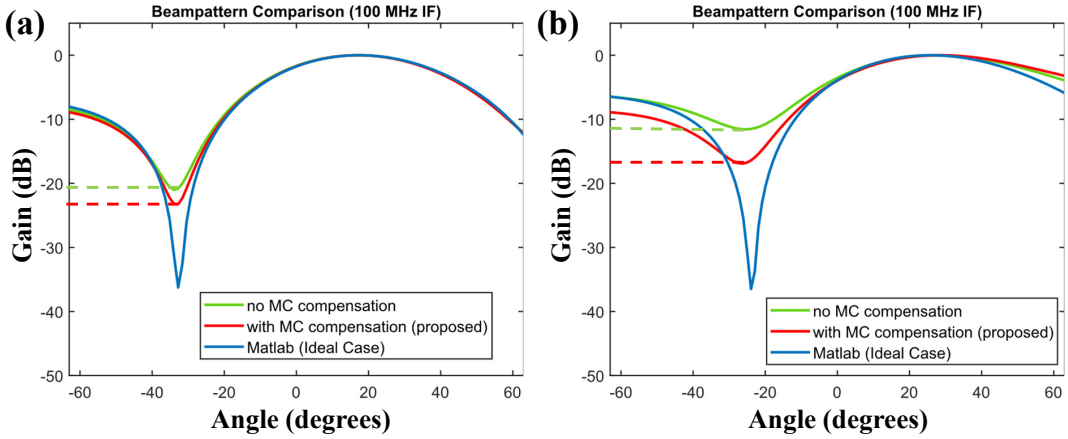

Figure 7.8: Measured beam patterns in comparison with the ideal beam patterns for (a) IF = 100-MHZ, Scanning angle=−10 degrees; (b) IF=100-MHZ, Scanning angle= −20 degrees.

simulation is set up to post-process the captured data. The post-processing includes the calibration, filtering and beam plotting.

The beam measurements are carried out for 100-MHz IF frequency generated from a 1.9-GHz transmitter signal and a 2-GHz LO signal. The ZCU-1275 RF-SoC ADCs are clocked at 1966-MHz to digitize the 100-MHz IF signal. A 3D FIR MC

compensate beamformer is designed for 10 and 20 degrees of arrival. Fig. 7.7 shows the comparison of the three curves: measured beam patterns using the original filter (without MC compensation), measured pattern using the MC compensation beamformer, and the ideal beam patterns that doesn't incorporate the channel and microwave non-ideal effects. The simulated responses are generated in Matlab from the 2D frequency response of the original filter (filter without MC compensation) in closed form. It should be noted that the antenna array has a inter-element spacing of 0.5λ at 6-GHz (25 mm), and as we picked 1.9-GHz frequency for measurement, this comes under a spatially oversampled case. The generated beam patterns will be broadened along the desired range of angles, and thus contain less number of side lobes. Hence, we evaluated our performance in terms of the nulls in the pattern.

From the measurements in 7.8, it can be observed that the beam positions are very well in agreement for all curves in both cases. Whereas, the nulls of the original filter without MC compensation are deepened and improved by 2.4 dB for 10 degrees and 5.2 dB for 20 degrees by employing the proposed MC compensated filter, thus validating our proposed work for these preliminary measurements.

7.5.4 Limitations

The measurements were taken in an indoor apartment environment for the frequencies ranging between 1.2 and 2 GHz, a band that is prone to strong interference. Due to this, the received signal power at the antenna array was at the same level as the interference even while using the highest power level permitted for ISM commercial applications. We expect that the MC filter performance can be further improved if the measurements were carried out in an anechoic chamber or an outdoor environment free from interference.

7.6 Contribution and comparison to previous work

This chapter discussed compensation of mutual coupling in antenna arrays; a non-ideality that greatly affects the antenna array's beam performance especially for wideband, highly sensitive applications. Prior methods on reduction of MC include modification to antenna structures using EBG structures [156], using special structures like parallel coupled-line resonators [157] or using low-scattering antennas [39]. The above techniques are implemented at the analog-level and lack the ability of adaptation, so we look into digital techniques where the MC is modeled as a matrix. The effect of mutual coupling is typically modeled by a coupling matrix [138], whose elements are either estimated using numerous parametric estimation methods [134, 137, 158] or explicitly found, using methods such as Fourier decomposition of measured element patterns [138,159] or measured scattering (S-) parameter based formulations [140, 159]. In this work, we employ S-parameter based approach which is the simplest of all the mentioned methods.

The proposed method is a novel digital MC compensation technique where the MC coupling transfer function is embedded into Frost FIR-filter based digital beamformer to provide beams in the desired direction while improving the side-lobe and null performance. This approach is well suited for wideband applications and possess all advantages available for a digital beamformer. The filter co-efficients are adaptive and can be reconfigured to optimize the array performance when desired. In this work, we have validated our proposed technique for the 2D case using experiments on two ULAs: a seven-element TCDA array operating in the frequency range of 1 to 7 GHz and a 32-element patch antenna array in the frequency range of 5.7 to 6 GHz. The measured beams with and without mutual coupling compensation technique are presented for various IF frequencies (upto 30 MHz bandwidth) which

convey the improvement in side-lobe levels as well as null performance, using the proposed method.

7.7 Conclusion

A mutual coupling transfer function is designed with a technique based on measured S-parameters that attempts to de-embed and uncouple the antenna arrays. The MC transfer function when integrated to the beamformer design improves the side-lobe levels and null performance of the array patterns that are originally distorted due to the MC. 3D and 2D Frost based FIR beamfilters that compensate these MC effects are developed to validate the proposed technique for UPA and ULAs. For a 2D FIR Frost beamformer implementation with MC compensation employing a 32-element patch antenna array $(5.6 - 6)$ GHz, $>$ 5 dB (average) SL level reduction can be achieved having 20-MHz bandwidth. For the 3D case, preliminary measurements were taken for the central row of the 7×7 wideband TCDA array (1-6 GHz), and the experimental results indicated a 5.2 dB null performance improvement for 100-MHz bandwidth using the proposed technique.

CHAPTER 8

DIGITAL MUTUAL COUPLING COMPENSATION USING FAST ALGORITHMS

In the previous chapter, we have looked at one of the approaches used for mutual coupling (MC) compensation. It is a Frost FIR filter based architecture [6] and utilizes convex optimization techniques with minimax design analysis to de-embed the effect of MC. One disadvantage in such filters is the digital complexity associated with Frost architectures. Hence, in this chapter we look into another approach based on fast-algorithms and has lower digital complexity compared to the Frost FIR based approach. The proposed approach is a fast, low-complexity, real-time capable algorithm that will furnish the uncoupling of mutually coupled elements in the digital signal processing back-end. It aims at realizing the inverse of Mutual coupling matrix by using a fast inversion algorithm for tridiagonal Toeplitz matrices. An eight-element 5.8-GHz array receiver with a ROACH-2 based digital hardware platform is realized to verify this proposal. This work is done in collaboration with Dr. Sirani Perera at Daytona College of Arts and Sciences and Dr. Chamith Wijenayake at University of Queensland, Australia. Dr. Wijenayake generated the MC coupling matrix from the measured S-parameters. Dr. Perera proposed and derived the mathematical proofs for the fast-algorithms discussed in this chapter.

8.1 Background

In an array configuration, electro-magnetic mutual coupling (MC) between antenna elements is always present. MC arises due to near field interaction of electric and magnetic fields and cause distortions to element radiation patterns of individual antennas and subsequent array processing [138, 159, 160]. Such distortions are untolerable for high performance receivers. Coupling is a function of array geometry

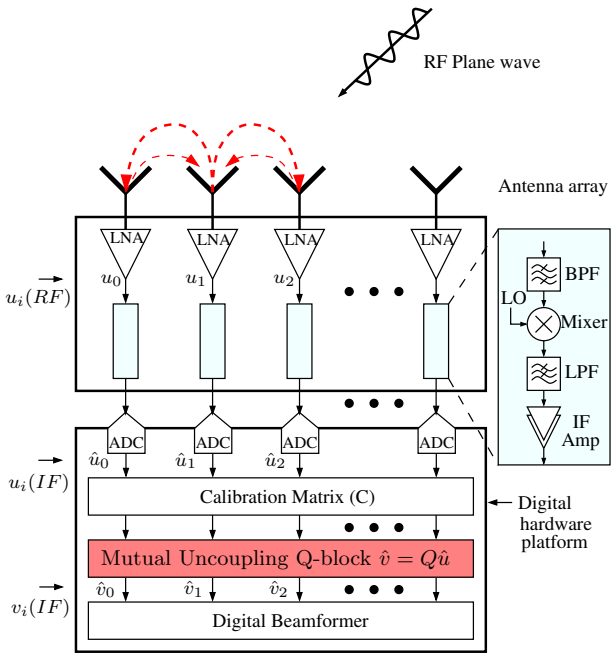

Figure 8.1: Overview of the proposed real time mutual uncoupling architecture.

and inter-element spacing and because electromagnetic fields attenuate with distance from an antenna, for a given antenna element, the effect of MC is dominant across its few nearest neighbors. Measurements confirm coupling is negligibly small for antenna arrays where the inter-element spacing is more than a wavelength [134]. This chapter proposes a fast algorithm implemented on a digital hardware back-end suitable for real-time digital uncoupling of mutually coupled arrays. A low order coupling function where each antenna is coupled only to its two nearest neighbors is considered. The proposed method can nevertheless be extended to higher order coupling albeit at increased system complexity. The system overview of the proposed MC compensation technique is shown in Fig. 8.1. We start with modeling the MC effects by a coupling matrix whose elements are the measured S-parameters. This is demonstrated in previous chapter but we revisit this theory briefly to understand the concepts from the perspective of the fast-algorithm approach.

8.2 Structured coupling matrix

As described in Chapter 7, the effect of mutual coupling is typically modeled by a coupling matrix [138], whose elements are either estimated using numerous parametric estimation methods [134, 137, 158] or explicitly found, using methods such as Fourier decomposition of measured element patterns [138, 159] or measured scattering (S-) parameter based formulations [140, 159]. This work employs S-parameter based approach, and for simplicity, narrowband operation at a particular frequency is assumed. Hence, the S-parameters only need to be measured at the frequency of interest. The S-parameters are not directly related to beamformer behavior due to the effects of the reflection coefficient at the LNA input port, and the finite propagation delay and transmission-line effects. The S-parameters lead to so-called coupling matrix $\mathbf{K}_c$, which is an $(N \times N)$ square matrix, for an N-element uniform linear array, and computed in terms of the S-parameters, transmission line characteristic impedance, and LNA impedance, across each antenna location in the array. Following [140, Sec. II-A], the coupling matrix can be computed as $\mathbf{K}_c = \mathbf{Z}_A \left(\mathbf{Z}_M + \mathbf{Z}_A\right)^{-1}$, where $\mathbf{Z}_A = Z_A \mathbf{I}_N$, $\mathbf{Z}_M = \left(\mathbf{I}_N - \mathbf{S}\right)^{-1} \left(\mathbf{I}_N + \mathbf{S}\right) \mathbf{Z}_0$, and $\mathbf{Z}_0 = Z_0 \mathbf{I}_N$, where $\mathbf{S}$ is the measured S-parameter matrix, $\mathbf{I}_N$ is the $(N \times N)$ identity matrix, Z_0 is the characteristic impedance of the transmission line connecting the antenna to LNA and Z_A is the input impedance. Dr. Wijenayake at University of Queensland has collaborated in this work by generating the MC coupling matrix from the measured S-parameters.

8.2.1 Structural properties of the coupling matrix

Consider a normalized mutual coupling between P nearest neighbors of a uniform linear array of N elements. The coupling matrix $\mathbf{K}_c = \left(k_{m,n}\right)_{N \times N}$ takes an $(P+1)$-

diagonal form, where the elements $k_{m,n}$ for $1 \leq m, n \leq N$ are of the form,

$$k_{m,n} = \begin{cases} a & \text{if} m = n \\ b_k & \text{if } |m-n| \leq P/2 \\ 0 & \text{if } |m-n| > P/2 \end{cases}$$

Here, the diagonal coefficients $a = \alpha e^{-j\theta} \in \mathbb{C}$ correspond to self-coupling and the P off-diagonal coefficients $b_k \in \mathbb{C}$, $k = 1, 2, ..., P$ correspond to mutual coupling from the P neighboring elements, and $\alpha \leq 1$, $\|b_k\| \leq 1$ due to passivity, and $\|b_k\| < \|b_{k+1}\|$, $k \leq P-1$ because mutual coupling reduces monotonically with distance from the antenna to its neighbors. The coefficient α captures the effect of the reflection coefficient at the LNA combined with the antenna impedance, transmission line characteristic impedance, and transmission line length, while the phase lag θ corresponds to the phase at the driving point of the LNA transformed due to finite transmission line length (i.e., time delay) [161]. The mutual coupling matrix $\mathbf{K}_c$ embeds the frequency-dependent behavior of the measured electromagnetic effects between elements, antenna driving point impedance function, characteristic impedance of the transmission lines, and frequency dependent behavior of the LNA driving point impedance, in one convenient matrix of complex coefficients. For simplicity (also validated by our measurements), we assume that coupling is dominant across two neighbors (i.e., $P = 2$), leading to a tridiagonal coupling matrix for an $N = 8$ element array, of the form,

$$\mathbf{K_c} = \begin{bmatrix} a & b_1 & 0 & 0 & 0 & 0 & 0 & 0 \\ b_1 & a & b_1 & 0 & 0 & 0 & 0 & 0 \\ 0 & b_1 & a & b_1 & 0 & 0 & 0 & 0 \\ 0 & 0 & b_1 & a & b_1 & 0 & 0 & 0 \\ 0 & 0 & 0 & b_1 & a & b_1 & 0 & 0 \\ 0 & 0 & 0 & 0 & b_1 & a & b_1 & 0 \\ 0 & 0 & 0 & 0 & 0 & b_1 & a & b_1 \\ 0 & 0 & 0 & 0 & 0 & 0 & b_1 & a \end{bmatrix}_{8\times 8}$$

It is well-known that such tri-diagonal matrices are non-singular provided $a \neq 0$ which is *always satisfied physically in an array processing system.* Hence, the inverse of the coupling matrix exists and can be denoted as $\mathbf{Q} = \mathbf{K_c}^{-1}$.

8.3 Uncoupling the mutual coupling

The existence of $\mathbf{Q}$ is of significance because it is possible to digitally "undo" the physical coupling of fields by multiplying the array outputs by the matrix $\mathbf{Q}$ at each time step. The coupling is a spatial linear matrix operation, which therefore, can be reversed (i.e., uncoupled) in the digital signal processor (DSP) using a brute-force matrix vector multiplication at every time step. Interestingly, the spatial nature

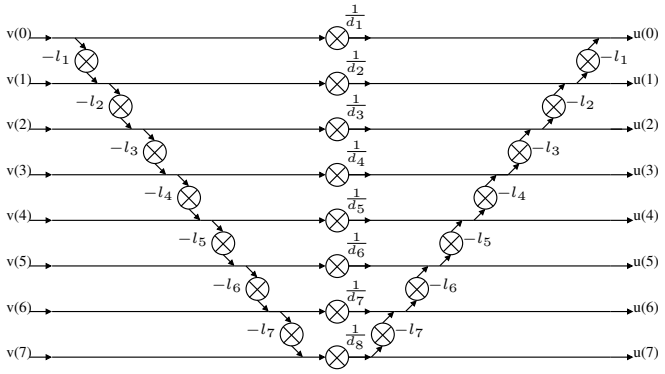

Figure 8.2: The signal flow graph corresponding to $N = 8$.

of the operation allows uncoupling operations to be conducted at intermediate frequency (IF) or even at baseband: there is not need for the matrix-vector product to be updated at the radio frequency (RF) rate. For example, for a baseband bandwidth of B GHz and carrier frequency $f >> B$ GHz, the digital mutual uncoupling algorithm requires a matrix-vector product that needs updating at a systolic array clock rate of $F_{clock} = 2B$ GHz rate (twice the baseband rate).

8.3.1 Brute-force computation

This work proposes a fast-algorithm[1] to realize $\mathbf{y} = \mathbf{QCu}$ where $\mathbf{u} = \mathbf{RK_c v}$ where $\mathbf{v}$ is the input without mutual coupling between elements, and $\mathbf{R}$ is a diagonal matrix that describes the varying gains and phase-offsets present in the receivers, and where $\mathbf{C}$ is the diagonal matrix that must be inserted before $\mathbf{Q}$ to calibrate the system. Ideally, $\mathbf{C} = \mathbf{R}^{-1}$ and is found experimentally by illuminating the array with a plane-wave at broadside direction. The realization would require measurement of S-parameters, one-time pre-computation of $\mathbf{Q}$ computed measured using $\mathbf{K_C}$. The computational (arithmetic) complexity of the brute-force computation of $\mathbf{y}$ is $\mathcal{O}(N^2)$. Although perfectly reasonable for small arrays (example, when $N = 4$) the arithmetic complexity grows quadratically with array size, and becomes computationally difficult even for reasonable large N. In a typical phased-array radar containing hundreds of elements, the computational complexity of the brute-force matrix-vector computation can become expensive in terms of both power and chip-area (cost).

[1]Dr. Sirani Perera at Daytona College of Arts and Sciences proposed and derived the mathematical proofs of this algorithm. This algorithm is used in this work in generating the inverse $\mathbf{Q}$ matrix and realize it on hardware for real-time performance evaluation.

8.3.2 Fast algorithms

To reduce the arithmetic complexity to a manageable level, this work explores a range of mathematical techniques that exploit the structural properties of the coupling matrix to facilitate a sparse matrix factorization. This in turn allows the desired matrix-vector product albeit at significantly reduced arithmetic complexity when compared to the direct (brute-force) approach. If the coupling is given by tridiagonal matrix $\mathbf{K}_c$, then its inverse $\mathbf{Q}$ can be computed and for a given time step vector $\mathbf{u}$, the mutual coupling effects can effectively by uncoupled via $\mathbf{y} = \mathbf{Q}\mathbf{u}$. The sparse factorization of the inverse matrix that uncouples the mutual coupling in the array takes the form,

$$\mathbf{Q} = \mathbf{G}_1\mathbf{G}_2\cdots\mathbf{G}_{N-1}\,\tilde{\mathbf{D}}\,\mathbf{G}_{N-1}^T\mathbf{G}_{N-2}^T\cdots\mathbf{G}_1^T \tag{8.1}$$

where $\mathbf{G}_k = \left[\begin{array}{c|cc|c} I_{k-1} & & & \\ \hline & 1 & -l_k & \\ & 0 & 1 & \\ \hline & & & I_{n-k-1} \end{array}\right]$ for $k = 1, 2, \cdots, N-1$, $\tilde{\mathbf{D}} = \text{diag}\left(\frac{1}{d_k}\right)_{k=1}^{N}$, $d_1 = a$, $l_1 = \frac{b_1}{a}$, $d_k = a - b_1 l_{k-1}$ and $l_k = \frac{b_1}{d_k}$ for $k = 2, 3, \cdots, N-1$, and $d_N = a - b_1 l_{N-1}$. The above mentioned matrix factorization of $\mathbf{Q}$ leads to a parallel digital realization, which realizes the desired uncoupling $\mathbf{y} = \mathbf{Q}\mathbf{u}$. The two coefficients defining the tridiagonal matrix $\mathbf{K_c}$ are $a \in \mathbb{C}$, $b_1 \in \mathbb{C}$ and are found experimentally via VNA measurements.

For a clock frequency of F_{clock} the computational throughput is $3(2N-1)F_{clock}$ real parallel multiplications per second, and $(12N-7)F_{clock}$ real parallel add/subs per second. The proposed algorithm has the arithmetic complexity of order $\mathcal{O}(N)$, which is a significant reduction compared to $\mathcal{O}(N^2)$ complexity that corresponds to a direct (i.e., brute force) matrix-vector product computation.

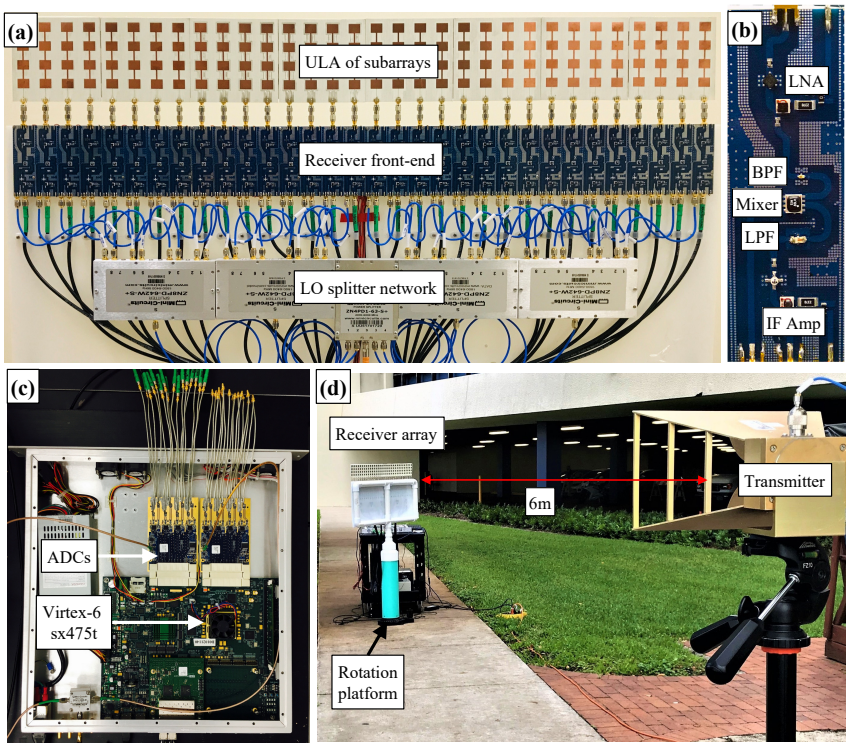

Figure 8.3: (a) A 32-element 5.8-GHz receiver front-end used for the experimental verification; (b) Close up of one PCB fabricated receiver chain (c) ROACH-2 FPGA platform used as digital back-end; (d) Measurement setup.

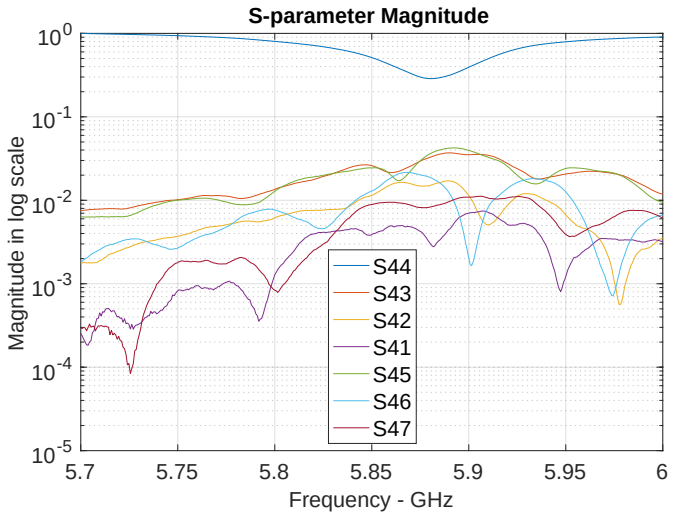

Figure 8.4: Measured S-parameters (return loss and mutual coupling) for seven-central elements of the designed antenna array.

8.4 Experimental verification

To verify the proposed real-time uncoupling algorithm, a fully-digital array receiver operating at 5.8 GHz is used. IF signals from the array are sampled through high speed ADCs on the digital back-end where the mutual uncoupling Q-block digital design is implemented. The design of this receiver array is already discussed in Section 8.4.2. So, the following section briefly cover the antenna array design, receiver chain design and the digital back-end details. Next, we continue the discussion on the measurements, and check the validation of the proposed uncoupling algorithm. The experimental setup is shown in Fig. 8.3.

8.4.1 Antenna array and S-Parameter measurement

The receiver array setup used for experimental validation consists of a 32-element uniform linear array (ULA) is shown in Fig. 8.3(a). Each antenna element is a 4×1 sub-array of patch antennas designed to resonate at 5.8 GHz and are spaced at 31 mm. The sub array employs a series-fed architecture and introduces additional gain along the vertical plane providing a sharper beam in the elevation plane. To verify the proposed work the center eight-elements of the ULA have been used. A VNA was used for measuring S-parameters on seven central elements of a 32-element array and are shown in Fig. 8.4. At 5.86 GHz, the measured $\mathbf{K_c}$ was found to be $a = 0.5756 - j0.8178$, $b_1 = 0.0052 + j0.0022$ and $b_2 = -0.0015 - j0.0005$.

8.4.2 Microwave receivers and digital back-end

The receiver array is designed to employ fully digital beamforming through a dedicated receiver for each antenna. Each receiver is a direct-conversion RF receiver

chain as shown in Fig. 8.3(b). The receiver chain includes a LNA (16 dB gain at 5.8 GHz, 2.4 dB noise figure), bandpass filter, mixer, lowpass filter, and an intermediate-frequency (IF) amplifier ($\approx$ 30 dB gain). Direct IF downconversion is done instead of I-Q, since the other quadrature signal is generated digitally using Hilbert transform. The IF signal is further low pass filtered and amplified before being sampled by ADCs on Reconfigurable Open Architecture Computing Hardware (ROACH-2) that is shown in Fig. 8.3(c). Further details and specifications for the array front-end can be found in Section 8.4.2.

For this work, ROACH-2 digital platform serves as the digital back-end. The signal flow graph corresponding to the mutual coupling algorithm as shown in Fig. 8.2 along with a spatial eight-point FFT based multi-beam beamforming architecture was implemented targeting the Xilinx Virtex-6 sx475t chip on the ROACH-2 processing platform. The calibration of the RF receiver chains were performed digitally by imposing gain and phase corrections in baseband. The gain and phase mismatches are premeasured using a reference signal (transmitted over the air from broadside) with respect to one receiver chain. Finally, the mismatches are compensated digitally by employing complex multipliers.

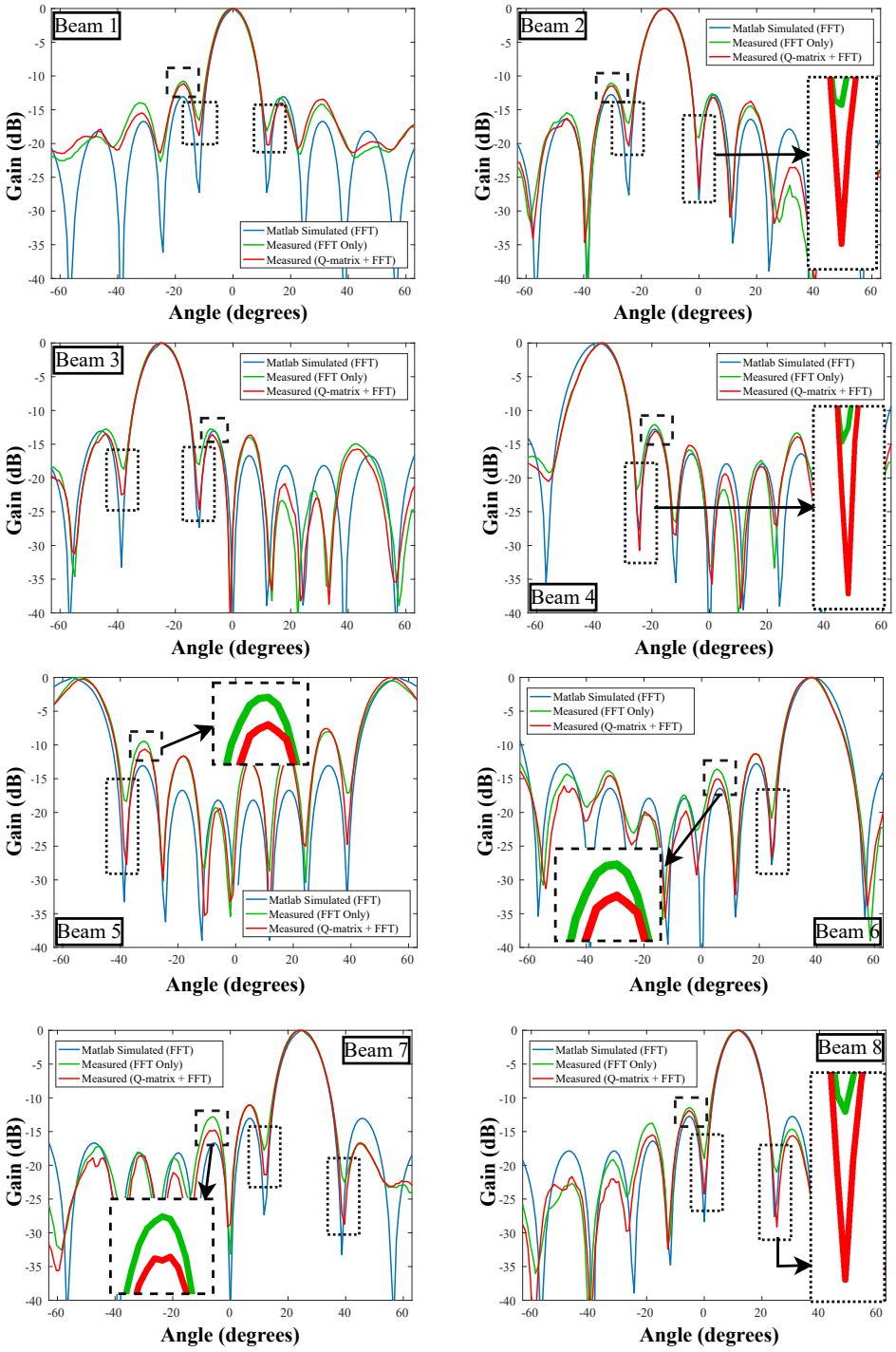

Figure 8.5: Comparison of measured beam patterns corresponding to all the eight bins of the spatial FFT based beams with and without mutual coupling compensation.

Table 8.1: Beam performance improvement using the proposed method

Beam	**Worst SLL reduction (dB) (dashes in Fig. 8.5)**	**Dominant null depths reduction (dB) (dots in Fig. 8.5)**
1	0.4	Left Null: 2.2 Right Null : 2.0
2	0.5	Left Null: 3.4 Right Null : 7.5
3	0.9	Left Null: 3.7 Right Null : 6.6
4	1	Right Null : 9
5	1.2	Right Null : 9.4
6	1.5	Left Null: 5.8
7	2.2	Left Null: 6.2 Right Null : 3.7
8	0.5	Left Null: 5.2 Right Null : 8

8.4.3 Measurements

The experimental setup for measurements is shown in Fig. 8.3(d). A horn antenna (13 dBi gain) is used to transmit a 5.86-GHz tone to the receiver array placed at a distance of 6 m. The low side LO of 5.85-GHz provided an IF of 10-MHz, which is sampled at 200-MHz by ROACH-2 ADCs. For measurement of the beampatterns, the angle of arrival of the incident wave was slowly varied by rotating the receiver array with transmitter fixed at its position. Fig. 8.5 shows the comparison in the measured beams without MC reduction (FFT only), with uncoupled mutual coupling (Q-matrix+FFT) and the ideal beampatterns for the eight FFT bins. The performance improvement by the proposed design in terms of worst sidelobe level (SLL) reduction and the null depths is summarized in Table. 8.1. The maximum and minimum SLL reductions are observed to be 0.4 dB and 2.2 dB in beams 1 and 7 respectively, while the nulls have been reduced by a maximum of 9.4 dB for Beam 5. The results indicate that the proposed design improves the side lobe level performance providing deeper nulls, thus beam patterns that approaching the ideal ones.

8.5 Contribution and comparison to previous work

In Chapter 7, section 7.6 we have looked into different techniques available in literature for compensating the effect of MC on antenna array's performance. The reader is referred to that section to identify the prior work. Similar to the Frost FIR filter–based digital MC compensation technique in chapter 8, we investigate another digital technique in this Chapter. Both techniques rely on developing a coupling matrix using the measured S-parameters. The idea behind the method presented in this Chapter is to compute the inverse of the coupling matrix and digitally uncouple the coupled multi-beam arrays. Since the brute-force computation of the inverse of matrix takes $\mathcal{O}(N^2)$ multiplications, we proposed a novel fast-algorithm that reduces the complexity to $\mathcal{O}(N)$. The proposed method is validate for a 8-element 5.8-GHz antenna array employing a 8-point FFT multi-beam beamformer. The measured beams with and without mutual coupling compensation technique are presented which convey the improvement in side-lobe levels and null performance using the proposed method.

The proposed method in this Chapter has relatively lower digital complexity compared to the Frost-FIR–based technique and has the flexibility to be applied to any beamforming approach. However, this method is well suited for narrow-band applications in contrast to Frost FIR filter–based technique which is a wideband approach.

8.6 Conclusion

Mutual coupling between elements of antenna arrays cause deviations to the expected beam responses in beamforming applications. Also, coupling of antennas causes LNA noise coupling that degrades the noise performance of the array receiver. These issues can be reduced by incorporating mutual coupling decoupling algorithms once the mutual coupling has been properly quantified. A novel fast algorithm has been proposed to digitally uncouple antenna arrays via inversion of $N \times N$ tridiagonal Toeplitz matrices having sparse factors. The proposed algorithm has been experimentally verified for an 8-element antenna array at 5.8 GHz. The measured results show 0.4-2.2 dB improvement of the highest (worst case) sidelobes on all measured beams of the spatial FFT–based eight beams while nulls (zeros in the array pattern) have been deepened by up to 9.4 dB, thereby moving closer to the desired beam responses

CHAPTER 9

CONCLUSIONS AND FUTURE WORK

Future wireless communication systems involving mmW bands will need large scale transceiver arrays with high gain to overcome the resulting free space path losses at those frequencies. These transceivers will most likely need the services of MIMO in combination with multi-beam beamforming to leverage the multi-path channels to improve SNR and mobile connectivity. This dissertation is focused on design and realization of fully-digital multi-beam phased arrays with digital signal processing performed using FPGA/RF SoC. Different analog and digital based multi-beam beamforming approaches have been proposed and validated with 2.4, 5.8 and 28 GHz RF system implementations. Digital designs to compensate the mutual coupling in the antenna arrays have also been investigated.

Chapter 2 presented a review of the concepts of beamforming and its techniques. We studied the properties of propagating plane waves(PW) and discussed how they can be applied for designing multi-beam beamformers. Using those concepts, a digital IIR filter employing 2D space-time networks is proposed in Chapter 3. These filters known by the name 2D spatially bandpass (SBP) filters encompass trapezoidal shaped passband and are used to realize multi-beams in real time. A 16-element 2.4-GHz I-Q direct conversion receiver array is built for its experimental verification. ROACH-2 FPGA platform with 32 ADC channels is used as the DSP back-end and to implement the digital circuitry. For proof-of-concept verification, the measurements are carried out for a two-beam case realized on the ROACH-2. The measured beams were well aligned with the fixed-point MATLAB simulated beams. It is also found that this approach would save 81.3% of hardware resources compared to an FIR implementation on the same FPGA platform.

Chapter 4 discussed in detail another multi-beam digital beamformer using fast Fourier transform. For the first time in literature, a fully digital 28-GHz four-element multi-beam receiver array is realized across the entire 800 MHz bandwidth. The Xilinx RF SoC based ZCU 1275 digital platform is used as the digital back-end to sample the incoming eight I-Q channels and to implement the four-point spatial FFT beamformer. Polyphase architectures have been employed to support the full bandwidth. The digitally measured beams were observed to be in good agreement with the simulated beams. The next chapter presented an analog implementation of a multi-beam beamformer using lenses and a focal plane array, also at 28-GHz. Lens based architectures replace the conventional analog phase shifters to produce sharp beams with reduced complexity and power consumption. An ABS material lens with 29 dBi directivity is designed and 3D printed for this work. The 28-GHz array receiver setup built in Chapter 4 is used for this realization and the antenna array acts as the focal plane array for the lens. For verification, measurements are conducted with the test setup configured for 28.1-GHz transmit frequency producing a 100-MHz IF. These measured array factors are compared to the CST simulated array factors. Although the gain enhancement due to the lens is not as anticipated, the beam positions are very well aligned which validate the analog multi-beam implementation. The study of these mismatches will be a subject of future work. At the end, this chapter also discussed briefly about a hybrid beamforming approach with an array of lenses called lenslet array that can provide very sharp beams with additional degrees of freedom arising from the digital end. The implementation of this lenslet array would be very promising for future wireless access points and is a subject of future work.

An FFT-based spatio-temporal RF directional sensing system is also proposed in this dissertation. These systems aimed at exploiting the concepts of spatio-temporal

spectral white spaces and be able to provide opportunistic channel access in the crowded spectrum. The proposed system performs sensing over 16 look direction simultaneously through a 16-point FFT based multi-beam beamformer implemented on ROACH-2 based FPGA system. Experimental results obtained for 2.4-GHz Wi-fi devices show the white spaces available during their operation, thus verifying the proof-of-concept directional sensing of the proposed system. The directional sensor in combination with a temporal FFT can be used to distinguish different channels along with the direction of the sources. Its realization can be a subject of future work.

Fully-digital approaches provide plethora of array factors and offer more degrees of freedom. However, the real time performance of an array of elements is effected by the non-ideal effects present in the antenna systems especially mutual coupling. Chapter 7 and 8 presented digital mutual coupling compensation techniques for these fully digital systems. The first design is based on finding a mutual coupling transfer function with the help of measured S-parameters of the array. This MC transfer function is integrated to a Frost-based FIR beamfilter to compensate the MC effects while realizing the multi-beams simultaneously. A 32-element 5.8-GHz path antenna array and a $7x7$ wideband TCDA array (1-6 GHz) are employed as the linear array and planar array for 2D and 3D Frost based FIR beamfilters validation. For the linear case, more than 5 dB SL level reduction is achieved for 20-MHz basedband bandwidth. While, the experimental results for the 3-D case indicated a 5.2 dB null performance improvement for 100-MHz bandwidth. Similarly, a novel fast-algorithm has been proposed in Chapter 8 to digitally uncouple antenna arrays via inversion of NxN tridiagonal Toeplitz matrices having sparse factors. This is experimentally verified for an eight-element antenna array at 5.8-GHz. The measured results show 0.4-2.2 dB improvement of the highest sidelobes on all measured beams while the

nulls have been deepened by upto 9.4 dB. The fast algorithm based approach is a narrow band approach, hence the wideband design and realization can be a subject of future work.

BIBLIOGRAPHY

[1] "Voice-led Marketing in China," Jun. 2019. [Online]. Available: https://www.phdmedia.com/china-cn/phd-china-whitepaper-voice-led-marketing-in-china/

[2] "Satellite communications with multi-beam beamforming," Apr. 2019. [Online]. Available: https://spacefl

[3] "Starlink cubesats," 2020. [Online]. Available: https://youtu.be/giQ8xEWjnBs

[4] "Hmc1065lp4e-downconverter." [Online]. Available: https://www.analog.com/media/en/technical-documentation/data-sheets/hmc1065.pdf

[5] Xilinx, "Zynq UltraScale+ RFSoC RF Data Converter 2.0," Apr. 2018. [Online]. Available: https://www.xilinx.com/support/documentation/ip_documentation/usp_rf_data_converter/v2_0/pg269-rf-data-converter.pdf

[6] Harry L. Van Trees, *Optimum Array Processing: Part IV of Detection, Estimation, and Modulation Theory*. NY: John Wiley & Sons, 2002.

[7] M. J. Marcus, "5G and "IMT for 2020 and beyond" [Spectrum Policy and Regulatory Issues]," *IEEE Wireless Communications*, vol. 22, no. 4, pp. 2–3, 2015.

[8] Rappaport, Theodore S and others, *Wireless communications: principles and practice*. prentice hall PTR New Jersey, 1996, vol. 2.

[9] C. Dehos, J. L. González, A. De Domenico, D. Ktenas, and L. Dussopt, "Millimeter-wave access and backhauling: The solution to the exponential data traffic increase in 5G mobile communications systems?" *IEEE Communications Magazine*, vol. 52, no. 9, pp. 88–95, 2014.

[10] Y. Kim, H.-Y. Lee, P. Hwang, R. K. Patro, J. Lee, W. Roh, and K. Cheun, "Feasibility of mobile cellular communications at millimeter wave frequency," *IEEE Journal of selected topics in Signal Processing*, vol. 10, no. 3, pp. 589–599, 2016.

[11] Joaquin RESTREPO, "Spectrum Allocation for 5G International Framework," Sep. 2019. [Online]. Avail-

able: https://www.itu.int/en/ITU-D/Regulatory-Market/Documents/Events2019/Togo/5G-Ws/Ses4_Joaquin_Spectrum-5G.pdf

[12] "The FCC's 5G FAST Plan," Apr. 2019. [Online]. Available: https://news.itu.int/wrc-19-agrees-to-identify-new-frequency-bands-for-5g/

[13] M. Bennis, M. Debbah, and H. V. Poor, "Ultrareliable and Low-Latency Wireless Communication: Tail, Risk, and Scale," *Proceedings of the IEEE*, vol. 106, no. 10, pp. 1834–1853, 2018.

[14] "Making 5G NR A Reality," Feb. 2013. [Online]. Available: https://www.qualcomm.com/documents/whitepaper-making-5g-nr-reality.

[15] S. Borkar and H. Pande, "Application of 5G next generation network to Internet of Things," in *2016 International Conference on Internet of Things and Applications (IOTA)*, Jan 2016, pp. 443–447.

[16] M. Jaber, M. A. Imran, R. Tafazolli, and A. Tukmanov, "5G Backhaul Challenges and Emerging Research Directions: A Survey," *IEEE Access*, vol. 4, pp. 1743–1766, 2016.

[17] W. Hong, K.-H. Baek, Y. Lee, Y. Kim, and S.-T. Ko, "Study and prototyping of practically large-scale mmWave antenna systems for 5G cellular devices," *IEEE Communications Magazine*, vol. 52, no. 9, pp. 63–69, 2014.

[18] S. Rajagopal, S. Abu-Surra, Z. Pi, and F. Khan, "Antenna array design for multi-Gbps mmWave mobile broadband communication," in *2011 IEEE Global Telecommunications Conference-GLOBECOM 2011*. IEEE, 2011, pp. 1–6.

[19] T. S. Rappaport, S. Sun, R. Mayzus, H. Zhao, Y. Azar, K. Wang, G. N. Wong, J. K. Schulz, M. Samimi, and F. Gutierrez, "Millimeter wave mobile communications for 5G cellular: It will work!" *IEEE access*, vol. 1, pp. 335–349, 2013.

[20] J. Zhang, X. Ge, Q. Li, M. Guizani, and Y. Zhang, "5G millimeter-wave antenna array: Design and challenges," *IEEE Wireless communications*, vol. 24, no. 2, pp. 106–112, 2016.

[21] S. Hur, T. Kim, D. J. Love, J. V. Krogmeier, T. A. Thomas, and A. Ghosh, "Millimeter wave beamforming for wireless backhaul and access in small cell

networks," *IEEE transactions on communications*, vol. 61, no. 10, pp. 4391–4403, 2013.

[22] B. D. Van Veen and K. M. Buckley, "Beamforming: A versatile approach to spatial filtering," *IEEE assp magazine*, vol. 5, no. 2, pp. 4–24, 1988.

[23] T. L. Marzetta, "Noncooperative cellular wireless with unlimited numbers of base station antennas," *IEEE transactions on wireless communications*, vol. 9, no. 11, pp. 3590–3600, 2010.

[24] E. G. Larsson, O. Edfors, F. Tufvesson, and T. L. Marzetta, "Massive MIMO for next generation wireless systems," *IEEE communications magazine*, vol. 52, no. 2, pp. 186–195, 2014.

[25] J. Brady, J. Hogan, and A. Sayeed, "Multi-beam MIMO prototype for real-time multiuser communication at 28 GHz," in *2016 IEEE Globecom Workshops (GC Wkshps)*. IEEE, 2016, pp. 1–6.

[26] W. Hong, Z. H. Jiang, C. Yu, J. Zhou, P. Chen, Z. Yu, H. Zhang, B. Yang, X. Pang, M. Jiang *et al.*, "Multibeam antenna technologies for 5G wireless communications," *IEEE Transactions on Antennas and Propagation*, vol. 65, no. 12, pp. 6231–6249, 2017.

[27] N. R. A. Observatory, "Very Large Array," 2019. [Online]. Available: https:http://www.vla.nrao.edu/

[28] S. Sun, T. S. Rappaport, M. Shafi, and H. Tataria, "Analytical framework of hybrid beamforming in multi-cell millimeter-wave systems," *IEEE Transactions on Wireless Communications*, vol. 17, no. 11, pp. 7528–7543, 2018.

[29] S. Sun, T. S. Rappaport, M. Shafi, P. Tang, J. Zhang, and P. J. Smith, "Propagation models and performance evaluation for 5G millimeter-wave bands," *IEEE Transactions on Vehicular Technology*, vol. 67, no. 9, pp. 8422–8439, 2018.

[30] T. S. Rappaport, Y. Xing, O. Kanhere, S. Ju, A. Madanayake, S. Mandal, A. Alkhateeb, and G. C. Trichopoulos, "Wireless communications and applications above 100 GHz: Opportunities and challenges for 6G and beyond," *IEEE Access*, vol. 7, pp. 78 729–78 757, 2019.

[31] D. Choudhury, "5G wireless and millimeter wave technology evolution: An overview," in *2015 IEEE MTT-S International Microwave Symposium*. IEEE, 2015, pp. 1–4.

[32] E. Dahlman, S. Parkvall, and J. Skold, *5G NR: The next generation wireless access technology*. Academic Press, 2018.

[33] S. Pulipati, V. Ariyarathna, U. De Silva, N. Akram, E. Alwan, and A. Madanayake, "Design of 28 GHz 64-QAM digital receiver," in *2019 International Workshop on Antenna Technology (iWAT)*, 2019, pp. 193–196.

[34] "Millimeter Wave Digital Arrays." [Online]. Available: https://www.darpa.mil/program/millimeter-wave-digital-arrays

[35] S. Harman, "Holographic Radar Development," *Microwave Journal*, vol. 64, no. 02, Feb. 2021.

[36] J. P. Doane, K. Sertel, and J. L. Volakis, "A wideband, wide scanning tightly coupled dipole array with integrated balun (TCDA-IB)," *IEEE Transactions on Antennas and Propagation*, vol. 61, no. 9, pp. 4538–4548, 9 2013.

[37] M. Aning, M. Aning *et al.*, *Wireless receiver design for digital communications*. SciTech Pub., 2012.

[38] L. Belostotski *et al.*, "Low-Noise Amplifier Design Considerations For Use in Antenna Arrays," *IEEE Trans. on Antennas and Propagation*, vol. 63, no. 6, pp. 2508–2520, Jun. 2015.

[39] C. K. Hansen, K. F. Warnick, B. D. Jeffs, J. R. Fisher, and R. Bradley, "Interference mitigation using a focal plane array," *Radio Science*, vol. 40, no. 05, pp. 1–13, Oct 2005.

[40] J. Lee, S. Kim, and J. Jang, "Reduction of Mutual Coupling in Planar Multiple Antenna by Using 1-D EBG and SRR Structures," *IEEE Transactions on Antennas and Propagation*, vol. 63, no. 9, pp. 4194–4198, 2015.

[41] W. L. Stutzman and G. A. Thiele, *Antenna theory and design*. John Wiley & Sons, 2012.

[42] C. A. Balanis, *Antenna theory: analysis and design*. John wiley & sons, 2016.

[43] T. K. Gunaratne, "Beamforming of temporally broadband bandpass plane waves using 2D FIR trapezoidal filters," Ph.D. dissertation, University of Calgary, 2006.

[44] L. Bruton and N. Bartley, "Three-dimensional image processing using the concept of network resonance," *IEEE Transactions on Circuits and Systems*, vol. 32, no. 7, pp. 664–672, 1985.

[45] L. T. Bruton, "Three-dimensional cone filter banks," *IEEE Transactions on Circuits and Systems I: Fundamental Theory and Applications*, vol. 50, no. 2, pp. 208–216, 2003.

[46] D. E. Dudgeon, "Multidimensional digital signal processing," *Engewood Cliffs*, 1983.

[47] A. Madanayake and L. T. Bruton, "A real-time systolic array processor implementation of two-dimensional IIR filters for radio-frequency smart antenna applications," in *2008 IEEE International Symposium on Circuits and Systems*, 2008, pp. 1252–1255.

[48] T. K. Gunaratne and L. T. Bruton, "Broadband Beamforming of Bandpass Plane Waves using 2D FIR Trapezoidal Filters at Baseband," in *APCCAS 2006 - 2006 IEEE Asia Pacific Conference on Circuits and Systems*, 2006, pp. 546–549.

[49] W. Liu and S. Weiss, *Wideband beamforming: concepts and techniques*. John Wiley & Sons, 2010, vol. 17.

[50] H. Iwakura, "Realization of tapped delay lines using switched-capacitor LDI ladders and application to FIR filter design," *IEEE Transactions on Circuits and Systems II: Analog and Digital Signal Processing*, vol. 40, no. 12, pp. 794–797, 1993.

[51] N. Lin, W. Liu, and R. Langley, "Performance analysis of a broadband beamforming structure without tapped delay-lines," in *2007 15th International Conference on Digital Signal Processing*. IEEE, 2007, pp. 583–586.

[52] J. E. Zekry, G. N. Daoud, H. A. Ghali, and H. F. Ragai, "Design and simulation of digitally tunable high-Q on-chip inductor," in *2007 Internatonal Conference on Microelectronics*. IEEE, 2007, pp. 239–242.

[53] A. Madanayake, *Real-time FPGA architectures for space-time frequency-planar MDSP*, 2008.

[54] R. M. Joshi, A. Madanayake, J. Adikari, and L. T. Bruton, "Synthesis and array processor realization of a 2-D IIR beam filter for wireless applications," *IEEE Transactions on Very Large Scale Integration (VLSI) Systems*, vol. 20, no. 12, pp. 2241–2254, 2012.

[55] A. Madanayake, T. Randeny, N. Udayanga, A. Sengupta, G. Jones, C. Wijenayake, and L. T. Bruton, "Applications of RF aperture-array spatially-bandpass 2-D IIR filters in sub-Nyquist spectrum sensing, wideband Doppler radar and radio astronomy beamforming," *Multidimensional Systems and Signal Processing*, vol. 28, no. 4, pp. 1523–1548, 2017.

[56] A. Madanayake and L. Bruton, "A review of 2D/3D IIR plane-wave real-time digital filter circuits," in *Canadian Conference on Electrical and Computer Engineering, 2005.* IEEE, 2005, pp. 1935–1941.

[57] T. K. Gunaratne and L. T. Bruton, "Adaptive complex-coefficient 2D FIR trapezoidal filters for broadband beamforming in cognitive radio systems," *Circuits, Systems, and Signal Processing*, vol. 30, no. 3, pp. 587–608, 2011.

[58] ——, "Beamforming of temporally-broadband-bandpass plane waves using real polyphase 2-D FIR trapezoidal filters," in *2007 IEEE International Symposium on Circuits and Systems.* IEEE, 2007, pp. 589–592.

[59] ——, "Beamforming of broad-band bandpass plane waves using polyphase 2-D FIR trapezoidal filters," *IEEE Transactions on Circuits and Systems I: Regular Papers*, vol. 55, no. 3, pp. 838–850, 2008.

[60] I. Moazzen and P. Agathoklis, "Broadband beamforming using 2D trapezoidal filters and nested arrays," in *Proceedings of 2011 IEEE Pacific Rim Conference on Communications, Computers and Signal Processing.* IEEE, 2011, pp. 488–493.

[61] R. A. Horn, R. A. Horn, and C. R. Johnson, *Topics in matrix analysis.* Cambridge university press, 1994.

[62] H. Moody, "The systematic design of the Butler matrix," *IEEE Transactions on Antennas and Propagation*, vol. 12, no. 6, pp. 786–788, 1964.

[63] F. Huang, W. Chen, and M. Rao, "Switched-beam antenna array based on Butler matrix for 5G wireless communication," in *2016 IEEE International Workshop on Electromagnetics: Applications and Student Innovation Competition (iWEM)*. IEEE, 2016, pp. 1–3.

[64] S. K. Pulipati, V. Ariyarathna, A. Madanayake, R. T. Wijesekara, C. U. Edussooriya, and L. T. Bruton, "A 16-Element 2.4-GHz Multibeam Array Receiver Using 2-D Spatially Bandpass Digital Filters," *IEEE Transactions on Aerospace and Electronic Systems*, vol. 55, no. 6, pp. 3029–3038, 2019.

[65] K. K. Parhi and D. G. Messerschmitt, "Pipeline interleaving and parallelism in recursive digital filters. I. Pipelining using scattered look-ahead and decomposition," *IEEE Transactions on Acoustics, Speech, and Signal Processing*, vol. 37, no. 7, pp. 1099–1117, 1989.

[66] P. Agathoklis and L. Bruton, "Practical-BIBO stability of n-dimensional discrete systems," in *IEE Proceedings G (Electronic Circuits and Systems)*, vol. 130, no. 6. IET, 1983, pp. 236–242.

[67] A. Madanayake and L. T. Bruton, "A review of 2D/3D IIR plane-wave real-time digital filter circuits," in *Canadian Conference on Electrical and Computer Engineering, 2005.*, 2005, pp. 1935–1941.

[68] H. L. P. A. Madanayake, S. V. Hum, and L. T. Bruton, "A Systolic Array 2-D IIR Broadband RF Beamformer," *IEEE Transactions on Circuits and Systems II: Express Briefs*, vol. 55, no. 12, pp. 1244–1248, 2008.

[69] S. Pulipati, V. Ariyarathna, and A. Madanayake, "A 16-Element 2.4-GHz Digital Array Receiver using 2-D IIR Spatially-Bandpass Plane-Wave Filter," in *2018 IEEE/MTT-S International Microwave Symposium - IMS*, 2018, pp. 667–670.

[70] J. G. Proakis and D. G. Manolakis, "Digital signal processing," *PHI publication*, 2004.

[71] "ROACH-2 Introduction." [Online]. Available: http://casper.berkeley.edu

[72] "ROACH-2 ADCs." [Online]. Available: https://casper.ssl.berkeley.edu/wiki/ADC16x250-8_coax_rev_2

[73] A. Madanayake, V. Ariyrathna, and S. kumar Pulipati, "Design and prototype implementation of an 8-beam 2.4 GHz array receiver for digital beamforming,"

in *2017 IEEE National Aerospace and Electronics Conference (NAECON)*. IEEE, 2017, pp. 91–97.

[74] S. Pulipati, V. Ariyarathna, U. De Silva, N. Akram, E. Alwan, A. Madanayake, S. Mandal, and T. S. Rappaport, "A Direct-Conversion Digital Beamforming Array Receiver with 800 MHz Channel Bandwidth at 28 GHz using Xilinx RF SoC," in *2019 IEEE International Conference on Microwaves, Antennas, Communications and Electronic Systems (COMCAS)*. IEEE, 2019, pp. 1–5.

[75] S. Pulipati, V. Ariyarathna, M. R. Khan, S. Bhardwaj, and A. Madanayake, "Aperture-Array & Lens+ FPA Multi-Beam Digital Receivers at 28 GHz on Xilinx ZCU 1275 RF SoC," in *2020 IEEE/MTT-S International Microwave Symposium (IMS)*. IEEE, 2020, pp. 555–558.

[76] S. W. Ellingson and W. Cazemier, "Efficient multibeam synthesis with interference nulling for large arrays," *IEEE Transactions on antennas and propagation*, vol. 51, no. 3, pp. 503–511, 2003.

[77] J. O. Coleman, "A generalized FFT for many simultaneous receive beams," Naval Research lab Washington DC signal processing section/advanced RADAR systems, Tech. Rep., 2007.

[78] J. W. Cooley and J. W. Tukey, "An algorithm for the machine calculation of complex Fourier series," *Mathematics of computation*, vol. 19, no. 90, pp. 297–301, 1965.

[79] R. Miura, T. Tanaka, I. Chiba, A. Horie, and Y. Karasawa, "Beamforming experiment with a DBF multibeam antenna in a mobile satellite environment," *IEEE Transactions on Antennas and Propagation*, vol. 45, no. 4, pp. 707–714, 1997.

[80] P. Xingdong, H. Wei, Y. Tianyang, and L. Linsheng, "Design and implementation of an active multibeam antenna system with 64 RF channels and 256 antenna elements for massive MIMO application in 5G wireless communications," *China communications*, vol. 11, no. 11, pp. 16–23, 2014.

[81] M. Sayginer and G. M. Rebeiz, "An eight-element 2–16-GHz programmable phased array receiver with one, two, or four simultaneous beams in SiGe BiCMOS," *IEEE Transactions on Microwave Theory and Techniques*, vol. 64, no. 12, pp. 4585–4597, 2016.

[82] Y. A. Atesal, B. Cetinoneri, K. M. Ho, and G. M. Rebeiz, "A two-channel 8–20-GHz SiGe BiCMOS receiver with selectable IFs for multibeam phased-array digital beamforming applications," *IEEE Transactions on Microwave Theory and Techniques*, vol. 59, no. 3, pp. 716–726, 2011.

[83] S. Voinigescu, *High-frequency integrated circuits*. Cambridge University Press, 2013.

[84] "FCC establishes procedures for first 5G spectrum auctions," Federal Communications Commission: Public Notice (FCC 18-109), Aug. 2018, Available: https://docs.fcc.gov/public/attachments/DOC-353228A1.pdf.

[85] B. Sklar, *Digital Communications: Fundamentals and Applications*. Prentice-Hall, 1988.

[86] Xilinx®, "Zynq UltraScale RFSoC Data Sheet DC and AC Switching Characteristics," Available: https://tinyurl.com/yc728o6x.

[87] V. Ariyarathna, "Algorithms and Circuits for Analog-Digital Hybrid Multibeam Arrays," Ph.D. dissertation, Florida International University, 2019. [Online]. Available: https://digitalcommons.fiu.edu/etd/4321

[88] N. Akram, "Digital and Mixed Domain Complexity Hardware Reduction Algorithms and Implementations for Massive MIMO," Ph.D. dissertation, Florida International University, 2020.

[89] R. A. Sainati, *CAD of microstrip antennas for wireless applications*. Artech House, Inc., 1996.

[90] Xilinx, "ZCU1275 Characterization Board User Guide (v1.0)," Nov. 2018. [Online]. Available: https://www.xilinx.com/support/documentation/boards_and_kits/zcu1275/ug1285-zcu1275-char-bd.pdf

[91] "Hwclk102 clock module clock configuration." [Online]. Available: https://xilinx-wiki.atlassian.net/wiki/spaces/A/pages/63799327/ZCU1275+ZCU1285+MTS+Design+Example

[92] V. Ariyarathna, D. F. G. Coelho, S. Pulipati, R. J. Cintra, F. M. Bayer, V. S. Dimitrov, and A. Madanayake, "Multibeam digital array receiver using a 16-point multiplierless DFT approximation," *IEEE Transactions on Antennas and Propagation*, vol. 67, no. 2, pp. 925–933, Feb 2019.

[93] A. Madanayake, V. Ariyarathna, S. Madishetty, S. Pulipati, R. J. Cintra, D. Coelho, R. Oliviera, F. M. Bayer, L. Belostotski, S. Mandal, and T. S. Rappaport, "Towards a low-SWaP 1024-beam digital array: A 32-beam subsystem at 5.8 GHz," *IEEE Transactions on Antennas and Propagation*, vol. 68, no. 2, pp. 900–912, 2020.

[94] Y. Yeh, B. Walker, E. Balboni, and B. A. Floyd, "A 28-GHz 4-channel dual-vector receiver phased array in SiGe BiCMOS technology," in *2016 IEEE Radio Frequency Integrated Circuits Symposium (RFIC)*, 2016, pp. 352–355.

[95] E. H. Mujammami and A. Sebak, "Analog Beamforming System Using Rotman Lens for 5G Applications at 28 GHz," in *2019 IEEE International Symposium on Antennas and Propagation and USNC-URSI Radio Science Meeting*, 2019, pp. 153–154.

[96] T. Obara, Y. Inoue, Y. Aoki, S. Suyama, J. Lee, and Y. Okumurav, "Experiment of 28 GHz Band 5G super wideband transmission using beamforming and beam tracking in high mobility environment," in *2016 IEEE 27th Annual International Symposium on Personal, Indoor, and Mobile Radio Communications (PIMRC)*, 2016, pp. 1–5.

[97] V. Venkateswaran and A. van der Veen, "Analog Beamforming in MIMO Communications With Phase Shift Networks and Online Channel Estimation," *IEEE Transactions on Signal Processing*, vol. 58, no. 8, pp. 4131–4143, 2010.

[98] H. Iwakura, "Realization of tapped delay lines using switched-capacitor LDI ladders and application to FIR filter design," *IEEE Transactions on Circuits and Systems II: Analog and Digital Signal Processing*, vol. 40, no. 12, pp. 794–797, 1993.

[99] V. Ariyarathna, N. Udayanga, A. Madanayake, S. M. Perera, L. Belostotski, and R. J. Cintra, "Design methodology of an analog 9-beam squint-free wideband IF multi-beamformer for mmW applications," in *2017 Moratuwa Engineering Research Conference (MERCon)*, 2017, pp. 236–240.

[100] A. Madanayake, V. Ariyarathna, N. Udayanga, L. Belostotski, S. K. Perera, and R. J. Cintra, "Design of a low-complexity wideband analog true-time-delay 5-beam array in 65nm CMOS," in *2017 IEEE 60th International Midwest Symposium on Circuits and Systems (MWSCAS)*, 2017, pp. 1204–1207.

[101] R. Rotman, M. Tur, and L. Yaron, "True Time Delay in Phased Arrays," *Proceedings of the IEEE*, vol. 104, no. 3, pp. 504–518, 2016.

[102] R. Rotman, S. Rotman, W. Rotman, O. Raz, and M. Tur, "Wideband RF beamforming: the Rotman lens vs. photonic beamforming," in *2005 IEEE Antennas and Propagation Society International Symposium*, vol. 2B, 2005, pp. 23–26 vol. 2B.

[103] D. B. Hayman, T. S. Bird, K. P. Esselle, and P. J. Hall, "Experimental Demonstration of Focal Plane Array Beamforming in a Prototype Radiotelescope," *IEEE Transactions on Antennas and Propagation*, vol. 58, no. 6, pp. 1922–1934, June 2010.

[104] A. Sayeed, C. Hall, and K. Y. Zhu, "A lens array multi-beam MIMO testbed for real-time mmwave communication and sensing," in *Proceedings of the 1st ACM Workshop on Millimeter-Wave Networks and Sensing Systems 2017*. ACM, 2017, pp. 35–40.

[105] J. R. Nagel, K. F. Warnick, B. D. Jeffs, J. R. Fisher, and R. Bradley, "Experimental verification of radio frequency interference mitigation with a focal plane array feed," *Radio Science*, vol. 42, no. 06, pp. 1–8, Dec 2007.

[106] A. Bisognin, N. Nachabe, C. Luxey, F. Gianesello, D. Gloria, J. R. Costa, C. A. Fernandes, Y. Alvarez, A. Arboleya-Arboleya, J. Laviada, F. Las-Heras, N. Dolatsha, B. Grave, M. Sawaby, and A. Arbabian, "Ball grid array module with integrated shaped lens for 5g backhaul/fronthaul communications in f-band," *IEEE Transactions on Antennas and Propagation*, vol. 65, no. 12, pp. 6380–6394, Dec 2017.

[107] W. B. Dou and Z. L. Sun, "Ray Tracing on Extended Hemispherical and Elliptical Silicon Dielectric Lenses," *International Journal of Infrared and Millimeter Waves*, vol. 16, no. 11, pp. 1993–2002, nov 1995. [Online]. Available: http://link.springer.com/10.1007/BF02072553

[108] P. Turalchuk, I. Munina, and A. Shitvov, "Analog Beamforming Based on Fourier Rotman Lens for Multibeam Applications," in *2018 48th European Microwave Conference (EuMC)*, 2018, pp. 1573–1576.

[109] Y. Gao, M. Khaliel, F. Zheng, and T. Kaiser, "Rotman Lens Based Hybrid Analog–Digital Beamforming in Massive MIMO Systems: Array Architectures, Beam Selection Algorithms and Experiments," *IEEE Transactions on Vehicular Technology*, vol. 66, no. 10, pp. 9134–9148, 2017.

[110] S. Pulipati, V. Ariyarathna, C. U. S. Edussooriya, C. Wijenayake, X. Wang, and A. Madanayake, "Real-Time FPGA-Based Multi-Beam Directional Sensing of 2.4 GHz ISM RF Sources," in *2019 Moratuwa Engineering Research Conference (MERCon)*, 2019, pp. 129–134.

[111] J. Mitola and G. Q. Maquire, "Cognitive radio: making software radios more personal," *IEEE Personal Communications*, vol. 6, no. 4, pp. 13–18, 1999.

[112] S. Haykin, "Cognitive radio: Brain-empowered wireless communications," *IEEE Journal on Selected Areas in Communications*, vol. 22, no. 2, pp. 201–220, 2005.

[113] A. Ali and W. Hamouda, "Advances on spectrum sensing for cognitive radio networks: Theory and applications," *IEEE Communications Surveys & Tutorials*, vol. 19, no. 2, pp. 1277–1304, 2017.

[114] C. Wijenayake, A. Madanayake, J. Kota, and L. T. Bruton, "Space-time spectral white spaces in cognitive radio: Theory, algorithms, and circuits," *IEEE Journal on Emerging and Selected Topics in Circuits and Systems*, vol. 3, no. 4, pp. 640–653, 2013.

[115] Q. Zhao and B. M. Sadler, "A survey of dynamic spectrum access," *IEEE Signal Processing Magazine*, vol. 24, no. 3, pp. 79–89, 2007.

[116] M. Höyhtyä, A. Mämmelä, M. Eskola, M. Matinmikko, J. Kalliovaara, J. Ojaniemi, J. Suutala, R. Ekman, R. Bacchus, and D. Roberson, "Spectrum occupancy measurements: A survey and use of interference maps," *IEEE Communications Surveys & Tutorials*, vol. 18, no. 4, pp. 2386–2414, 2016.

[117] C. Lee and M. Haenggi, "Delay analysis of spatio-temporal channel access for cognitive networks," in *Proc. IEEE International Conference on Communications*, 2011, pp. 1–5.

[118] C. Liu and M. Jin, "Maximum-minimum spatial spectrum detection for cognitive radio using parasitic antenna arrays," in *Proc. IEEE/CIC International Conference on Communications in China (ICCC)*, 2014, pp. 365–369.

[119] W. Na, J. Yoon, S. Cho, D. Griffith, and N. Golmie, "Centralized cooperative directional spectrum sensing for cognitive radio networks," *IEEE Transactions on Mobile Computing*, vol. 17, no. 6, pp. 1260–1274, 2018.

[120] R. Qian, M. Sellathurai, and T. Ratnarajah, "Directional spectrum sensing for cognitive radio using ESPAR arrays with a single RF chain," in *Proc. European Conference on Networks and Communications (EuCNC)*, 2014, pp. 1–5.

[121] D. Wilcox, E. Tsakalaki, A. Kortun, T. Ratnarajah, C. B. Papadias, and M. Sellathurai, "On spatial domain cognitive radio using single-radio parasitic antenna arrays," *IEEE Journal on Selected Areas in Communications*, vol. 31, no. 3, pp. 571–580, 2013.

[122] B. H. Qureshi, R. K. Sharma, N. Murtaza, M. Grimm, A. Krah, M. A. Hein, A. Heuberger, and R. S. Thoma, "Exploiting spatial dimension in spectrum sensing using a sector antenna: A ray tracer based analysis," in *Proc. IEEE 77th Vehicular Technology Conference (VTC Spring)*, 2013, pp. 1–5.

[123] H. Sarvanko, M. Höyhtyä, M. Matinmikko, and A. Mämmelä, "Exploiting spatial dimension in cognitive radios and networks," in *Proc. 6th International ICST Conference on Cognitive Radio Oriented Wireless Networks and Communications (CROWNCOM)*, 2011, pp. 360–364.

[124] Z. Xu, Q. Liu, C. Zhao, Z. Zhou, and K. S. Kwak, "Spectrum sense utilizing multi-antenna beams scanning in cognitive radio networks," in *Proc. 9th International Symposium on Communications and Information Technology*, 2009, pp. 1369–1374.

[125] H. Yazdani and A. Vosoughi, "On cognitive radio systems with directional antennas and imperfect spectrum sensing," in *Proc. IEEE International Conference on Acoustics, Speech and Signal Processing (ICASSP)*, 2017, pp. 3589–3593.

[126] G. Zhao, J. Ma, G. Ye Li, T. Wu, Y. Kwon, A. Soong, and C. Yang, "Spatial spectrum holes for cognitive radio with relay-assisted directional transmission," *IEEE Transactions on Wireless Communications*, vol. 8, no. 10, pp. 5270–5279, 2009.

[127] V. Ariyarathne, V. A. Coutinho, S. Pulipati, A. Madanayake, R. T. Wijesekara, C. U. S. Edussooriya, L. T. Bruton, T. K. Gunaratne, and R. J. Cintra, "Real-time 2-D FIR trapezoidal digital filters for 2.4 GHz aperture receiver applications," in *Moratuwa Engineering Research Conference*, 2018, pp. 1–6.

[128] R. E. Blahut, *Fast Algorithms for Signal Processing*. Cambridge University Press, 2010.

[129] S. Pulipati, V. Ariyarathna, A. L. Jayaweera, C. U. S. Edussooriya, C. Wijenayake, L. Belostotski, and A. Madanayake, "FPGA-Based 2-D FIR Frost Beamformers with Digital Mutual Coupling Compensation," in *2020 IEEE/MTT-S International Microwave Symposium (IMS)*, 2020, pp. 1077–1080.

[130] S. H. Talisa *et al.*, "Benefits of Digital Phased Array Radars," *Proc. of the IEEE*, vol. 104, no. 3, pp. 530–543, Mar. 2016.

[131] V. Ariyarathna, D. F. G. Coelho, S. Pulipati, R. J. Cintra, F. M. Bayer, V. S. Dimitrov, and A. Madanayake, "Multibeam digital array receiver using a 16-Point multiplierless DFT approximation," *IEEE Transactions on Antennas and Propagation*, vol. 67, no. 2, pp. 925–933, 2019.

[132] Xilinx, "Zynq UltraScale+ RFSoC," 2020. [Online]. Available: https://www.xilinx.com/products/silicon-devices/soc/rfsoc.html

[133] Z. Zheng *et al.*, "MISC Array: A New Sparse Array Design Achieving Increased Degrees of Freedom and Reduced Mutual Coupling Effect," *IEEE Trans. on Signal Processing*, vol. 67, no. 7, pp. 1728–1741, Apr. 2019.

[134] ——, "Robust Adaptive Beamforming Against Mutual Coupling Based on Mutual Coupling Coefficients Estimation," *IEEE Trans. on Vehicular Technology*, vol. 66, no. 10, pp. 9124–9133, Oct. 2017.

[135] W.-S. Lu and T. Hinamoto, "A second-order cone programming approach for minimax design of 2-D FIR filters with low group delay," in *Proc. IEEE Int. Symp. Circuits Syst.*, 2006, pp. 2521–2524.

[136] T. K. Gunaratne and L. T. Bruton, "Beamforming of Broad-Band Bandpass Plane Waves Using Polyphase 2-D FIR Trapezoidal Filters," *IEEE Trans. on Circuits Syst.*, vol. 55, no. 3, pp. 838–850, Apr. 2008.

[137] T. Svantesson, "Mutual coupling compensation using subspace fitting," in *Proc. IEEE Sensor Array and Multichannel Signal Processing Workshop*, 2000, pp. 494–498.

[138] H. Steyskal and J. S. Herd, "Mutual coupling compensation in small array antennas," *IEEE Transactions on Antennas and Propagation*, vol. 38, no. 12, pp. 1971–1975, Dec. 1990.

[139] S. De Silva *et al.*, "Modeling and measuring of antenna array S-parameters and radiation efficiency," in *IEEE International Symposium on Antennas and Propagation*, 2017, pp. 2293–2294.

[140] J. Kota *et al.*, "A 2-D signal processing model to predict the effect of mutual coupling on array factor," *IEEE Antennas and Wireless Propagation Letters*, vol. 12, pp. 1264–1267, 2013.

[141] T. K. Gunaratne, L. Bruton, and P. Agathoklis, "Broadband beamforming of focal plane array (FPA) signals using real-time spatio-temporal 3D FIR frustum digital filters," vol. 59, no. 6, pp. 2029–2040, June 2011.

[142] C. U. S. Edussooriya, L. T. Bruton, P. Agathoklis, and T. K. Gunaratne, "Low-complexity maximally-decimated multirate 3-D spatio-temporal FIR cone and frustum filters," vol. 60, no. 7, pp. 1845–1856, Jul. 2013.

[143] A. Madanayake, C. Wijenayake, D. G. Dansereau, T. K. Gunaratne, L. T. Bruton, and S. B. Williams, "Multidimensional (MD) circuits and systems for emerging applications including cognitive radio, radio astronomy, robot vision and imaging," vol. 13, no. 1, pp. 10–43, 2013.

[144] A. Antoniou and W.-S. Lu, *Practical Optimization: Algorithms and Engineering Applications*. NY: Springer, 2007.

[145] D. E. Dudgeon and R. M. Mersereau, *Multidimensional Digital Signal Processing*. Englewood Cliffs, NJ: Prentice-Hall, 1984.

[146] A. Madanayake, V. Ariyarathna, S. Madishetty, S. Pulipati, R. J. Cintra, D. Coelho, R. Oliviera, F. M. Bayer, L. Belostotski, S. Mandal, and T. S. Rappaport, "Towards a Low-SWaP 1024-Beam Digital Array: A 32-Beam Subsystem at 5.8 GHz," *IEEE Transactions on Antennas and Propagation*, vol. 68, no. 2, pp. 900–912, Feb 2020.

[147] S. Madishetty, "Design of Multi-Beam Hybrid Digital Beamforming Receivers," Master's thesis, The University of Akron, 2018. [Online]. Available: https://etd.ohiolink.edu/

[148] S. B. Venkatakrishnan, E. A. Alwan, and J. L. Volakis, "Wideband RF Self-Interference Cancellation Circuit for Phased Array Simultaneous Transmit and Receive Systems," *IEEE Access*, vol. 6, no. 99, pp. 3425–3432, 2018.

[149] J. T. Logan, R. W. Kindt, and M. N. Vouvakis, "A 1.2 to 12 GHz Sliced Notch Antenna Array," *IEEE Transactions on Antennas and Propagation*, vol. 66, no. 4, pp. 1818–1826, 4 2018.

[150] J. Zhong, A. Johnson, E. A. Alwan, and J. L. Volakis, "Dual-Linear Polarized Phased Array With 9:1 Bandwidth and 60° Scanning Off Broadside," *IEEE Transactions on Antennas and Propagation*, vol. 67, no. 3, pp. 1996–2001, 3 2019.

[151] A. D. Johnson, J. Zhong, S. B. Venkatakrishnan, E. A. Alwan, and J. L. Volakis, "Phased array with low angle scanning and 46:1 bandwidth," *IEEE Transactions on Antennas and Propagation*, pp. 1–1, 2020.

[152] E. Yetisir, N. Ghalichechian, and J. L. Volakis, "Ultrawideband Array With 70^o Scanning Using FSS Superstrate," *IEEE Transactions on Antennas and Propagation*, vol. 64, no. 10, pp. 4256–4265, 10 2016.

[153] A. O. Bah, P. Qin, R. W. Ziolkowski, Y. J. Guo, and T. S. Bird, "A Wideband Low-Profile Tightly Coupled Antenna Array With a Very High Figure of Merit," *IEEE Transactions on Antennas and Propagation*, vol. 67, no. 4, pp. 2332–2343, 4 2019.

[154] W. F. Moulder, K. Sertel, and J. L. Volakis, "Superstrate-Enhanced Ultrawideband Tightly Coupled Array With Resistive FSS," *IEEE Transactions on Antennas and Propagation*, vol. 60, no. 9, pp. 4166–4172, 9 2012.

[155] J. . R. Bayard, M. E. Cooley, and D. H. Schaubert, "Analysis of infinite arrays of printed dipoles on dielectric sheets perpendicular to a ground plane," *IEEE Transactions on Antennas and Propagation*, vol. 39, no. 12, pp. 1722–1732, 12 1991.

[156] N. Ma and H. Zhao, "Reduction of the mutual coupling between aperture coupled microstrip patch antennas using EBG structure," in *2014 IEEE International Wireless Symposium (IWS 2014)*, 2014, pp. 1–4.

[157] K. S. Vishvaksenan, K. Mithra, R. Kalaiarasan, and K. S. Raj, "Mutual Coupling Reduction in Microstrip Patch Antenna Arrays Using Parallel Coupled-

Line Resonators," *IEEE Antennas and Wireless Propagation Letters*, vol. 16, pp. 2146–2149, 2017.

[158] T. T. Zhang, Y. L. Lu, and H. T. Hui, "Simultaneous estimation of mutual coupling matrix and DOAs for UCA and ULA," in *Proc. 17th International Zurich Symposium on Electromagnetic Compatibility*, 2006.

[159] Hon Tat Hui, "Decoupling methods for the mutual coupling effect in antenna arrays: A review," *Recent Patents on Engineering*, vol. 1, no. 2, pp. 187–193, Jun. 2007.

[160] E. M. Friel and K. M. Pasala, "Effects of mutual coupling on the performance of STAP antenna arrays," *IEEE Trans. on Aerospace and Electronic Systems*, vol. 36, no. 2, pp. 518–527, Apr. 2000.

[161] A. Sheldon, L. Belostotski, G. Messier, and A. Madanayake, "Impact of noise bandwidth on noise figure," *IEEE Trans. on Instrumentation and Measurement*, vol. 68, no. 7, pp. 2662–2664, 2019.

VITA

SRAVAN KUMAR PULIPATI

December 4, 1992	Born, Telangana, India
2017-2021	Ph. D., Electrical and Computer Engineering Florida International University Miami, Florida
2014-2016	M.S., Electrical and Computer Engineering The University of Akron Akron, Ohio
2010-2014	B.S., Electronics and Communication Engineering Kakatiya University Telangana, India

PUBLICATIONS AND PRESENTATIONS

1. S. K. Pulipati et al., "A 16-Element 2.4-GHz Multibeam Array Receiver Using 2-D Spatially Bandpass Digital Filters," IEEE Transactions on Aerospace and Electronic Systems, vol. 55, no. 6, pp. 3029-3038, 2019.
2. C. Wijenayake, S. Pulipati et al., "Low-complexity wideband transmit beamforming using network-resonant digital plane-wave filters." IEEE Antennas and Wireless Propagation Letters 17.7 (2018): 1300-1304.
3. A. Madanayake, V. Ariyarathna, S. Madishetty, S. Pulipati, R. J. Cintra, D. Coelho, R. Oliviera, F. M. Bayer, L. Belostotski, S. Mandal, and T. S. Rappaport, "Towards a low-SWaP 1024-beam digital array: A 32-beam subsystem at 5.8 GHz," IEEE Transactions on Antennas and Propagation, vol. 68, no. 2, pp. 900-912, 2020.
4. V. Ariyarathna, D. F. G. Coelho, S. Pulipati et al., "Multibeam digital array receiver using a 16- point multiplierless DFT approximation," IEEE Transactions on Antennas and Propagation, vol. 67, no. 2, pp. 925-933, Feb 2019.
5. V. A. Coutinho, V. Ariyarathna, D. F. Coelho, S. Pulipati et al., "A Low-SWaP 16-Beam 2.4 GHz Digital Phased Array Receiver Using DFT Approximation," in IEEE Transactions on Aerospace and Electronic Systems, vol. 56, no. 5, pp. 3645-3654, Oct. 2020.
6. S. Pulipati et al.,"Aperture-Array & Lens+ FPA Multi-Beam Digital Receivers at 28 GHz on Xilinx ZCU 1275 RF SoC," in 2020 IEEE/MTT-S International Microwave Symposium (IMS). IEEE, 2020, pp. 555-558.

7. S. Pulipati, and R. Ma, "Design Considerations and FPGA Implementation of a Wideband All-Digital Transmit Beamformer with 50% Fractional Bandwidth," 2020 IEEE/MTT-S International Microwave Symposium (IMS), IEEE, 2020.
8. S. Pulipati et al., "FPGA-Based 2-D FIR Frost Beamformers with Digital Mutual Coupling Compensation," in 2020 IEEE/MTT-S International Microwave Symposium (IMS), 2020, pp. 1077-1080.
9. S. Pulipati et al., "Xilinx RF-SoC-based Digital Multi-Beam Array Processors for 28/60 GHz Wireless Testbeds," 2020 Moratuwa Engineering Research Conference (MERCon), IEEE, 2020.
10. U. De Silva, S. Pulipati et al., "A Passive STAR Microwave Circuit for 1-3 GHz Self-Interference Cancellation," 2020 IEEE 63rd International Midwest Symposium on Circuits and Systems (MWSCAS), IEEE, 2020.
11. S. Pulipati et al., " A Direct-Conversion Digital Beamforming Array Receiver with 800 MHz Channel Bandwidth at 28 GHz using Xilinx RF SoC," in 2019 IEEE International Conference on Microwaves, Antennas, Communications and Electronic Systems (COMCAS). IEEE, 2019, pp. 1-5.
12. S. Pulipati et al., "Real-Time FPGA-Based Multi-Beam Directional Sensing of 2.4 GHz ISM RF Sources," in 2019 Moratuwa Engineering Research Conference (MERCon), 2019, pp. 129-134.
13. S. Pulipati et al., "Design of 28 GHz 64-QAM digital receiver," in 2019 International Workshop on Antenna Technology (iWAT), 2019, pp. 193-196.
14. C. Edussooriya, C. Wijenayake, S. Pulipati et al, "Low-Complexity Wideband Transmit Array using Variable-Precision 2-D Sparse FIR Digital Filters," 2019 IEEE International Symposium on Circuits and Systems (ISCAS), IEEE, 2019.
15. S. Pulipati et al., "A 16-element 2.4-GHz digital array receiver using 2-D IIR spatially-bandpass plane-wave filter," 2018 IEEE/MTT-S International Microwave Symposium-IMS, IEEE, 2018.
16. V. Ariyarathna, V. A. Coutinho, S. Pulipati et al., "Real-time 2-D FIR trapezoidal digital filters for 2.4 GHz aperture receiver applications," in Moratuwa Engineering Research Conference, 2018, pp. 1-6.
17. A. Madanayake, V. Ariyrathna, and S. kumar Pulipati, "Design and prototype implementation of an 8-beam 2.4 GHz array receiver for digital beamforming," in 2017 IEEE National Aerospace and Electronics Conference (NAECON), IEEE, 2017, pp. 91-97.